2002

Substitution chemistry in the rhombohedral R7X12Z-type structure

Elizabeth Ann Jensen
Iowa State University

INFORMATION TO USERS

This manuscript has been reproduced from the microfilm master. UMI films the text directly from the original or copy submitted. Thus, some thesis and dissertation copies are in typewriter face, while others may be from any type of computer printer.

The quality of this reproduction is dependent upon the quality of the copy submitted. Broken or indistinct print, colored or poor quality illustrations and photographs, print bleedthrough, substandard margins, and improper alignment can adversely affect reproduction.

In the unlikely event that the author did not send UMI a complete manuscript and there are missing pages, these will be noted. Also, if unauthorized copyright material had to be removed, a note will indicate the deletion.

Oversize materials (e.g., maps, drawings, charts) are reproduced by sectioning the original, beginning at the upper left-hand corner and continuing from left to right in equal sections with small overlaps.

Photographs included in the original manuscript have been reproduced xerographically in this copy. Higher quality 6" x 9" black and white photographic prints are available for any photographs or illustrations appearing in this copy for an additional charge. Contact UMI directly to order.

ProQuest Information and Learning
300 North Zeeb Road, Ann Arbor, MI 48106-1346 USA
800-521-0600

Substitution chemistry in the rhombohedral $R_7X_{12}Z$-type structure

by

Elizabeth Ann Jensen

A dissertation submitted to the graduate faculty

in partial fulfillment of the requirements for the degree of

DOCTOR OF PHILOSOPHY

Major: Inorganic Chemistry

Program of Study Committee:
John D. Corbett, Major Professor
H. F. Franzen
Gordon J. Miller
Nenad M. Kostić
Douglas K. Finnemore

Iowa State University

Ames, Iowa

2002

UMI Number: 3051473

UMI Microform 3051473

ProQuest Information and Learning Company
300 North Zeeb Road
P.O. Box 1346
Ann Arbor, MI 48106-1346

Graduate College

Iowa State University

This is to certify that the doctoral dissertation of

Elizabeth Ann Jensen

has met the dissertation requirements of Iowa State University

Signature was redacted for privacy.

Major Professor

Signature was redacted for privacy.

For the Major Program

TABLE OF CONTENTS

CHAPTER 1. INTRODUCTION

The structures of many of the lanthanide and early transition metal halide compounds are based on M_6X_{12} units that have been long known for niobium and tantalum halides, for example Nb_6Cl_{14}[1] and Ta_6X_{15}[2] (X = Cl, Br). Figure 1 represents this structural unit, in which six metal atoms (M) define a nominal octahedron and the halide atoms (X) bridge each of the twelve M–M edges. Molecular orbital theory predicts that 14 to 16 electrons per cluster are required to make these binary niobium and tantalum halides closed-shell.

The analogous binary halide (X = Cl, Br, I) compounds of electron-poorer metals such as zirconium or hafnium cannot meet the requirement, having only 10 to 12 electrons per cluster.[3] Instead, electronic stability (with respect to alternative phases) is reached by these compounds through the addition of another atom to the cluster. These "heteroatom interstitials" were discovered as adventitious carbon atoms at the centers of the octahedral metal clusters.[4] Low yields and poor reproducibility often plagued syntheses of Zr halides, but when a suitable amount of C was intentionally included in the reaction mixture, compounds such as $Zr_6I_{12}C$ could be prepared in high yield with confidence.[3] As soon as this was recognized, other main group elements such as Be, B, N, Al, Si, Ge, or P were inserted in place of carbon.[4,5] When no other suitable element was available, even alkali metals would fill the role of cluster-centering interstitial.[4,6] It was later concluded that no empty Zr halide clusters exist.

The interstitial atom provides electrons and orbitals for strong bonds with d orbitals on the cluster metals.[7] Metal–interstitial bonding is often more important to cluster

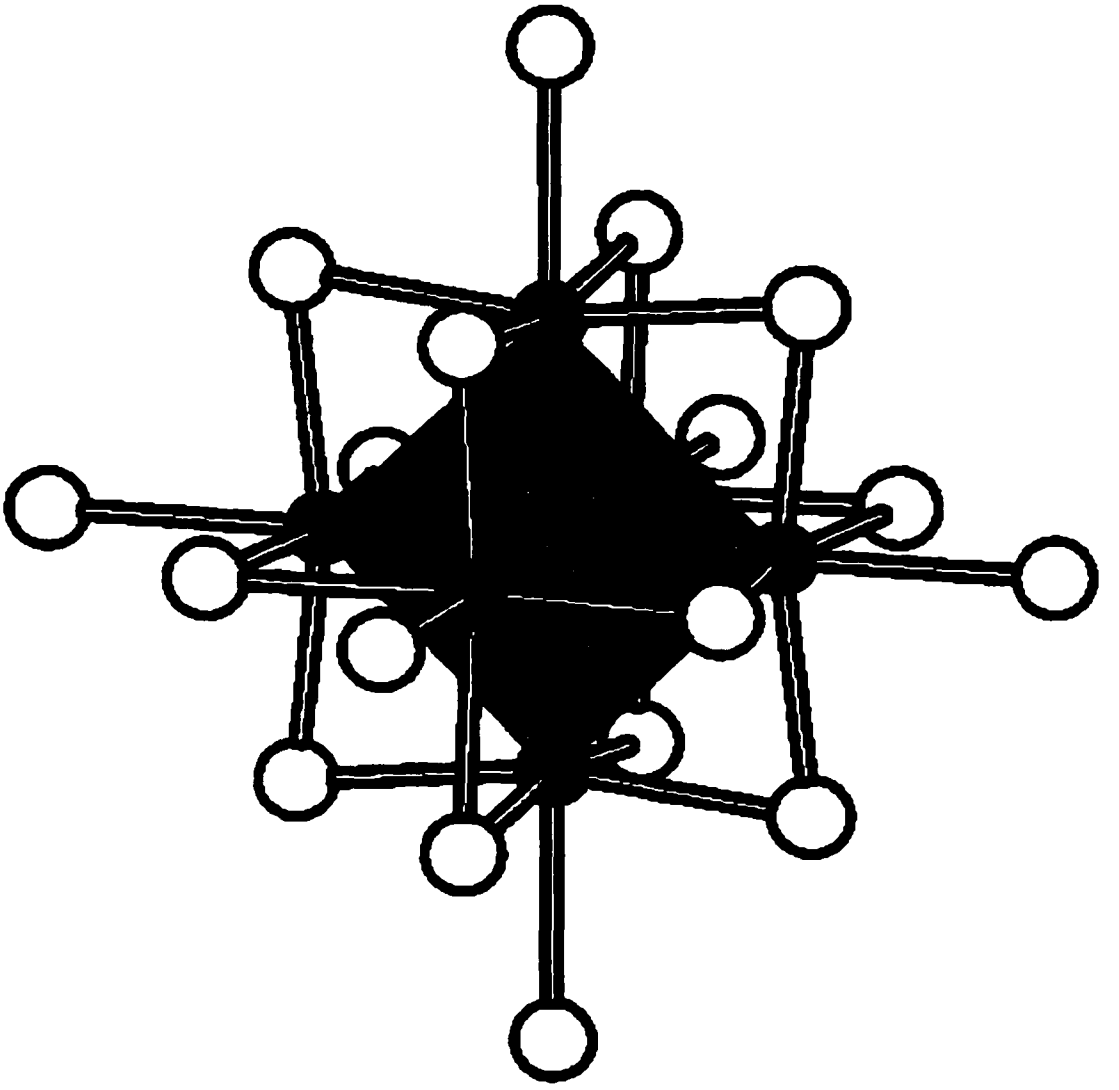

Figure 1. The M_6X_{12} cluster unit with the six terminal halogen atoms also visible. Black and white circles represent metal and halogen atoms, respectively. The M_6 octahedron is shaded.

stabilization than metal–metal bonding. With the discovery that 3d transition metals (Cr, Mn, Fe, Co, Ni[5,8]) could also be incorporated into Zr iodide clusters, the closed-shell electronic requirement was increased to 18, rather than 14, electrons per cluster because the transition metal provided a mainly-nonbonding set of e_g orbitals.

In addition to electronic concerns, stability of these compounds depends on efficient packing, atom sizes, and competition from alternate phases. Zirconium chlorides have a greater variety of structures, while Zr iodides accommodate a wider range of interstitial elements.[9]

Similar chemistry on scandium, yttrium, and lanthanide halides produced similar compounds containing interstitially-stabilized $R_6X_{12}(Z)$ clusters (R = lanthanide metal) with Z = C, B, N,[4,10] dicarbon units,[11,12] and transition metals.[7] It was found that lanthanide clusters obeyed the 18 electron requirement less strictly. Some lanthanide halide cluster compounds were made over a large range of electron counts (14 to 20)[13] whereas zirconium iodides and chlorides rarely deviated from 18 or 19 cluster-based electrons.[7]

Almost all zirconium halide compounds are made of isolated $Zr_6X_{12}(Z)$ clusters. These are interconnected in a variety of ways by multifunctional halide atoms. In addition to the twelve edge-bridging halides (often denoted X^i; i = *inner*), the M_6X_{12} unit has bonding orbitals that project exo from the metal vertices; these terminal positions are always occupied by other halides, X^a (a = *ausser*). The particular way in which these halides are shared between clusters in three dimensions gives rise to the variety of observed stoichiometries. For example, in $MZr_6I_{14}C^3$ (M = K, Rb, Cs) ten of the twelve Zr_6 octahedron edges are bridged by I^i which belong only to that cluster. The two remaining (nonadjacent) edges are bridged by iodides that are also exo-bonded to Zr vertices of

neighboring clusters (I^{i-a}). Conversely, two Zr atoms of this cluster are exo-bonded to I^i of other clusters (I^{a-i}). Furthermore, four other iodides bridge to terminal positions on adjacent clusters (I^{a-a}). The interconnectivity of the compound can be summarized $M^{n+}[Zr_6I^i_{10}I^{i-a}_{2/2}I^{a-i}_{2/2}I^{a-a}_{4/2}(C)]^{n-}$.

Unlike zirconium compounds, ternary lanthanide halides form only three structures featuring isolated $R_6X_{12}(Z)$ clusters: $R_{12}X_{17}Z_2$, $R_6X_{10}Z$, and $R_7X_{12}Z$. Only $R_7X_{12}Z$ is clearly related to a zirconium compound ($Zr_6X_{12}Z$, see below). Other lanthanide compounds form infinite chains or layers of condensed octahedra (e.g. R_3I_3Z[14]), bioctahedral clusters that share one R–R edge (e.g. $La_{10}I_{15}Os_2$,[15] $Gd_{10}I_{16}(C_2)_2$ and $Tb_{10}Br_{15}B_2$[16]) or oligomers made up of four octahedra (e.g. $Y_{16}I_{20}Ru_4$[17] or Gd_5I_7Mn[18]). As in zirconium halides, the variety of bridging halide arrangements results in vastly differing structures even with the same or similar stoichiometries.

The rhombohedral $R_7X_{12}Z$ structure is the most versatile lanthanide halide, known for R = Sc, Y, and most of La–Lu, with X = Cl, Br, or I, although bromides have been considerably less well studied. Many of the iodides were originally reported as "R_7I_{12}" without recognized Z but the structure refinements had evidence of missed interstitials in the form of residual electron density at the centers of the clusters.[19] These compounds accept a great variety of interstitial elements, including most of the transition metals of Groups 6–10 as well as main group elements (B, C, N).[20] The structure consists of R_6 trigonal antiprismatic clusters, only slightly distorted from ideal octahedra, with Z in the centers. All twelve edges are bridged by one of two crystallographically distinct X. Six X1 bridge the R–R edges of the "top" and "bottom" triangular basal faces. The other six "waist" edges are bridged by X2 which also form exo bonds to vertices of adjacent clusters. Reciprocally, the

six vertices of each cluster are terminally bonded to X2 atoms which bridge R–R "waist" edges of neighboring clusters. The seventh R atom (crystallographically labeled R2) is located halfway between R_6Z clusters along the *c* direction, surrounded only by six X1 (three from the cluster below and three from the cluster above) arranged trigonal antiprismatically. This isolated atom is not found in $Zr_6I_{12}Z$ although the halogen functionality and connectivity is the same in both structures (Figures 2 and 3). The detailed formula of $R_7X_{12}Z$ can be written $R^{+3}[R_6(X1^i)_6(X2^{i-a})_{6/2}(X2^{a-i})_{6/2}(Z)]^{-3}$.

Experience with other structures has shown that introduction of alkali or alkaline earth metal cations can produce new compounds with more open structural frameworks dominated by the metal–halide clusters. The cations mainly fulfill charge requirements as in the compounds $AR_6I_{10}Z$ (A = K, Cs; R = Pr, La; Z = Mn, Fe, Os),[21] $Cs_4R_6I_{13}Z$ (R = Ce, Pr; Z = Co, Os),[22] or $Cs_2La_{10}I_{17}Co_2$.[23] Early attempts to substitute the R2 position in $R_7X_{12}Z$ with Ca were largely unsuccessful, resulting in only partially-substituted $(Ca_{0.65}Pr_{0.35})Pr_6I_{12}Co$, $(Ca_{1-y}Gd_y)Gd_6I_{12}Fe$, and $(Ca_{1-z}Gd_z)Gd_6I_{12}Co$ refined from badly twinned crystals.[7] Another investigation gave $CsEr_6I_{12}C$ which has a similar stoichiometry although the cation occupies a different position and the clusters are differently connected.[24] More recently, $NaLa_6I_{12}Os$[25] was discovered during attempts to synthesize analogs of $K_4La_6I_{14}Os$.[26] The present work greatly expands the range of elements allowed to occupy the isolated R2 position.

The synthesis and characterization of some new quaternary lanthanide halides will be discussed in the following chapters. The focus will be on trends affecting the dimensions of the common structure. In addition, electrical and magnetic properties will be considered.

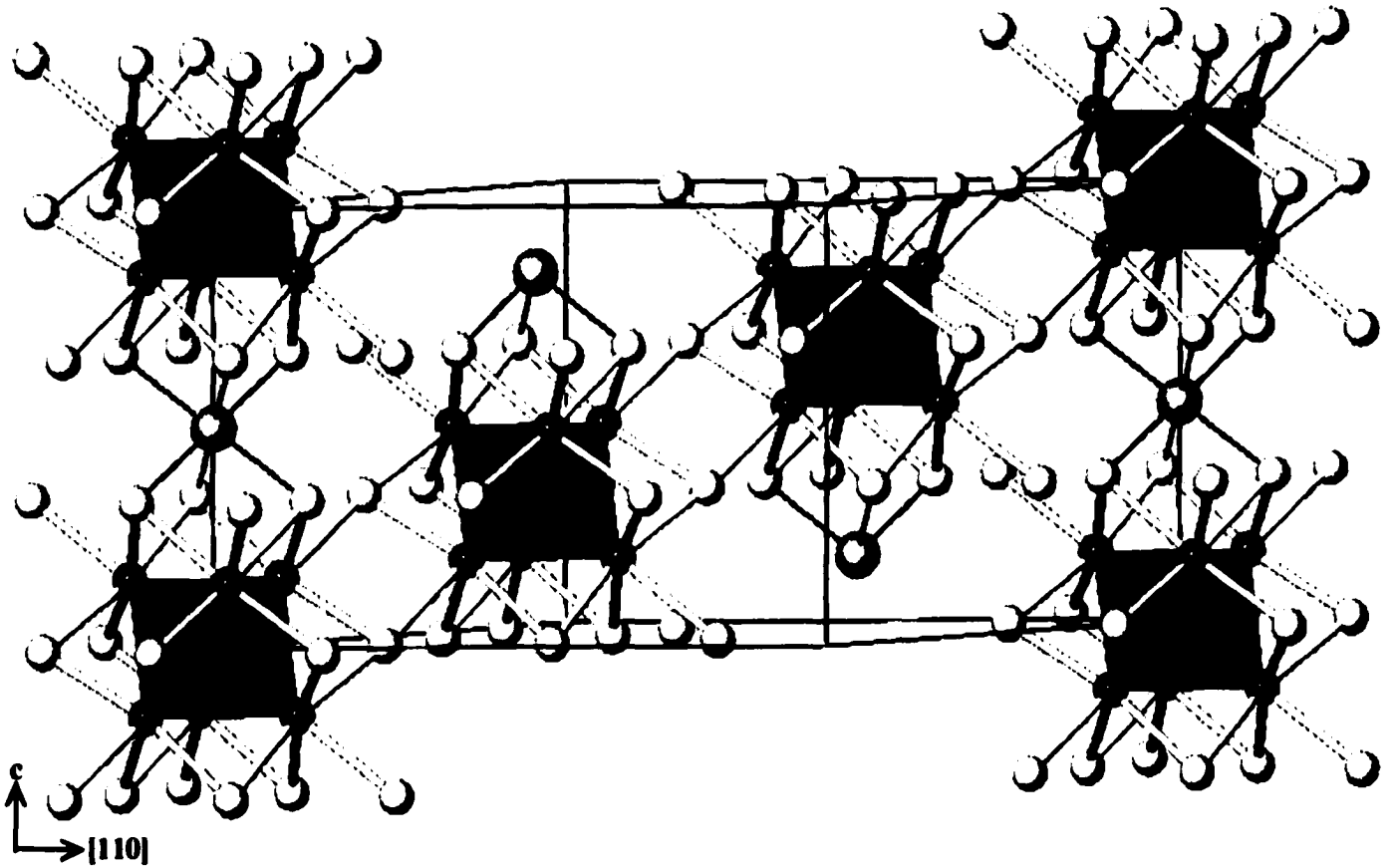

Figure 2. A view of the structure of $NaLa_6I_{12}Os$, showing a section of one chain of $La_6I_{12}Os$ clusters. Small black, large black, grey, and white spheres represent Os, La, Na, and I, respectively. In the parent compound, $La_7I_{12}Os$, the Na position would be occupied by La2.

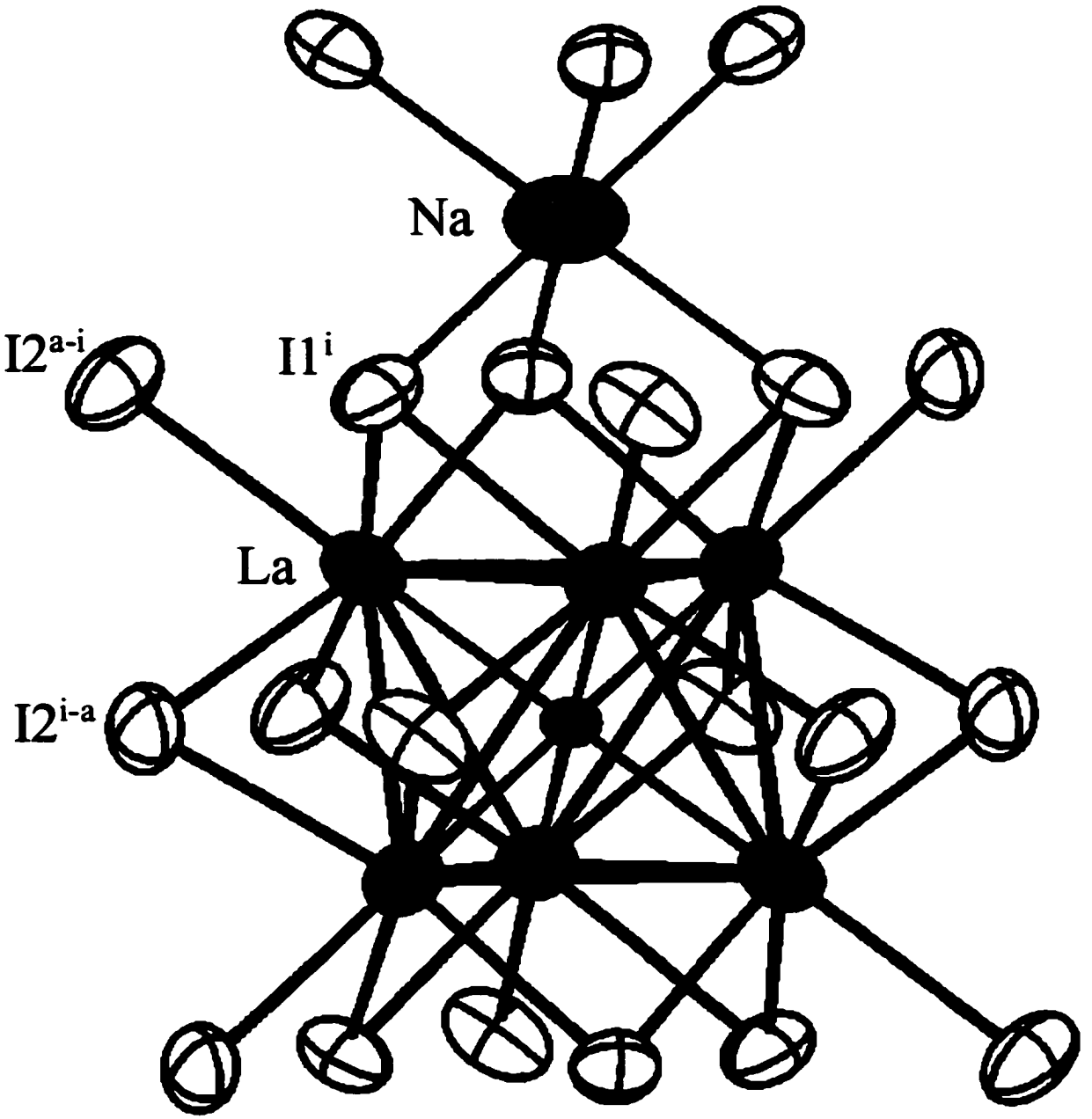

Figure 3. About one independent unit in $NaLa_6I_{12}Os$. Large black, small black, grey, and white (90 %) ellipsoids represent La, Os, Na, and I, respectively. In the parent compound, $La_7I_{12}Os$, the Na position would be occupied by La2.

CHAPTER 2. EXPERIMENTAL DETAILS

Materials

Alkali and Alkaline Earth Metals

Elemental Li (Alfa Aesar, 99.9 %), Mg (Fisher, 99.9 %), Na (Fisher, 99.9 %), and Sr metals (Alfa Aesar, 99.95 %) were stored in a glove box (He-filled in the case of Li; N_2-filled for the others) and were cut just before use to minimize surface impurities. White, powdered alkali and alkaline earth metal iodides (LiI, Alfa Aesar, 99 %; NaI, Mallinckrodt, 99.9 %; KI, Fisher, 99.99 %; RbI, Alfa Aesar, 99.8 %; CsI, Alfa Aesar, 99.9 %; CaI_2, Alfa Aesar, 99.5 %; SrI_2, Aldrich, 99.99 %; BaI_2, Alfa Aesar, 95 %) were dried under dynamic vacuum and purified by vacuum sublimation before storage in small vials in a glove box.

Rare Earth Metals

Rare earth metals (La, Pr) were obtained as thin sheets from the Materials Preparation Center of Ames Laboratory (99.999 %). The metals were stored inside tightly lidded jars in either a He- or N_2-filled glove box. The cold-rolled sheets were scraped with a scalpel to remove any black "tarnish" or oxides and cut into small pieces immediately before use.

Interstitial Elements

Transition metal powders (Co, Alfa Aesar, 99.5 %; Ir, Alfa Aesar, 99.9 %; Fe, Alfa Aesar, 99.9 %; Ni, Alfa Aesar, 99.9 %; Os, Alfa Aesar, 99.95 %; Pd, Alfa Aesar, 99.95 %; Pt, Alfa Aesar, 99.9 %; Re, Alfa Aesar, 99.997 %; Rh, Alfa Aesar, 99.95 %; Ru, Alfa Aesar, 99.95 %; Cu, Fisher, 99.999 %; Ag, Johnson Matthey, 99.9 %), pieces (Mn, Johnson Matthey, 99.99 %; Cd, Alfa Aesar, 99.9999 %), and wire (Au, Alfa Aesar, 99.95 %) were stored in vials in a N_2-filled glove box and used as received.

Rare Earth Metal Trihalides

The rare earth metal triiodides were prepared by direct reaction of the elements[27] according to

$$2\ La + 3\ I_2 = 2\ LaI_3.$$

A special two-armed fused silica apparatus, connected to a ball joint by a long neck, was constructed with a tungsten crucible inside the larger arm. Pieces of La metal and I_2 (Fisher, 99.8 %) were placed into the crucible and the apparatus was evacuated and sealed at the neck. A liquid N_2 trap was placed around the smaller arm and the crucible was slowly heated to 150 °C with a tube furnace in order to sublime the I_2 into the smaller arm. Then both arms were heated, the crucible to 800 °C and the I_2 side to 130 °C, while the connecting tube was wrapped with heating tape held at 100 °C to prevent blockage of the tube by condensed I_2. After 24 hours, the temperature of the I_2 arm was increased to 180 °C. After a further 48 hours the crucible was cooled to 300 °C and the remaining I_2 was collected in the small arm with a liquid N_2 trap. The connecting tube was sealed and the crucible was cooled to room temperature. Inside a N_2-atmosphere glove box the large arm was broken open and the yellowish products removed from the crucible. Vacuum sublimation at 860 °C was used to purify LaI_3. To prevent it from reacting with the fused silica sublimation tube, the powdered triiodide salt was placed inside a tantalum crucible and fitted with a tantalum condenser in a N_2-filled glove box. The tantalum assembly was then placed inside a fused silica tube. The apparatus was joined to the vacuum line horizontally and was heated under dynamic vacuum using a mercury diffusion pump. A dry ice/acetone trap was used near the diffusion pump and a liquid nitrogen trap was placed near the fused silica reaction tube. A sample of the purified product was characterized by Guinier x-ray powder diffraction and, when necessary,

was resublimed until no LaOI was detected in the powder pattern. The final pale yellow powder was placed in a vial stored in a N_2-filled glove box.

Praseodymium triiodide was prepared analogously to LaI_3. In this case the reaction temperatures were the same as for LaI_3 and the product was a bright green powder which was sublimed under vacuum at 800 °C and checked for purity by x-ray powder diffraction. The product was stored in a N_2-filled glove box.

The ammonium bromide route was used to prepare rare-earth metal tribromides.[28] In this multistep process, the sesquioxide R_2O_3 is first reacted with excess NH_4Br to form $(NH_4)_2RBr_5$

$$10\ NH_4Br + R_2O_3 = 2\ (NH_4)_2RBr_5 + 6\ NH_3 + 3\ H_2O.$$

The ammonium salt is then decomposed under vacuum to form RBr_3

$$(NH_4)_2RBr_5 = RBr_3 + 2\ NH_4Br.$$

The tribromides were purified by vacuum sublimation in a Ta container and stored in a N_2-filled glove box.

La_2O_3 was ground together with a large excess of NH_4Br (Fisher, 99 %) and placed into a Pyrex tube. The open end of the tube was drawn into a capillary about 15–20 cm long. The tube was then heated in air to 280 °C inside a fume hood. During the reaction, H_2O and NH_3 gases evolved and exited the tube through the capillary. After 24 hours, the grey-white product, probably a mixture of $(NH_4)_2LaBr_5$, NH_4Br and side products (LaOBr), was transferred to a porcelain crucible inside a Pyrex tube and heated under dynamic vacuum to 400 °C. The $(NH_4)_2LaBr_5$ salt decomposed and NH_4Br sublimed to the cooler end of the tube while anhydrous $LaBr_3$ remained in the hot zone.

$LaBr_3$ was purified by vacuum sublimation at 850 °C, similarly to the triiodides. When necessary, the product was resublimed until no LaOBr was detected in the x-ray powder pattern. The final white powder was placed in a vial stored in a N_2-filled glove box.

Synthetic Techniques

Rare-earth metal halide compounds were produced at temperatures near 1000 °C. Generally, solid state syntheses take place in Pyrex or fused silica tubes; but the reaction of metal halides with these containers at high temperatures is well known. Instead, containers of the refractive metals Nb or Ta may be used successfully[29] to prepare many reduced metal halides. The metals are relatively easy to cut and shape and can be sealed by arc welding. The containers are vulnerable to air oxidation at high temperatures but enclosure within an evacuated fused silica jacket prevents this. In this study, the less expensive niobium tubes were expected to work well according to past experiences, but the metal tubes themselves included too much [O] (~135 ppm) which diffused into and contaminated the reactants, resulting in production of 40–100 % LaOI. Therefore, most syntheses were done in Ta containers.

Tantalum tubes (3/8 inch o.d.) were cut into ~5 cm lengths and cleaned with a solution of 55 % conc. H_2SO_4, 25 % conc. HNO_3, and 20 % conc. HF (by volume) for about 30 seconds in a fume hood. The tubes were then rinsed with running distilled water. After drying in air at room temperature, one end of each tube was crimped shut in a vise and sealed by arc welding.

Routine syntheses began by loading weighed amounts of reactants into a prepared tantalum tube. Most loading was done in N_2-filled dry box (or identical He-filled dry box for reactions loaded with metallic Li) from Vacuum Atmospheres Co., model DLX-001-S-P,

equipped with a Vacuum Atmospheres DRI-TRAIN regeneration system, model HE-493. Continual circulation of the N_2 (or He) atmosphere through an activated Cu/molecular sieve catalyst to reduce the levels of moisture and oxygen as far as possible. The moisture level inside the glove box was maintained at < 1 ppm by volume and monitored with a Panametrics System 3A hygrometer. The total mass of most reactions was 0.25 g. Quantities were measured on an analytical balance with ±0.0005 g precision. After all reactants were added, the open end of the tube was crimped shut and tubes were transported inside a tightly lidded jar to the arc welder, where they were sealed under argon. The Ta reaction containers were exposed to air for only a few seconds during transfer from the jar to the welding chamber. The chamber was immediately evacuated, then backfilled with Ar gas and evacuated until the pressure was less than 40 millitorr. The chamber was backfilled with Ar to just below atmospheric pressure before welding.

Loaded, sealed containers were enclosed in a fused silica tube attached to a ball joint by a long (15 – 30 cm) neck. The containers and interior of the silica jacket were cleaned with the Ta cleaning solution and rinsed with distilled water. After drying in air at room temperature, the silica jacket was attached to the vacuum line equipped with a mercury diffusion pump. Under dynamic vacuum, the silica jacket was heated three times with a oxygen/natural gas torch until glowing red hot to remove water from the silica. The jacket was removed from the vacuum line by sealing the neck with the torch. The reaction assembly was placed into a ThermCraft Marshall furnace with an EuroTherm programmable temperature controller and chromel-alumel thermocouples (placed adjacent to the silica jacket inside the furnace) to control and monitor the temperature cycles.

After reaction, the tube contents were examined under a low power microscope inside a N_2-filled glove box. Potential single crystals were removed. A portion of the products was prepared for x-ray powder diffraction. Remaining product was sealed into evacuated Pyrex ampoules for storage.

Characterization

Visual Inspection

Reactions were opened inside a N_2-filled Blickman glove box equipped with a Vacuum Atmospheres model HE-493 regeneration system. The moisture level was monitored with a Panametrics model 700 hygrometer and never exceeded 1-3 ppm during normal usage. A binocular microscope, objective removed, was mounted above the horizontal Plexiglas top. One or both welded ends of the metal container were cut off and the inner container walls were scraped with a spatula to ensure that all products were removed. Products were carefully examined and color, morphology and relative amounts of each different material were noted. With experience, it was possible to identify some materials (e.g. LaOI).

X-ray Powder Diffraction

The products of every reaction were characterized by x-ray powder diffraction. Since each phase displays a "fingerprint" pattern of diffraction maxima, these patterns could be used to identify components in multiphase samples. In addition, the relative amounts of each product in a sample could be estimated by comparing the intensities of similar diffraction lines.

After visual inspection, a portion of the reaction products were prepared for Guinier powder diffraction analysis. Each sample was ground into coarse powder with a mortar and

pestle, mixed with a small quantity of Si standard (NIST, SRM-640b), and mounted between two pieces of cellophane (Scotch) tape to prevent exposure to air. The sample was transferred from the glove box to the camera inside a capped vial to further reduce exposure to air. Powder patterns were obtained on Kodak BIOMAX MR Scientific Imaging Film within the dynamically evacuated chamber of an Enraf-Nonius FR-552 Guinier camera with rotating sample holder. Monochromated Cu $K\alpha_1$ radiation ($\lambda = 1.540598$ Å) was produced by a sealed tube x-ray generator operating at 45 kV and 20 mA. The range of the exposed film, ~ 2–85 ° in 2θ, was enough to record the first five Si lines.

The resulting powder pattern was visually compared to calculated patterns of known elements and compounds (or hypothetical compounds with known structure types) generated with the computer program POWDER.[30] The "fingerprint" quality of powder diffraction patterns made it possible to approximately determine the composition of the samples by examination. When more than one compound was evident in the powder pattern of the reaction products, the relative yields of the phases could be estimated based on the intensities of the stronger diffraction lines. This method must be employed with care, as differing symmetries of the components, preferred orientation of the crystallites, and other factors can affect the relative intensities.

Experimental powder patterns of $ALa_6I_{12}Z$ compounds were converted to digital format by a LS20 Line Scanner (KEJ Instruments) and the computer programs SCAN and SCANPI.[31] The program COMPARE[32] was used to digitally match the experimental diffraction lines to calculated patterns. The powder pattern lines of known phases were indexed and lattice parameters and errors were calculated via least squares refinement of line positions relative to Si using the program LATT.[33] Because the quality of the least squares

results depends on the number of diffraction lines, only patterns with ≥10 matched lines are reported. In addition, whenever lattice constants were refined from powder patterns of two or more reactions with the same loaded composition, the one with the greater number of matched diffraction lines is reported.

Single Crystal X-ray Diffraction

Single crystals were selected by visual inspection of reaction products. Particles showing smooth faces or geometric shapes that might indicate crystal growth were sought. Small, irregular chunks of apparently homogeneous material were chosen in the absence of more helpful features. Potential crystals were removed from the bulk with the grease-coated tip of a glass fiber pulled from a Pyrex or fused silica rod. The grease used was Apiezon L vacuum grease, degassed by heating with a natural gas flame under dynamic vacuum. When necessary, powder and other debris was removed from the crystal with the tip of a scalpel blade or by rolling it in grease on a microscope slide. The crystal was mounted to the inner wall of a fused silica capillary (0.5 mm i.d.) with grease. The open end of the capillary was plugged with grease and the capillary was removed from the glove box and sealed with a small natural gas/oxygen torch. The capillary was mounted in a metal pin and the free end was coated with black Apiezon W wax to improve visibility.

Crystal quality was measured by photographic diffraction methods. Laue photos were used to determine the suitability of potential single crystals. Crystals that produced powder rings or non-singular spots were discarded. The best crystals were studied further.

Crystallographic data were normally collected at room temperature using graphite-monochromated Mo Kα radiation ($\lambda = 0.70173$ Å) on a Rigaku AFC6 automated four-circle diffractometer. Radiation was produced by a Rigaku RU200 rotating anode generator

operating at 49 kV and 150 mA. Computer software (Molecular Structure Corporation) controlled the operation of the instrument and permitted location, centering, measurement, and indexing of reflections. Companion programs for determination of cell parameters, lattice symmetry, and an orientation matrix were utilized before data collection parameters were chosen. Three standard reflections were measured periodically to monitor instrument and crystal stability. No significant decay was observed in any of the data sets. After data collection, ψ-scans were measured on at least three intense reflections with χ near 90 °.

A Lorentz-polarization correction and an empirical absorption correction using an averaged ψ-scan were included in initial data processing. Reflections were defined as observed if $I/\sigma_I \geq 2$. The space group was determined from extinction conditions identified by examination of the data set. Redundant data were averaged and the unique data set was used for structure refinement. Initial data processing and application of empirical absorption corrections was done using **teXsan** for Windows (Version 1.04, Molecular Structure Corporation, © 1997–1998). The initial model for structure solution was obtained by direct methods using the XS procedure in the SHELXTL™ (Version 5.1, Bruker AXS, Inc., © 1998) software package.

The XL program in the SHELXTL™ package was used for structure refinement. A full-matrix least-squares calculation on F^2 followed by Fourier syntheses was used to refine atomic positions and thermal displacement parameters. The structure factors were calculated using neutral atomic scattering factors with corrections for both real and imaginary parts of anomalous dispersion for elements with $Z > 10$.[34] Refinement of an extinction parameter was usually appropriate. Site/fractional occupancies of the isolated metal atom position were

refined in all cases. The overall quality of the solution was measured by the residual electron density observed in a final difference Fourier map, along with the values of R1 and *w*R2.

Tables of data collection and refinement parameters are reported below, as well as tables of positional and thermal parameters, important interatomic distances, and angles for specific compounds.. Drawings of the structures were generated with the program Atoms (Version 5.0, Shape Software, Kingsport, TN, © 1999 Eric Dowty). Thermal ellipsoids are drawn at the 90 % probability level unless otherwise indicated. Definitions of some important structure refinement parameters are given below.

1. The linear absorption coefficient, μ, is given by

$$\mu = \frac{n}{V} \sum_i n_i(\mu_a)_i$$

in which n_i is the number of atoms of element i in the unit cell volume V and μ_a is the atomic absorption coefficient tabulated in the International Tables.[34]

2. An extinction parameter, x, is refined where F_c is multiplied by

$$k [1 + 0.001 \times F_c^2 \lambda^3 / \sin(2\theta)]^{-1/4}$$

where k is the overall scale factor. This expression is empirical and represents a compromise to cover both primary and secondary extinction.

3. The R factor for averaging data is given by

$$R(int) = \sum |F_o^2 - F_o^2(mean)| / \sum [F_o^2]$$

in which F_o^2 is the experimental measurement. Both summations in R(int) include all input reflections for which more than one symmetry equivalent has been averaged.

4. The crystallographic R indices: The quantity minimized, *w*R2, depends on F_o^2, and will appear about twice as large as those based on F. The index R1 is more conventional and is

relatively insensitive to the weighting scheme.

$$wR2 = \{ \sum [w(F_o^2 - F_c^2)^2] / \sum [w(F_o^2)^2] \}^{1/2}$$

$$R1 = \sum | |F_o| - |F_c| | / \sum |F_o|$$

5. The Goodness of Fit (GooF) is calculated from F^2 according to the expression

$$GooF = \{ \sum [w(F_o^2 - F_c^2)^2] / (n - p) \}^{1/2}$$

in which n is the number of reflections and p is the total number of parameters refined. A GooF close to unity is ideal.

6. The coefficients of the anisotropic displacement factor (U_{ij}) are given by the expression (in units of $Å^2$)

$$\exp(-2\pi^2 [h^2(a^*)^2U_{11} + k^2(b^*)^2U_{22} + ... + 2hka^*b^*U_{12}]).$$

7. The isotropic temperature factor Ueq is given by the expression (in units of $Å^2$)

$$\exp(-8\pi^2 Ueq [\sin(\theta) / \lambda]^2).$$

8. The site occupation factor (s.o.f.) for an atom is given by

$$s.o.f. = (PS)/G$$

in which P is the site occupancy, S is the site multiplicity per unit cell (as given in the International Tables[35]), and G is the multiplicity of the general position for that space group.

Neutron Powder Diffraction

Neutron powder diffraction on a 3 cm^3 sample of $Li_xLa_6I_{12}Os$ (loaded composition $Li_3La_6I_{12}Os$) was done on the General Purpose Powder Diffractometer (GPPD) of the Intense Pulsed Neutron Source (IPNS) at Argonne National Laboratory. Diffraction patterns were collected at room temperature with the sample enclosed in a capped cylindrical vanadium

container. The resulting data were refined by the Rietveld method[36,37] using the General Structure Analysis System[38] (GSAS).

At any point in the powder pattern, the total normalized profile intensity, I_o, is given by the expression

$$I_o = \frac{I_o'}{WI_i}$$

where I_o' is the number of counts observed in a channel of width W and I_i is the incident intensity. The total calculated intensity, I_c, is given by

$$I_c = I_b + S_h \sum_p S_{ph} Y_{ph}$$

where I_b is the background intensity, S_h is the histogram scale factor, S_{ph} is the phase-specific scale factor within the histogram, and Y_{ph} is the contribution from the h^{th} reflection of the p^{th} phase.

The profile of the diffracted peaks may be described by the pseudo-Voigt function, which is a combination of Gaussian and Lorentzian functions

$$H(\Delta T) = (1 - \eta)N[e^u erfc(y) + e^v erfc(z)] + \frac{2N\eta}{\pi}\{-\mathrm{Im}[e^p E_1(p)] - \mathrm{Im}[e^q E_1(q)]\}$$

where *erfc* is the complementary error function. The normalization factor, N, and the coefficients u, v, y and z are given by

$$N = \frac{\alpha\beta}{2(\alpha + \beta)}$$

$$u = \frac{\alpha}{2}(\alpha\sigma^2 + 2\Delta T)$$

$$v = \frac{\beta}{2}(\beta\sigma^2 - 2\Delta T)$$

$$y = \frac{\alpha\sigma^2 + \Delta T}{\sqrt{2\sigma^2}}$$

$$z = \frac{\beta\sigma^2 - \Delta T}{\sqrt{2\sigma^2}}.$$

The Lorentzian and Gaussian mixing factor, η, is given by the equation

$$\eta = 1.36603(\gamma/\Gamma) - 0.47719(\gamma/\Gamma)^2 + 0.11116(\gamma/\Gamma)^3$$

in which γ is the Lorentzian coefficient and Γ, a function of the total Gaussian FWHM ($\Gamma_g = \sqrt{8\sigma^2 \ln 2}$), is

$$\Gamma = \sqrt[5]{\Gamma_g^5 + 2.69269\Gamma_g^4\gamma + 2.42843\Gamma_g^3\gamma^2 + 4.47163\Gamma_g^2\gamma^3 + 0.07842\Gamma_g\gamma^4 + \gamma^5}\ .$$

The coefficients p and q are defined as

$$p = -\alpha\Delta T + \frac{i\alpha\gamma}{2}$$

$$q = -\beta\Delta T + \frac{i\beta\gamma}{2}.$$

The profile coefficients are defined as

$$\alpha = \alpha_1/d$$

$$\beta = \beta_0 + \beta_1/d^4$$

$$\sigma^2 = \sigma_0^2 + \sigma_1^2 d^2 + \sigma_2^2 d^4$$

$$\gamma = \gamma_0 + \gamma_1 d + \gamma_2 d^2 + (\gamma_{1c} d + \gamma_{2c} d^2)\cos\Phi\ ,$$

for reflections that can be described by a sublattice, and

$$\gamma = \gamma_0 + \gamma_1 d + \gamma_2 d^2 + (\gamma_{1c} d + \gamma_{2s} d^2)\cos\Phi,$$

for the bulk of the reflections.

The residuals R_p and R_{wp} are defined as

$$R_p = \frac{\sum | I_o - I_c |}{\sum I_o}$$

$$R_{wp} = \sqrt{\frac{M}{\sum w I_o^2}}$$

with

$$M = \sum w(I_o - I_c)^2 .$$

The weights, *w*, are derived from an error propagation scheme and are assumed to be uncorrelated.

The reduced χ^2, or goodness of fit, is defined by

$$\chi^2 = \frac{M}{N_{obs} - N_{var}} .$$

The isotropic temperature factors, U_{iso}, are expressed as thermal corrections to the structure factor (with units of $Å^2$) according to

$$\exp[-(8\pi^2 U_{iso} \sin^2\theta/\lambda^2)].$$

Background contributions were accounted for by the function

$$I_b = \sum_{j=1}^{36} B_j \frac{Q^{2(j-1)}}{(j-1)!}$$

in which $Q = 2\pi/d$ and the values of B_j are determined by least squares during the Rietveld refinement of the powder pattern.

An absorption coefficient, A_B, was refined in the equation for sample absorption

$$A_h = \exp[-T_1 A_B \lambda - T_2 A_B^2 \lambda^2]$$

in which $T_1 = 1.7133 - 0.0368\sin^2\theta$ and $T_2 = -0.0927 - 0.3750\sin^2\theta$

Neutron scattering lengths[39] used in the refinement are given in Table 1; unlike x-ray

Table 1. Neutron scattering lengths

Atom	Li	La	I	Os	O
Neutron Scattering Length	-0.203	0.827	0.528	1.07	0.5805

scattering, neutron scattering is not directly proportional to atomic number. The portion of the diffraction pattern below 7 μs TOF was excluded from the refinement, based on large background interference. The zero point, histogram scale factor, five background parameters, necessary profile parameters, lattice parameters, and atomic positions were refined to convergence with final R_p, R_{wp} = 5.3, 8.2 %.

Magnetic Susceptibility

Magnetic susceptibility measurements were performed on a Quantum Design MPMS SQUID magnetometer. Unsieved powdered samples (40 – 70 mg) were loaded into a fused silica container[40] in a He-filled glove box. The container held the sample between the flat ends of two 3 mm o.d. glass rods inside a concentric 3 mm i.d. glass tube. This container was capped with a latex rubber septum, transferred out of the glove box, and then quickly sealed using a natural gas/oxygen torch. Magnetizations of the samples at 2 or 5 K were checked as a function of the applied field (0 – 6 Tesla) to screen for possible magnetic impurities, but these plots were nearly ideal ($M(T) \rightarrow 0$ as $H \rightarrow 0$). The magnetic susceptibilities were measured at 1 or 3 Tesla between 5 and 300 or 400 K. The data were corrected for the susceptibility of the container as well as with the standard diamagnetic core terms. The susceptibility of each sample was fitted to the Curie-Weiss equation with an additional, temperature independent (van Vleck), term, χ_0,

$$\chi = \frac{C}{T-\theta} + \chi_0$$

in which θ is the Weiss temperature and C, the Curie constant, is given by

$$\frac{Ng^2\mu_B^2}{3k_B}$$

in which N is Avogadro's number, g represents the g-factor, μ_B is the Bohr magneton, and k_B is the Boltzmann constant. The slope of each fit, plotted as χ^{-1} vs. T, gave the Curie constant, from which the sample effective spin-only magnetic moment could be calculated according to

$$\mu_{eff} = 2.828(C)^{1/2}.$$

Electrical Resistivity

In a He-filled glove box, 40 – 60 mg of powder was sieved through a 250 μm mesh onto a 150 μm mesh to obtain a sample of 200 μm average particle size. The sample was diluted with dry chromatographic Al_2O_3 (total volume ~1 cm^3) to minimize contact between the particles and was sealed inside an evacuated Pyrex ampoule about 5 cm long and 10 mm o.d. Measurements were made over the range 100-300 K with a high frequency Hewlett-Packard 4342A Q-meter operating at 34 MHz. When the sample is placed within a coil, the quality factor of a LC circuit induced by rf skin absorption in uniformly sized grains can be measured. The quality factor was measured with the sample in (Q) and out of (Q_0) the coil at regularly spaced temperature intervals (about 10 ° C). The change in the quality factor was used to calculate the sample resistivity ($\Omega \cdot m$) according to

$$\rho = (BVa^2)/\Delta(1/Q)$$

where B is a constant calibrated to the particular coil ($4.84 \cdot 10^5$), V is the sample volume (m^3),

a is the average particle radius (m) and $\Delta(1/Q) = (1/Q) - (1/Q_0)$. This method generally gives resistivity values correct within a factor of two and good temperature dependencies.[41,42] The sample is assumed to be diamagnetic or only weakly paramagnetic.

Solid State Nuclear Magnetic Resonance

For ^7Li solid state MAS-NMR measurements, a small amount of $LiLa_6I_{12}Os$ powder was ground and diluted with dry chromatographic Al_2O_3 to total volume ~1 cm^3 in a N_2-filled glove box, then loaded into the NMR spinner capsule and tightly capped. The capsule was spun at 4 kHz on a Bruker MSL-300 spectrometer at room temperature while the spectrum was obtained. Powdered solid LiCl was used as a reference.

Energy-Dispersive Spectroscopy

Energy-dispersive x-ray spectroscopy (EDS) on a JEOL system 840A scanning electron microscope (SEM), equipped with an IXRF x-ray analyzer system and a Kevex Quantum light element detector, was done to evaluate the elemental compositions of some single crystals. A beam of approximately 20 kV and 0.3 mA gave a count rate of about 2500 s^{-1} for typical data collections. The beam typically sampled an area ~ $1 - 3\ \mu m^2$ and penetrated into the sample about $1 - 2\ \mu m$. Standards (CaI_2, SrI_2, and LaI_3) were measured to ensure proper calibration.

Extended Hückel Molecular Orbital Calculations

Molecular orbital calculations were made with the CAESAR[43] extended-Hückel tight-binding program. Primary Hückel theory only considers valence atomic orbitals. Overlap integrals are included in electronic structure calculations using extended-Hückel theory which incorporates nonorthogonal atomic orbital basis sets. The molecular orbitals are expressed as linear combinations of the atomic orbitals. The H_{ii} values and atomic orbital

coefficients[44] employed are listed in Table 2. Calculations involved an isolated $[La_6I_{18}Z]^{8-}$ cluster from the representative compound $SrLa_6I_{12}Os$, including the six I^{a-i} atoms as well as the twelve edge-bridging I atoms.

Void Space Calculation

The AVOID program (part of the XTEL Program Library from Indiana University Molecular Structure Center) was used to calculate void spaces in the $LiLa_6I_{12}Os$ structure. Given the appropriate input file, consisting of atom positions and element names, the program calculates the largest hole in the crystal lattice as well as distances to neighboring atoms. The user must modify the input file by filling the hole with an atom before the next largest void can be calculated.

Table 2. Atomic parameters for extended Hückel band calculations

Atom	Orbital	H_{ii} (eV)	ζ_{i1}	c_1	ζ_{i2}	c_2
I	5s	-18.0	2.679	1.0		
	5p	-12.7	2.322	1.0		
La	6s	-7.67	2.14	1.0		
	6p	-5.01	2.08	1.0		
	5d	-8.21	3.78	0.7765	1.381	0.4586
Os	6s	-8.17	2.452	1.0		
	6p	-4.81	2.429	1.0		
	5d	-11.84	5.571	0.6372	2.416	0.5598

CHAPTER 3. RESULTS AND DISCUSSION

Syntheses

All reactions were run using the materials and techniques described in Chapter 1. The products of each reaction were characterized by Guinier x-ray powder diffraction and the identification and estimated yields of the products were drawn from the resulting powder pattern. For some loaded compositions, especially $LiLa_6I_{12}Os$ and $NaLa_6I_{12}Os$, many different reaction time/temperature programs were tried in order to optimize the conditions under which the intended compounds were produced in the greatest yield and with diffractometer-quality single crystals. The aim of these experiments was two-fold: first, to discover which alkali and alkaline earth metals (A) could occupy the isolated R2 position and secondly, to explore the range of possible interstitial Z elements for each A. Unless otherwise stated, the loaded composition of all reactions was $AR_6I_{12}Z$ (A = alkali or alkaline earth metal; R = lanthanide metal; Z = transition metal).

A = Lithium

Reactions loaded with Z = Ru, Os, Ir, Pt produced at least 70% $LiLa_6I_{12}Z$. The highest yields (90-100% $LiLa_6I_{12}Z$) were produced by reacting the loaded composition at 900 °C for one week (168 h) followed by cooling to room temperature at 10 °C/h. The analogous reactions with Z = Re, Rh under the same conditions showed none of the desired $LiLa_6I_{12}Z$ product and 80-90 % LaI_3 (starting material) in the powder pattern of the products. Reaction times of 48 hours at 900 °C gave only 80% $LiLa_6I_{12}Z$ for the same loaded compositions. Loading elemental Li did not change either the composition or the yield of the products with respect to reactions loaded with LiI. LiI and/or the hydrated $LiI{\cdot}xH_2O$ were seen in the

products only when five or more equivalents of Li were loaded (as either iodide or metal). When less than one equivalent of Li was loaded, the yield of $LiLa_6I_{12}Os$ decreased, down to 40% for a reaction loaded $Li_{0.1}La_6I_{12}Os$. Most reactions also showed less than 10% LaOI as the only impurity phase.

A = Sodium

The best yields (≥70 %) of $NaLa_6I_{12}Z$ resulted when the loaded composition was reacted at 700-900 °C for one week (168h) and then cooled 10 °C/h to room temperature, with Z = Os, Ir, Pt, Ru, Fe, Co, Ni. None of the target compound resulted from Z = Re, Au, Pd, Cu, Mn; these had the starting materials LaI_3 and/or NaI in the products, indicative of no reaction. In the reaction loaded with Z = Pd, the major products were NaI and La_2IPd_2.[45] In the reaction with Z = Au, cubic La_3I_3Au[46] was the major product. Negative results were obtained for $NaLa_6Br_{12}Z$, with Z = Co, Ni, B, Si, P. All of these resulted in cubic La_3Br_3Z (isostructural with La_3I_3Au) and large amounts of unreacted $LaBr_3$. Various $Na_xLa_6I_{12}Os$ compositions ($x = 0.1 - 4.0$) all gave good yields (≥90 %) of the target phase, along with <10 % of LaOI.

Reaction of loaded composition $NaPr_6I_{12}Ir$ at 900 °C for one week resulted in > 95 % the intended compound. Similar experiments on compositions $NaPr_6I_{12}Z$ (Z = P, As) and $NaPr_6X_{12}Os$ (X = Br, Cl) produced only small amounts of $NaPr_6I_{12}$(P, As) (the other products were cubic Pr_3I_3(P, As) and NaI) and $NaPr_6Br_{12}Os$, and no $NaPr_6Br_{12}As$ (PrI_3 and NaI) or $NaPr_6Cl_{12}Os$ ($PrCl_3$), respectively.

A = Magnesium

Good yields (≥80 %) of $MgLa_6I_{12}Os$ were obtained from a stoichiometric reaction at 900 °C for one week (168 h) followed by cooling to room temperature at 10 °C/h. The other

phases observed in powder patterns of the products were ≤20 % LaI_3 and/or 10 % LaOI. Some single crystals obtained from these reactions gave lattice constants corresponding to triclinic $La_6I_{10}Os$,[47] but this product was not observed in powder patterns, therefore it could have been present only in small quantity (< 5 %).

A = Calcium

Very good yields (90 %) of $CaLa_6I_{12}Z$ (Z = Os, Ir, Co, Ni) were obtained from stoichiometric reactions at 900 °C for one week (168 h) followed by cooling to room temperature at 10 °C/h. Inclusion of alternate interstitial elements (Z = Re, Pt, Mn) in the loaded composition resulted in little or no $CaLa_6I_{12}Z$ and the appearance of LaI_3 in the products. None of the reactions showed greater than 20% LaOI, and most had only 5% or less of this impurity. $CaLa_6I_{12}Os$ could be made in high yield from loaded compositions of $Ca_xLa_6I_{12}Os$ (x = 0.5 – 2.0). In addition, $CaPr_6I_{12}Ir$ was produced in high yield under reaction conditions similar to those of the La reactions.

A = Strontium

Excellent yields (90-100%) of $SrLa_6I_{12}Z$ (Z = Fe, Ru, Os) were obtained from stoichiometric reactions at 800 – 950 °C for one to two weeks, followed by cooling to room temperature at 10 °C/h. The products contained < 10 % LaOI.

A = Other

Reactions loaded $ALa_6I_{12}Z$ with A = K, Rb, Cs, Ba did not produce any of the targeted rhombohedral compound with Z = Os, Ir. Visual identification of the experimental powder patterns was ambiguous for A = K, but none of the digitized patterns (see Chapter 1: Characterization) could be refined to the rhombohedral structure. Large amounts of triclinic $La_6I_{10}Z$ were observed instead, as well as simple binary halides such as KI or RbI. In

addition, single crystals picked from these reactions were invariably triclinic $La_6I_{10}Z$ or other phases. Failure to incorporate Rb, Cs, and Ba into rhombohedral $ALa_6I_{12}Z$ may reflect these atoms' larger sizes and/or greater stability of competing phases (e.g. RbI or $La_6I_{10}Os$). None of the reactions with A = Ag, Sn, Cd, Cu and Z = Os resulted in the target compound.

Single Crystal X-ray Diffraction

$(Li_{0.967}La_{0.033})La_6I_{12}Os$

An irregular black crystal was chosen for x-ray diffraction from a reaction loaded $Li_2La_6I_{12}Os$. A summary of data collection and refinement parameters is given in Table 3. Data collection was performed at room temperature on a Rigaku AFC6 automated diffractometer using Mo Kα radiation. A random search resulted in 25 reflections with an average intensity of 6645 counts per second. These reflections could be indexed to a R-centered hexagonal unit cell. Diffractometer software suggested the Laue class $\bar{3}$. A hemisphere (±h, +k, ±l) of data was collected between the 2θ limits of 3° and 60 °, followed by measurement of ten ψ-scans which resulted in a relative transmission factor range of 0.7656 – 1.0000.

Structure solution began with data reduction, which included Lorentz-polarization corrections and an empirical absorption correction based on an averaged transmission curve. Intensity statistics indicated a centrosymmetric space group. Systematic absences in the data set indicated the space group $R\bar{3}$ (#148) or one noncentrosymmetric space group $R3$ (#146). Direct methods gave an acceptable solution in the expected centrosymmetric group. All data with I > 0 were averaged, resulting in R(int) of 7.0 %. The heavy atoms were located first, followed by the Li. Isotropic refinement of 100 % La2 on the isolated cation site gave R1 and *w*R2 of 22.1, 63.8 %, respectively, and smaller than expected Ueq (less than 10% of the

Table 3. Crystallographic data for $(Li_{0.967}La_{0.033})La_6I_{12}Os$

Space group, Z	$R\bar{3}$ (#148), 3
a, c (Å)[a]	16.147(5), 10.972(4)
V (Å^3)	2477(2)
d_{calc} (g/cm^3)	5.122
μ (Mo Kα, mm^{-1})	22.561
Crystal dimensions (mm)	0.11 x 0.10 x 0.10
Diffractometer	Rigaku AFC6
Radiation, wavelength (Å)	Mo Kα, 0.71069
Scan mode	2θ–ω
Octant measured	±h, +k, ±l
$2\theta_{max}$ (°)	60
No. measured reflections	2573
No. independent reflections, R(int) (I>0)	1628, 0.0697
No. independent observed reflections (I $\geq 2\sigma_I$)	766
No. of variables	34
Relative transmission factor range	0.7656–1.0000
Extinction parameter	4.5(5) x 10^{-5}
Goodness of fit	0.950
R1, *w*R2 (I $\geq 2\sigma_I$)	0.0429, 0.0710
R1, *w*R2 (all data)	0.1570, 0.0928
Largest residual peaks (e/Å^3)	1.66 (0.8 Å from I1), -1.91 (0 Å from Os)

[a] refined cell constants from 14 Guinier lines

other Ueq). When this position was refined as 100 % Li, its Ueq vanished but R1 and *w*R2 improved to 9.0, 27.0 %, respectively. The refinement of the Li occupancy (with Ueq fixed at the average value of the other atoms) failed to converge. A second La atom was assigned to share the position with Li (with Ueq for La2 constrained to the same value as Li) and the occupancy was refined to 96.7(1) % Li and 3.3(1) % La2. The Li/La2 Ueq was about twice as large as the others. The anisotropic refinement resulted in final R1, *w*R2 of 4.3, 9.3 %. Table 4 lists positional and thermal parameters with their associated errors. The largest peak in the final difference Fourier map was 1.66 e/Å^3, located 0.8 Å from I1. The largest negative peak was -1.91 e/Å^3 at 0 Å from Os. There were no problems with the anisotropic thermal parameters; none of these varied greatly from the Ueq values. Important interatomic distances and bond angles are presented in Tables 5 and 6, respectively.

Table 4. Positional and thermal parameters for $(Li_{0.967}La_{0.033})La_6I_{12}Os$

Atom	x	y	z	Ueq	Occ.	U_{11}	U_{22}	U_{33}	U_{23}	U_{13}	U_{12}
La1	0.88381(6)	0.83818(6)	0.15261(8)	0.0230(2)	1	0.0228(5)	0.0228(4)	0.0242(4)	-0.0050(4)	-0.0048(4)	0.0117(4)
I1	0.88391(7)	0.96155(8)	0.3245(1)	0.0308(2)	1	0.0292(5)	0.0329(5)	0.0270(5)	0.0090(5)	-0.0036(5)	0.0130(4)
I2	0.68821(7)	0.76503(8)	-0.0019(1)	0.0375(3)	1	0.0206(4)	0.0372(6)	0.0402(7)	0.0130(6)	-0.0078(5)	0.0036(4)
Os	0	0	0	0.0129(3)	1	0.0130(4)	U_{11}	0.0129(7)	0	0	½ U_{11}
Li	0	0	1/2	0.05(2)	0.967(1)	0.05(2)	U_{11}	0.05(3)	0	0	½ U_{11}
La2	0	0	1/2	0.05	0.033(1)	0.05	U_{11}	0.05	0	0	½ U_{11}

Table 5. Important interatomic distances in $(Li_{0.967}La_{0.033})La_6I_{12}Os$ (Å)

Os–La1	(x6)	2.8743(9)	La1–I1	3.224(1)
Li/La2–I1	(x6)	3.108(1)	La1–I1	3.228(1)
La1–I2[a]		3.246(1)	La1–La1	4.050(2)
La1–I2[a]		3.250(1)	La1–La1	4.079(2)
La1–I2[b]		3.414(1)	I1–I1[c]	4.316(1)

[a] waist bridging I2
[b] exo bonded I2
[c] shortest I–I contact

Table 6. Important bond angles in $(Li_{0.967}La_{0.033})La_6I_{12}Os$ (°)

La1-Os-La1	180.00(4)	Li/La2-I2-La1	89.67(3)
La1-Os-La1	90.41(3)	Li/La2-I1-La1	89.61(3)
La1-Os-La1	89.59(3)	La1-I1-La1	77.77(4)
I1-Li/La2-I1	180.00(4)	La1-I2-La1	77.79(4)
I1-Li/La2-I1	87.94(3)	La1-I2-La1	173.56(4)
I1-Li/La2-I1	92.06(3)	La1-I2-La1	95.91(4)

$Na_1La_6I_{12}Os$

An irregular black crystal was chosen for x-ray diffraction from a reaction loaded $Na_4La_9I_{22}Os_3$. A summary of data collection and refinement parameters is given in Table 7. Data collection was performed at room temperature on a Rigaku AFC6 automated diffractometer using Mo Kα radiation. A random search resulted in 25 reflections with an average intensity of 13943 counts per second. These reflections could be indexed to a R-centered hexagonal unit cell. Diffractometer software suggested the Laue class $\bar{3}$. A quarter sphere (±h, +k, +l) of data was collected between the 2θ limits of 3° and 60 °, followed by measurement of ten ψ-scans which resulted in a relative transmission factor range of 0.3882 – 1.0000.

Structure solution began with data reduction, which included Lorentz-polarization corrections and an empirical absorption correction based on an averaged transmission curve. Intensity statistics indicated a centrosymmetric space group. Systematic absences in the data set indicated the space group $R\bar{3}$ (#148) or one noncentrosymmetric space group $R3$ (#146). Direct methods gave an acceptable solution in the expected centrosymmetric group. All data with I>0 were averaged, resulting in R(int) of 8.7 %. The heavy atoms were located first, followed by the Na. Isotropic refinement of the isolated cation position at 0, 0, ½ as 100 % La2 resulted in reasonable Ueq and R1, *w*R2 of 11.3, 32.8 %. Isotropic refinement of 100 % Na on the isolated cation site gave R1, *w*R2 of 10.2, 29.2 %. Refinement of a second La atom assigned to share the position with Na (with Ueq for La2 constrained to the same value as Na) failed to converge, regardless of the initial percentages of Na and La, therefore the site occupancy was reset to 100 % Na. The Na Ueq was almost twice as large as the average Ueq of the other atoms. The anisotropic refinement resulted in final R1, *w*R2 of 5.7, 18.9 %.

Table 7. Crystallographic data for $Na_1La_6I_{12}Os$

Space group, Z	$R\bar{3}$ (#148), 3
a, c (Å)[a]	15.99(2), 11.13(4)
V (Å^3)	2464(11)
d_{calc} (g/cm^3)	5.061
μ (Mo Kα, mm^{-1})	22.167
Crystal dimensions (mm)	0.16 x 0.12 x 0.12
Diffractometer	Rigaku AFC6
Radiation, wavelength (Å)	Mo Kα, 0.71069
Scan mode	2θ–ω
Octant measured	±h, +k, +l
$2\theta_{max}$ (°)	60
No. measured reflections	1817
No. independent reflections, R(int) (I>0)	1655, 0.0867
No. independent observed reflections (I $\geq 2\sigma_I$)	839
No. of variables	33
Relative transmission factor range	0.3882–1.0000
Extinction parameter	0.6(2) x 10^{-5}
Goodness of fit	0.983
R1, *w*R2 (I $\geq 2\sigma_I$)	0.0567, 0.1445
R1, *w*R2 (all data)	0.1566, 0.1892
Largest residual peaks (e/Å^3)	3.04 (0.8 Å from Os), -3.20 (0.8 Å from Os)

[a] refined cell constants from 12 Guinier lines

Table 8 lists positional and thermal parameters with their associated errors. The largest peak in the final difference Fourier map was 3.04 e/Å^3, located 0.8 Å from Os. The largest negative peak was -3.20 e/Å^3 at 0.8 Å from Os. There were no problems with the anisotropic thermal parameters. Important interatomic distances and bond angles are presented in Tables 9 and 10, respectively.

Table 8. Positional and thermal parameters for $Na_1La_6I_{12}Os$

Atom	x	y	z	Ueq	Occ.	U_{11}	U_{22}	U_{33}	U_{23}	U_{13}	U_{12}
La1	0.95539(7)	0.83858(1)	0.1499(1)	0.0260(3)	1	0.0259(6)	0.0280(5)	0.0234(6)	-0.0057(5)	-0.0008(5)	0.0128(4)
I1	0.86922(9)	0.94953(8)	0.3340(1)	0.0311(3)	1	0.0344(6)	0.0326(6)	0.0249(7)	0.0035(6)	-0.0064(5)	0.0156(5)
I2	0.31272(9)	0.0790(1)	0.0024(2)	0.0372(4)	1	0.0231(6)	0.0494(8)	0.0377(9)	-0.0171(6)	-0.0063(6)	0.0172(5)
Os	0	0	0	0.0152(4)	1	0.0169(4)	U_{11}	0.0120(8)	0	0	1/2 U_{11}
Na	0	0	1/2	0.052(6)	1	0.062(9)	U_{11}	0.03(1)	0	0	1/2 U_{11}

Table 9. Important interatomic distances in $Na_1La_6I_{12}Os$ (Å)

Os–La1	(x6)	2.873(1)	La1–I1	3.224(2)
Na–I1	(x6)	3.210(1)	La1–I1	3.232(2)
La1–I2[a]		3.253(2)	La1–La1	4.051(2)
La1–I2[a]		3.233(2)	La1–La1	4.074(2)
La1–I2[b]		3.436(2)	I1–I1[c]	4.427(1)

[a] waist bridging I2
[b] exo bonded I2
[c] shortest I–I contact

Table 10. Important bond angles in $Na_1La_6I_{12}Os$ (°)

La1-Os-La1	180.00(4)	Na-I1-La1	89.88(4)
La1-Os-La1	90.32(4)	Na-I1-La1	89.75(4)
La1-Os-La1	89.68(3)	La1-I1-La1	77.73(5)
I1-Na-I1	180.00(3)	La1-I2-La1	77.51(6)
I1-Na-I1	89.83(4)	La1-I2-La1	173.64(5)
I1-Na-I1	90.17(4)	La1-I2-La1	96.13(5)

$(Na_{0.887}Pr_{0.113})Pr_6I_{12}Ir$

An irregular black crystal was chosen for x-ray diffraction from a reaction loaded $NaPr_6I_{12}Ir$. A summary of data collection and refinement parameters is given in Table 11. Data collection was performed at room temperature on a Rigaku AFC6 automated diffractometer using Mo Kα radiation. A random search resulted in 25 reflections with average intensity 6969 counts per second. These reflections could be indexed to a R-centered hexagonal unit cell. Diffractometer software suggested the Laue class $\bar{3}$. A hemisphere (±h, +k, ±l) of data was collected between the 2θ limits of 3° and 60 °, followed by measurement of ten ψ-scans which resulted in a relative transmission factor range of 0.2904 – 1.0000.

Structure solution began with data reduction, which included Lorentz-polarization corrections and an empirical absorption correction based on an averaged transmission curve. Intensity statistics indicated a centrosymmetric space group. Systematic absences in the data set indicated the space group $R\bar{3}$ (#148) or one noncentrosymmetric space group $R3$ (#146). Direct methods gave an acceptable solution in the expected centrosymmetric group. All data with I>0 were averaged, resulting in R(int) of 27.3 %. The heavy atoms were located first, followed by the Na. Isotropic refinement of 100 % Na on the isolated cation site gave R1, *w*R2 of 13.8, 22.4 %. A second Pr atom was assigned to share the position with Na (with Ueq for Pr2 constrained to the same value as Na) and the occupancy was refined to 88.7(3) % Na and 11.3(3) % Pr2. The Na/Pr2 Ueq was only slightly larger than the other Ueq. The anisotropic refinement resulted in final R1, *w*R2 of 9.1, 20.3 %. Table 12 lists positional and thermal parameters with their associated errors. The largest peak in the final difference Fourier map was 5.52 e/Å^3, located 1.12 Å from Ir. The largest negative peak was -7.21 e/Å^3

Table 11. Crystallographic data for $(Na_{0.887}Pr_{0.113})Pr_6I_{12}Ir$

Space group, Z	$R\bar{3}$ (#148), 3
a, c (Å)[a]	15.958(8), 10.841(8)
V (Å^3)	2391(3)
d_{calc} (g/cm^3)	5.412
μ (Mo Kα, mm^{-1})	24.901
Crystal dimensions (mm)	0.10 x 0.12 x 0.12
Diffractometer	Rigaku AFC6
Radiation, wavelength (Å)	Mo Kα, 0.71069
Scan mode	2θ–ω
Octant measured	±h, +k, ±l
$2\theta_{max}$ (°)	60
No. measured reflections	3271
No. independent reflections, R(int) (I>0)	1561, 0.2725
No. independent observed reflections (I $\geq 2\sigma_I$)	759
No. of variables	34
Relative transmission factor range	0.2904–1.0000
Extinction parameter	0.7(4) x 10^{-4}
Goodness of fit	0.983
R1, *w*R2 (I $\geq 2\sigma_I$)	0.0912, 0.2027
R1, *w*R2 (all data)	0.1773, 0.2572
Largest residual peaks (e/Å^3)	5.52 (1.12 Å from Ir), -7.21 (0.75 Å from Pr1)

[a] refined cell constants from 11 Guinier lines

Table 12. Positional and thermal parameters for $(Na_{0.887}Pr_{0.113})Pr_6I_{12}Ir$

Atom	x	y	z	Ueq	Occ.	U_{11}	U_{22}	U_{33}	U_{23}	U_{13}	U_{12}
Pr1	0.8821(1)	0.0452(1)	0.1510(2)	0.0218(4)	1	0.0224(7)	0.0189(7)	0.0244(7)	-0.0006(5)	-0.0039(5)	0.0104(6)
I1	0.8678(1)	0.0513(7)	-0.3324(2)	0.0261(5)	1	0.0261(8)	0.0260(9)	0.0251(9)	0.0030(7)	-0.0053(6)	0.0123(7)
I2	0.7466(2)	0.0994(2)	-0.6695(2)	0.0326(5)	1	0.044(1)	0.0306(9)	0.035(1)	0.0095(7)	0.0154(8)	0.0279(8)
Ir	0	0	0	0.0122(5)	1	0.0127(6)	U_{11}	0.0114(9)	0	0	$1/2U_{11}$
Na	0	0	1/2	0.037(7)	0.887(3)	0.039(8)	U_{11}	0.03(1)	0	0	$1/2U_{11}$
Pr2	0	0	1/2	0.037	0.113(3)	0.039	U_{11}	0.03	0	0	$1/2U_{11}$

at 0.75 Å from Pr1. There were no problems with the anisotropic thermal parameters. Important interatomic distances and bond angles are presented in Tables 13 and 14, respectively.

Table 13. Important bond distances in $(Na_{0.887}Pr_{0.113})Pr_6I_{12}Ir$

Ir–Pr1	(x6)	2.840(2)	Pr1–I1	3.161(2)
Na/Pr2–I1	(x6)	3.179(2)	Pr1–I1	3.170(2)
Pr1–I2[a]		3.184(2)	Pr1–Pr1	4.001(3)
Pr1–I2[a]		3.201(2)	Pr1–Pr1	4.032(3)
Pr1–I2[b]		3.324(2)	I1–I1[c]	4.301(2)

[a] waist bridging I2
[b] exo bonded I2
[c] shortest I–I contact

Table 14. Important bond angles in $(Na_{0.887}Pr_{0.113})Pr_6I_{12}Ir$

Pr1-Ir-Pr1	180.00(6)	Na/Pr2-I1-Pr1	89.48(5)
Pr1-Ir-Pr1	90.44(4)	Na/Pr2-I1-Pr1	89.32(5)
Pr1-Ir-Pr1	89.56(4)	Pr1-I1-Pr1	78.38(7)
I1-Na/Pr2-I1	180.00(8)	Pr1-I2-Pr1	78.31(8)
I1-Na/Pr2-I1	89.95(4)	La1-I2-La1	173.99(8)
I1-Na/Pr2-I1	90.05(4)	La1-I2-La1	95.68(7)

$(Na_{0.954}La_{0.046})La_6I_{12}Fe$

An irregular black crystal was chosen for x-ray diffraction from a reaction loaded $NaLa_6I_{12}Fe$. A summary of data collection and refinement parameters is given in Table 15. Data collection was performed at room temperature on a Rigaku AFC6 automated diffractometer using Mo Kα radiation. A random search resulted in 25 reflections with an average intensity of 8315 counts per second. These reflections could be indexed to a R-centered hexagonal unit cell. Diffractometer software suggested the Laue class $\bar{3}$. A hemisphere (±h, +k, ±l) of data was collected between the 2θ limits of 3° and 60 °, followed by measurement of ten ψ-scans which resulted in a relative transmission factor range of 0.3746 – 1.0000.

Structure solution began with data reduction, which included Lorentz-polarization corrections and an empirical absorption correction based on an averaged transmission curve. Intensity statistics indicated a centrosymmetric space group. Systematic absences in the data set indicated the space group $R\bar{3}$ (#148) or one noncentrosymmetric space group $R3$ (#146). Direct methods gave an acceptable solution in the expected centrosymmetric group. All data with I>0 were averaged, resulting in R(int) of 14.5 %. The I and La atoms were located first, followed by the Fe and Na. Isotropic refinement of 100 % Na on the isolated cation site gave R1, *w*R2 of 10.3, 25.3 %. A second La atom was assigned to share the position with Na (with Ueq for La2 constrained to the same value as Na) and the occupancy was refined to 95.4(2) % Na and 4.6(2) % La2. The Na/La2 Ueq was slightly smaller than the average of the other Ueq. The anisotropic refinement resulted in final R1, *w*R2 of 6.1, 12.3 %. Table 16 lists positional and thermal parameters with their associated errors. The largest peak in the final difference Fourier map was 3.37 e/Å^3, located 3.06 Å from I1. The largest negative

Table 15. Crystallographic data for $(Na_{0.954}La_{0.046})La_6I_{12}Fe$

Space group, Z	$R\bar{3}$ (#148), 3
a, c (Å)[a]	16.142(2), 11.122(2)
V (Å^3)	2509.7(8)
d_{calc} (g/cm^3)	4.833
μ (Mo Kα, mm^{-1})	18.978
Crystal dimensions (mm)	0.10 x 0.09 x 0.12
Diffractometer	Rigaku AFC6
Radiation, wavelength (Å)	Mo Kα, 0.71069
Scan mode	2θ–ω
Octant measured	±h, +k, ±l
$2\theta_{max}$ (°)	60
No. measured reflections	3437
No. independent reflections, R(int) (I>0)	1640, 0.1451
No. independent observed reflections (I $\geq 2\sigma_I$)	645
No. of variables	34
Relative transmission factor range	0.3746–1.0000
Extinction parameter	0.1(2) x 10^{-6}
Goodness of fit	0.976
R1, wR2 (I $\geq 2\sigma_I$)	0.0611, 0.1234
R1, wR2 (all data)	0.2051, 0.1649
Largest residual peaks (e/Å^3)	3.37 (3.06 Å from I1), -2.31 (0.22 Å from La1)

[a] refined cell constants from Rigaku diffractometer

Table 16. Positional and thermal parameters for $(Na_{0.954}La_{0.046})La_6I_{12}Fe$

Atom	x	y	z	Ueq	Occ.	U_{11}	U_{22}	U_{33}	U_{23}	U_{13}	U_{12}
La1	0.78271(9)	0.28892(8)	0.1857(1)	0.0320(3)	1	0.0334(7)	0.0237(6)	0.0345(6)	0.0030(6)	-0.0104(6)	0.0111(5)
I1	0.84832(9)	0.4643(1)	-0.0009(1)	0.0318(4)	1	0.0342(8)	0.0324(7)	0.0298(6)	0.0066(6)	0.0088(6)	0.0173(6)
I2	0.9211(1)	0.2342(1)	0.0023(1)	0.0381(4)	1	0.0490(9)	0.0365(8)	0.0413(8)	0.0114(7)	0.0148(7)	0.0308(8)
Fe	0	0	0	0.019(1)	1	0.021(2)	U_{11}	0.016(3)	0	0	$1/2U_{11}$
Na	0	0	1/2	0.027(5)	0.954(2)	0.030(6)	U_{11}	0.023(8)	0	0	$1/2U_{11}$
La2	0	0	1/2	0.027	0.046(2)	0.030	U_{11}	0.023	0	0	$1/2U_{11}$

peak was -2.31 e/Å^3 at 0.22 Å from La1. All other peaks in the map were found within 1 Å of an occupied atomic position. There were no problems with the anisotropic thermal parameters. Important interatomic distances and bond angles are presented in Tables 17 and 18, respectively.

Table 17. Important interatomic distances in $(Na_{0.954}La_{0.046})La_6I_{12}Fe$ (Å)

Fe–La1	(x6)	2.840(2)	La1–I1	3.232(2)
Na/La2–I1	(x6)	3.1395(9)	La1–I1	3.240(2)
La1–I2[a]		3.244(2)	La1–La1	4.012(2)
La1–I2[a]		3.246(2)	La1–La1	4.019(2)
La1–I2[b]		3.449(2)	I1–I2[c]	4.408(2)

[a] waist bridging I2
[b] exo bonded I2
[c] shortest I–I contact

Table 18. Important bond angles in $(Na_{0.954}La_{0.046})La_6I_{12}Fe$ (°)

La1-Fe-La1	180.00(3)	Na/La2-I1-La1	89.89(4)
La1-Fe-La1	90.10(3)	Na/La2-I1-La1	90.03(4)
La1-Fe-La1	89.90(3)	La1-I1-La1	76.63(6)
I1-Na/La2-I1	180.00(2)	La1-I2-La1	77.55(6)
I1-Na/La2-I1	89.80(3)	La1-I2-La1	172.85(6)
I1-Na/La2-I1	90.20(3)	La1-I2-La1	96.31(5)

$(Ca_{0.906}La_{0.094})La_6I_{12}Os$

An irregular black crystal was chosen for x-ray diffraction from a reaction loaded $Ca_2La_9I_{22}Os_3$. A summary of data collection and refinement parameters is given in Table 19. Data collection was performed at room temperature on a Rigaku AFC6 automated diffractometer using Mo Kα radiation. A random search resulted in 25 reflections with average intensity 10616 counts per second. These reflections could be indexed to a R-centered hexagonal unit cell. Diffractometer software suggested the Laue class $\bar{3}$. A hemisphere (±h, +k, ±l) of data was collected between the 2θ limits of 3° and 60 °, followed by measurement of ten ψ-scans which resulted in a relative transmission factor range of 0.5155 – 1.0000.

Structure solution began with data reduction, which included Lorentz-polarization corrections and an empirical absorption correction based on an averaged transmission curve. Intensity statistics indicated a centrosymmetric space group. Systematic absences in the data set indicated the space group $R\bar{3}$ (#148) or one noncentrosymmetric space group $R3$ (#146). Direct methods gave an acceptable solution in the expected centrosymmetric group. All data with I>0 were averaged, resulting in R(int) of 11.3 %. The heavy atoms were located first, followed by the Ca. Isotropic refinement of 100 % Ca on the isolated cation site gave R1, *w*R2 of 10.2, 30.6 %. A second La atom was assigned to share the position with Ca (with Ueq for La2 constrained to the same value as Ca) and the occupancy was refined to 90.6(1) % Ca and 9.4(1) % La2. The Ca/La2 Ueq was only slightly larger than the average of the other Ueq. The anisotropic refinement resulted in final R1, *w*R2 of 3.7, 7.8 %. Table 20 lists positional and thermal parameters with their associated errors. The largest peak in the final difference Fourier map was 1.29 e/Å^3, located 0.8 Å from I2. The largest negative peak was

Table 19. Crystallographic data for $(Ca_{0.906}La_{0.094})La_6I_{12}Os$

Space group, Z	$R\bar{3}$ (#148), 3
a, c (Å)[a]	16.098(3), 11.157(4)
V (Å^3)	2504(1)
d_{calc} (g/cm^3)	5.153
μ (Mo Kα, mm^{-1})	22.562
Crystal dimensions (mm)	0.12 x 0.19 x 0.12
Diffractometer	Rigaku AFC6
Radiation, wavelength (Å)	Mo Kα, 0.71069
Scan mode	2θ–ω
Octant measured	±h, +k, ±l
$2\theta_{max}$ (°)	60
No. measured reflections	2712
No. independent reflections, R(int) (I>0)	1293, 0.1128
No. independent observed reflections (I $\geq 2\sigma_I$)	858
No. of variables	34
Relative transmission factor range	0.5155–1.0000
Extinction parameter	12.6(4) x 10^{-5}
Goodness of fit	0.969
R1, wR2 (I $\geq 2\sigma_I$)	0.0372, 0.0660
R1, wR2 (all data)	0.0826, 0.0782
Largest residual peaks (e/Å^3)	1.29 (0.8 Å from I2), -1.91 (0 Å from Os)

[a] refined cell constants from 18 Guinier lines

Table 20. Positional and thermal parameters for $(Ca_{0.906}La_{0.094})La_6I_{12}Os$

Atom	x	y	z	Ueq	Occ.	U_{11}	U_{22}	U_{33}	U_{23}	U_{13}	U_{12}
La1	0.95444(5)	0.88236(5)	0.14793(9)	0.0139(3)	1	0.0197(4)	0.0210(4)	0.0237(5)	0.0035(3)	-0.0007(3)	0.0091(4)
I1	0.82040(6)	0.94942(6)	0.3400(1)	0.0251(3)	1	0.0257(5)	0.0260(5)	0.0242(7)	0.0020(4)	0.0056(4)	0.0133(4)
I2	0.76380(7)	0.07725(8)	0.0027(1)	0.0373(4)	1	0.0351(6)	0.0488(7)	0.043(1)	-0.0208(5)	-0.0135(5)	0.0322(5)
Os	0	0	0	0.0139(3)	1	0.0134(4)	U_{11}	0.0150(7)	0	0	$1/2U_{11}$
Ca	0	0	1/2	0.034(2)	0.906(1)	0.034(3)	U_{11}	0.034(4)	0	0	$1/2U_{11}$
La2	0	0	1/2	0.034	0.094(1)	0.034	U_{11}	0.034	0	0	$1/2U_{11}$

-1.91 e/Å^3 at 0 Å from Os. There were no problems with the anisotropic thermal parameters. Important interatomic distances and bond angles are presented in Tables 21 and 22, respectively.

Table 21. Important interatomic distances in $(Ca_{0.906}La_{0.094})La_6I_{12}Os$ (Å)

Os–La1	(x6)	2.869(9)	La1–I1	3.266(1)
Ca/La2–I1	(x6)	3.1395(9)	La1–I1	3.275(1)
La1–I2[a]		3.229(1)	La1–La1	4.049(2)
La1–I2[a]		3.234(1)	La1–La1	4.065(1)
La1–I2[b]		3.414(1)	I1–I2[c]	4.387(1)

[a] waist bridging I2
[b] exo bonded I2
[c] shortest I–I contact

Table 22. Important bond angles in $(Ca_{0.906}La_{0.094})La_6I_{12}Os$ (°)

La1-Os-La1	180.00(4)	Ca/La2-I1-La1	91.06(2)
La1-Os-La1	90.24(2)	Ca/La2-I1-La1	90.90(2)
La1-Os-La1	89.76(2)	La1-I1-La1	76.84(3)
I1-Ca/La2-I1	180.00(3)	La1-I2-La1	77.56(4)
I1-Ca/La2-I1	89.11(2)	La1-I2-La1	172.51(3)
I1-Ca/La2-I1	90.89(2)	La1-I2-La1	94.95(3)

$(Ca_{0.621}La_{0.379})La_6I_{12}Os$

An irregular black crystal was chosen for x-ray diffraction from a reaction loaded $Ca_{0.5}La_{6.5}I_{12}Os$. A summary of data collection and refinement parameters is given in Table 23. Data collection was performed at room temperature on a Rigaku AFC6 automated diffractometer using Mo Kα radiation. A random search resulted in 25 reflections with an average intensity of 3491 counts per second. These reflections could be indexed to a R-centered hexagonal unit cell. Diffractometer software suggested the Laue class $\bar{3}$. A hemisphere (±h, +k, ±l) of data was collected between the 2θ limits of 3° and 60 °, followed by measurement of ten ψ-scans which resulted in a relative transmission factor range of 0.7469 – 1.0000.

Structure solution began with data reduction, which included Lorentz-polarization corrections and an empirical absorption correction based on an averaged transmission curve. Intensity statistics indicated a centrosymmetric space group. Systematic absences in the data set indicated the space group $R\bar{3}$ (#148) or one noncentrosymmetric space group $R3$ (#146). Direct methods gave an acceptable solution in the expected centrosymmetric group. All data with I>0 were averaged, resulting in R(int) of 13.9 %. The heavy atoms were located first, followed by the Ca. A second La atom was assigned to share the position with Ca (with Ueq for La2 constrained to the same value as Ca) and the occupancy was isotropically refined to 62.1(2) % Ca and 37.9(2) % La2. The Ca/La2 Ueq was only slightly larger than the average of the other Ueq. The anisotropic refinement resulted in final R1 and *w*R2 of 5.3 and 11.2 %, respectively. Table 24 lists positional and thermal parameters with their associated errors. The largest peak in the final difference Fourier map was 2.53 e/Å^3, located 1.73 Å from La1. The largest negative peak was -3.73 e/Å^3 at 0 Å from Os.

Table 23. Crystallographic data for $(Ca_{0.621}La_{0.379})La_6I_{12}Os$

Space group, Z	$R\bar{3}$ (#148), 3
a, c (Å)[a]	16.118(2), 11.075(2)
V (Å^3)	2491.7(7)
d_{calc} (g/cm^3)	5.171
μ (Mo Kα, mm^{-1})	22.641
Crystal dimensions (mm)	0.12 x 0.19 x 0.12
Diffractometer	Rigaku AFC6
Radiation, wavelength (Å)	Mo Kα, 0.71069
Scan mode	2θ–ω
Octant measured	±h, +k, ±l
$2\theta_{max}$ (°)	60
No. measured reflections	3415
No. independent reflections, R(int) (I>0)	1631, 0.1391
No. independent observed reflections (I $\geq 2\sigma_I$)	725
No. of variables	34
Relative transmission factor range	0.7469–1.0000
Extinction parameter	13.3(9) x 10^{-5}
Goodness of fit	0.923
R1, *w*R2 (I $\geq 2\sigma_I$)	0.0534, 0.0849
R1, *w*R2 (all data)	0.1761, 0.1117
Largest residual peaks (e/Å^3)	2.53 (1.7 Å from La1), -3.73 (0 Å from Os)

[a] refined cell constants from Rigaku diffractometer

Table 24. Positional and thermal parameters for $(Ca_{0.621}La_{0.379})La_6I_{12}Os$

Atom	x	y	z	Ueq	Occ.	U_{11}	U_{22}	U_{33}	U_{23}	U_{13}	U_{12}
La1	0.83736(8)	0.88290(7)	-0.1493(1)	0.0135(5)	1	0.0254(6)	0.0235(6)	0.0241(5)	0.0019(5)	0.0038(5)	0.0135(5)
I1	0.86881(9)	0.05145(9)	-0.3409(1)	0.0299(3)	1	0.0307(7)	0.0318(7)	0.0250(5)	0.0023(6)	-0.0034(6)	0.0141(6)
I2	0.6872(1)	0.9225(1)	-0.0019(1)	0.0390(4)	1	0.0219(6)	0.0532(9)	0.0409(8)	-0.0212(7)	-0.0074(6)	0.0189(6)
Os	0	0	0	0.0150(4)	1	0.0151(5)	U_{11}	0.0150(9)	0	0	$1/2U_{11}$
Ca	0	0	1/2	0.044(5)	0.621(2)	0.028(2)	U_{11}	0.076(6)	0	0	$1/2U_{11}$
La2	0	0	1/2	0.044	0.379(2)	0.028	U_{11}	0.076	0	0	$1/2U_{11}$

There were no problems with the anisotropic thermal parameters. Important interatomic distances and bond angles are presented in Tables 25 and 26, respectively.

Table 25. Important bond distances in $(Ca_{0.621}La_{0.379})La_6I_{12}Os$ (Å)

Os–La1	(x6)	2.867(1)	La1–I1	3.2746(2)
Ca/La2–I1	(x6)	3.165(1)	La1–I1	3.281(2)
La1–I2[a]		3.230(2)	La1–La1	4.052(2)
La1–I2[a]		3.237(2)	La1–La1	4.057(2)
La1–I2[b]		3.417(2)	I1–I2[c]	4.374(1)

[a] waist bridging I2
[b] exo bonded I2
[c] shortest I–I contact

Table 26. Important bond angles in $(Ca_{0.621}La_{0.379})La_6I_{12}Os$ (°)

La1-Os-La1	180.00(4)	Ca/La2-I1-La1	89.54(4)
La1-Os-La1	90.07(3)	Ca/La2-I1-La1	89.43(4)
La1-Os-La1	89.93(3)	La1-I1-La1	76.47(4)
I1-Ca/La2-I1	180.00(3)	La1-I2-La1	77.59(6)
I1-Ca/La2-I1	88.00(4)	La1-I2-La1	172.86(6)
I1-Ca/La2-I1	92.00(4)	La1-I2-La1	95.28(5)

$(Ca_{0.801}La_{0.199})La_6I_{12}Co$

An irregular black crystal was chosen for x-ray diffraction from a reaction loaded $CaLa_6I_{12}Co$. A summary of data collection and refinement parameters is given in Table 27. Data collection was performed at room temperature on a Rigaku AFC6 automated diffractometer using Mo Kα radiation. A random search resulted in 25 reflections with an average intensity of 8609 counts per second. These reflections could be indexed to a R-centered hexagonal unit cell. Diffractometer software suggested the Laue class $\bar{3}$. A hemisphere (±h, +k, ±l) of data was collected between the 2θ limits of 3° and 60 °, followed by measurement of ten ψ-scans which resulted in a relative transmission factor range of 0.5459 – 1.0000.

Data reduction included Lorentz-polarization corrections and an empirical absorption correction based on an averaged transmission curve. Intensity statistics strongly indicated a centrosymmetric space group. Systematic absences in the data set indicated the space group $R\bar{3}$ (#148) or one noncentrosymmetric space group $R3$ (#146). Direct methods gave an acceptable solution in the expected centrosymmetric group. All data with I>0 were averaged, resulting in R(int) of 8.1 %. The heavy atoms were located first, followed by the Ca. Isotropic refinement of 100 % La2 at the isolated cation site resulted in R1, *w*R2 of 11.8, 34.0 % with Ueq two to five times larger than those of the other atoms. Isotropic refinement with 100 % Ca gave R1, *w*R2 of 9.9, 28.1 % and Ueq comparable to the others. Further refinement of the Ca occupancy (with Ueq fixed) failed to converge. A second La atom was added, sharing the position with Ca (with Ueq for La2 constrained to the same value as Ca). Isotropic refinement of the mixed occupancy resulted in 80.1(1) % Ca, 19.9(1) % La2. The final Ca/La2 Ueq was comparable to the other Ueq. The anisotropic refinement resulted in

Table 27. Crystallographic data for $(Ca_{0.801}La_{0.199})La_6I_{12}Co$

Space group, Z	$R\bar{3}$ (#148), 3
a, c (Å)[a]	16.009(2), 11.099(2)
V (Å^3)	2463.4(7)
d_{calc} (g/cm^3)	4.965
μ (Mo Kα, mm^{-1})	19.541
Crystal dimensions (mm)	0.09 x 0.09 x 0.12
Diffractometer	Rigaku AFC6
Radiation, wavelength (Å)	Mo Kα, 0.71069
Scan mode	2θ–ω
Octant measured	±h, +k, ±l
$2\theta_{max}$ (°)	60
No. measured reflections	3369
No. independent reflections, R(int) (I>0)	1609, 0.0814
No. independent observed reflections (I $\geq 2\sigma_I$)	960
No. of variables	34
Relative transmission factor range	0.5459–1.0000
Extinction parameter	26.3(1) x 10^{-5}
Goodness of fit	0.989
R1, wR2 (I $\geq 2\sigma_I$)	0.0359, 0.0573
R1, wR2 (all data)	0.0989, 0.0698
Largest residual peaks (e/Å^3)	1.71 (0.6 Å from I2), -1.63 (0.9 Å from La1)

[a] refined cell constants from Rigaku diffractometer

final R1, *w*R2 of 3.6, 7.0 %. Table 28 lists positional and thermal parameters with their associated errors. The largest peak in the final difference Fourier map was 1.71 e/Å^3, located 0.6 Å from I2. The largest negative peak was -1.63 e/Å^3 at 0.9 Å from La1. There were no problems with the anisotropic thermal parameters. Important interatomic distances and bond angles are presented in Tables 29 and 30, respectively.

Table 28. Positional and thermal parameters for $(Ca_{0.801}La_{0.199})La_6I_{12}Co$

Atom	x	y	z	Ueq	Occ.	U_{11}	U_{22}	U_{33}	U_{23}	U_{13}	U_{12}
La1	0.50445(4)	0.21611(4)	0.18606(4)	0.0166(1)	1	0.0154(2)	0.0162(3)	0.0179(2)	0.0008(2)	-0.0001(2)	0.0076(2)
I1	0.61596(5)	0.15187(4)	-0.00709(5)	0.0238(2)	1	0.0248(3)	0.0256(4)	0.0212(3)	-0.0054(2)	-0.0022(2)	0.0128(3)
I2	0.42970(6)	0.01851(5)	0.33688(6)	0.0338(2)	1	0.0328(4)	0.0169(3)	0.0378(4)	0.0078(3)	-0.0121(3)	0.0021(3)
Co	0	0	0	0.0124(6)	1	0.0115(8)	U_{11}	0.014(1)	0	0	$1/2U_{11}$
Ca	0	0	1/2	0.039(1)	0.801(1)	0.030(2)	U_{11}	0.059(3)	0	0	$1/2U_{11}$
La2	0	0	1/2	0.039	0.199(1)	0.030	U_{11}	0.059	0	0	$1/2U_{11}$

Table 29. Important interatomic distances in $(Ca_{0.801}La_{0.199})La_6I_{12}Co$ (Å)

Co–La1	(x6)	2.8397(3)	La1–I1	3.2675(9)
Ca/La2–I1	(x6)	3.1426(7)	La1–I1	3.2745(9)
La1–I2[a]		3.233(1)	La1–La1	4.010(1)
La1–I2[a]		3.2336(9)	La1–La1	4.022(1)
La1–I2[b]		3.3910(9)	I1–I2[c]	4.339(1)

[a] waist bridging I2
[b] exo bonded I2
[c] shortest I–I contact

Table 30. Important bond angles in $(Ca_{0.801}La_{0.199})La_6I_{12}Co$ (°)

La1-Co-La1	180.00(4)	Ca/La2-I1-La1	90.46(2)
La1-Co-La1	90.17(2)	Ca/La2-I1-La1	90.33(2)
La1-Co-La1	89.83(2)	La1-I1-La1	75.88(2)
I1-Ca/La2-I1	180.00(3)	La1-I2-La1	76.66(3)
I1-Ca/La2-I1	88.65(2)	La1-I2-La1	172.11(3)
I1-Ca/La2-I1	91.35(2)	La1-I2-La1	95.46(2)

$Sr_1La_6I_{12}Os$

An irregular black crystal was chosen for x-ray diffraction from a reaction loaded $Sr_2La_6I_{12}Os$. A summary of data collection and refinement parameters is given in Table 31. Data collection was performed at room temperature on a Rigaku AFC6 automated diffractometer using Mo Kα radiation. A random search resulted in 25 reflections with an average intensity of 8286 counts per second. Twenty of these reflections could be indexed to a R-centered hexagonal unit cell. The other five reflections had an average intensity of 3536 counts per second and were probably due to a small crystallite or debris on the surface of the main crystal. All of the reflections had smooth, sharp peak profiles with no doubling or shoulders. Diffractometer software suggested the Laue class $\bar{3}$. A hemisphere (+h, ±k, ±l) of data was collected between the 2θ limits of 3° and 60 °, followed by measurement of six ψ-scans which resulted in a relative transmission factor range of 0.5528 – 1.0000.

Structure solution began with data reduction, which included Lorentz-polarization corrections and an empirical absorption correction based on an averaged transmission curve. Intensity statistics indicated a centrosymmetric space group. Systematic absences in the data set indicated the space group $R\bar{3}$ (#148) or one noncentrosymmetric space group $R3$ (#146). Direct methods gave an acceptable solution in the expected centrosymmetric group. All data with I>0 were averaged, resulting in R(int) of 13.5 %. The heavy atoms were located first, followed by the Sr. Isotropic refinement of 100 % Sr at the isolated cation site resulted in R1, *w*R2 of 9.8, 27.8 % with Ueq similar to those of the other atoms. A refinement of the Sr occupancy (with Ueq fixed) failed to converge, as did a refinement of a second La atom sharing the position with Sr (with Ueq for La2 constrained to the same value as Sr), regardless of the initial percentages of Sr and La, so the position was reset to 100 % Sr. The

Table 31. Crystallographic data for $Sr_1La_6I_{12}Os$

Space group, Z	$R\bar{3}$ (#148), 3
a, c (Å)[a]	16.083(2), 11.366(3)
V (Å^3)	2546.1(9)
d_{calc} (g/cm^3)	5.174
μ (Mo Kα, mm^{-1})	23.654
Crystal dimensions (mm)	0.12 x 0.12 x 0.09
Diffractometer	Rigaku AFC6
Radiation, wavelength (Å)	Mo Kα, 0.71069
Scan mode	2θ–ω
Octant measured	+h, ±k, ±l
$2\theta_{max}$ (°)	60
No. measured reflections	5077
No. independent reflections, R(int) (I>0)	1641, 0.1353
No. independent observed reflections (I $\geq 2\sigma_I$)	930
No. of variables	33
Relative transmission factor range	0.5528–1.0000
Extinction parameter	0.01(5) x 10^{-5}
Goodness of fit	1.003
R1, *w*R2 (I $\geq 2\sigma_I$)	0.0509, 0.0840
R1, *w*R2 (all data)	0.1283, 0.1029
Largest residual peaks (e/Å^3)	1.81 (0.8 Å from I2), -1.55 (1.0 Å from Sr)

[a] refined cell constants from 20 Guinier lines

final Sr Ueq is comparable to the other atomic Ueq. The anisotropic refinement resulted in final R1, *w*R2 of 5.1, 10.3 %. Table 32 lists positional and thermal parameters with their associated errors. The largest peak in the final difference Fourier map was 1.81 e/Å^3, located 0.8 Å from I1. The largest negative peak was -1.55 e/Å^3 at 1.04 Å from Sr. There were no problems with the anisotropic thermal parameters. Important interatomic distances and bond angles are presented in Tables 33 and 34, respectively.

Table 32. Positional and thermal parameters for $Sr_1La_6I_{12}Os$

Atom	x	y	z	Ueq	Occ.	U_{11}	U_{22}	U_{33}	U_{23}	U_{13}	U_{12}
La1	0.88132(6)	0.83636(6)	0.14542(7)	0.0239(2)	1	0.0241(4)	0.0254(4)	0.0242(4)	-0.0053(4)	-0.0045(4)	0.0139(4)
I1	0.20135(6)	0.48382(6)	0.33538(8)	0.0266(2)	1	0.0266(5)	0.0267(5)	0.0265(4)	-0.0062(4)	-0.0040(4)	0.0134(4)
I2	0.07933(9)	0.31463(7)	-0.00252(9)	0.0359(3)	1	0.0477(6)	0.0206(4)	0.0392(6)	0.0074(4)	0.0193(5)	0.0169(4)
Os	0	0	0	0.0143(3)	1	0.0139(4)	U_{11}	0.0153(6)	0	0	1/2 U_{11}
Sr	0	0	1/2	0.0332(8)	1	0.040(1)	U_{11}	0.020(2)	0	0	1/2 U_{11}

Table 33. Important interatomic distances in $Sr_1La_6I_{12}Os$ (Å)

Os–La1	(x6)	2.873(1)	La1–I1	3.265(1)
Sr–I1	(x6)	3.2497(9)	La1–I1	3.277(1)
La1–I2[a]		3.229(1)	La1–La1	4.053(3)
La1–I2[a]		3.232(1)	La1–La1	4.075(2)
La1–I2[b]		3.425(1)	I1–I2[c]	4.360(2)

[a] waist bridging I2
[b] exo bonded I2
[c] shortest I–I contact

Table 34. Important bond angles in $Sr_1La_6I_{12}Os$ (°)

La1-Os-La1	180.00(4)	Sr-I1-La1	91.35(3)
La1-Os-La1	90.31(2)	Sr-I1-La1	91.13(3)
La1-Os-La1	89.69(2)	La1-I1-La1	77.05(3)
I1-Sr-I1	180.00(3)	La1-I2-La1	77.69(4)
I1-Sr-I1	88.83(2)	La1-I2-La1	172.10(4)
I1-Sr-I1	91.17(2)	La1-I2-La1	94.54(4)

$(Sr_{0.526}La_{0.474})La_6I_{12}Os$

An irregular black crystal was chosen for x-ray diffraction from a reaction loaded $Sr_{0.5}La_{6.5}I_{12}Os$. A summary of data collection and refinement parameters is given in Table 35. Data collection was performed at room temperature on a Rigaku AFC6 automated diffractometer using Mo Kα radiation. A random search resulted in 25 reflections with an average intensity of 6461 counts per second. All of these reflections could be indexed to a R-centered hexagonal unit cell. Diffractometer software suggested the Laue class $\bar{3}$. A hemisphere (±h, +k, ±l) of data was collected between the 2θ limits of 3° and 60 °, followed by measurement of ten ψ-scans which resulted in a relative transmission factor range of 0.2249 – 1.0000.

Structure solution began with data reduction, which included Lorentz-polarization corrections and an empirical absorption correction based on an averaged transmission curve. Intensity statistics indicated a centrosymmetric space group. Systematic absences in the data set indicated the space group $R\bar{3}$ (#148) or one noncentrosymmetric space group $R3$ (#146). Direct methods gave an acceptable solution in the expected centrosymmetric group. All data with I>0 were averaged, resulting in R(int) of 10.8 %. The heavy atoms were located first, followed by the Sr. Isotropic refinement of 100 % Sr at the isolated cation site resulted in R1, *w*R2 of 11.1, 20.8 % with Ueq about twice as large as the average Ueq of the other atoms. Further isotropic refinement of the Sr occupancy failed to converge. A second La atom was added, sharing the position with Sr (with Ueq for La2 constrained to the same value as Sr). Isotropic refinement of the mixed occupancy resulted in 52.6(2) % Sr, 47.4(2) % La2. The final Sr/La2 Ueq was comparable to the other Ueq. The anisotropic refinement

Table 35. Crystallographic data for $(Sr_{0.526}La_{0.474})La_6I_{12}Os$

Space group, Z	$R\bar{3}$ (#148), 3
a, c (Å)[a]	16.106(2), 11.145(2)
V (Å^3)	2503.7(7)
d_{calc} (g/cm^3)	5.241
μ (Mo Kα, mm^{-1})	23.960
Crystal dimensions (mm)	0.10 x 0.10 x 0.09
Diffractometer	Rigaku AFC6
Radiation, wavelength (Å)	Mo Kα, 0.71069
Scan mode	2θ–ω
Octant measured	±h, +k, ±l
$2\theta_{max}$ (°)	60
No. measured reflections	3434
No. independent reflections, R(int) (I>0)	1638, 0.1077
No. independent reflections (I $\geq 2\sigma_I$)	827
No. of variables	34
Relative transmission factor range	0.2249–1.0000
Extinction parameter	1.1(2) x 10^{-4}
Goodness of fit	0.955
R1, *w*R2 (I $\geq 2\sigma_I$)	0.0580, 0.1182
R1, *w*R2 (all data)	0.1536, 0.1499
Largest residual peaks (e/Å^3)	3.28 (1.29 Å from Os), -3.14 (1.06 Å from La1)

[a] refined cell constants from Rigaku diffractometer

resulted in final R1, *w*R2 of 5.8, 15.0 %. Table 36 lists positional and thermal parameters with their associated errors.

The largest peak in the final difference Fourier map was 3.28 e/Å^3, located 1.28 Å from Os. The largest negative peak was -3.14 e/Å^3 at 1.06 Å from La1. There were no problems with the anisotropic thermal parameters. Important interatomic distances and bond angles are presented in Tables 37 and 38, respectively.

Table 36. Positional and thermal parameters for $(Sr_{0.526}La_{0.474})La_6I_{12}Os$

Atom	x	y	z	Ueq	Occ.	U_{11}	U_{22}	U_{33}	U_{23}	U_{13}	U_{12}
La1	0.50386(9)	0.21577(8)	0.1850(1)	0.0231(3)	1	0.0197(6)	0.0216(6)	0.0290(5)	0.0024(4)	0.0029(4)	0.0111(5)
I1	0.61473(9)	0.14800(9)	-0.0040(1)	0.0276(3)	1	0.0233(7)	0.0284(8)	0.0309(5)	-0.0053(5)	-0.0017(4)	0.0128(6)
I2	0.4319(1)	0.0198(1)	0.3352(1)	0.0338(4)	1	0.0312(8)	0.0169(6)	0.0407(7)	0.0059(5)	-0.0108(5)	0.0025(6)
Os	0	0	0	0.0136(4)	1	0.0111(5)	U_{11}	0.0186(7)	0	0	½ U_{11}
Sr	0	0	1/2	0.044(2)	0.526(2)	0.026(2)	U_{11}	0.080(3)	0	0	½ U_{11}
La2	0	0	1/2	0.044	0.474(2)	0.026	U_{11}	0.080	0	0	½ U_{11}

Table 37. Important interatomic distances in $(Sr_{0.526}La_{0.474})La_6I_{12}Os$ (Å)

Os–La1	(x6)	2.869(1)	La1–I1	3.281(2)
Sr/La2–I1	(x6)	3.225(1)	La1–I1	3.289(2)
La1–I2[a]		3.233(2)	La1–La1	4.053(2)
La1–I2[a]		3.235(2)	La1–La1	4.061(2)
La1–I2[b]		3.415(2)	I1–I1[c]	4.333(2)

[a] waist bridging I2
[b] exo bonded I2
[c] shortest I–I contact

Table 38. Important bond angles in $(Sr_{0.526}La_{0.474})La_6I_{12}Os$ (°)

La1-Os-La1	180.00(4)	Sr/La2-I1-La1	89.16(4)
La1-Os-La1	90.01(3)	Sr/La2-I1-La1	89.02(4)
La1-Os-La1	89.90(3)	La1-I1-La1	76.34(5)
I1-Sr/La2-I1	180.00(3)	La1-I2-La1	77.61(6)
I1-Sr/La2-I1	88.52(3)	La1-I2-La1	172.84(6)
I1-Sr/La2-I1	91.48(3)	La1-I2-La1	95.25(5)

General Summary of Single Crystal X-Ray Diffraction Results

The single crystal x-ray diffraction results show that an alkali or alkaline earth metal atom will substitute for the isolated lanthanide atom without destruction of the $R_7X_{12}Z$ structure to form $AR_6X_{12}Z$. Successful substitutions occurred for A = Li, Na, Ca, Sr with R = La, X = I and Z = Os. Although substitution by Mg was suggested by the analysis of the Guinier lattice constants and unit cell volume calculations, no crystal of $MgLa_6I_{12}Z$ of sufficient quality was found for single crystal x-ray diffraction experiments. The compositions $NaLa_6I_{12}Fe$, $NaPr_6I_{12}Ir$ and $CaLa_6I_{12}Co$ also resulted in substituted $AR_6I_{12}Z$-type compounds. It is reasonable to suppose that similar substitutions are possible in all $R_7X_{12}Z$, so long as the relative stabilities of alternate phases do not change with the addition of the heterocation.

Comparison of the interatomic distances revealed that the A – I1 distances increased with larger A cations (3.108, 3.225 Å in $(Li_{0.967}La_{0.033})La_6I_{12}Os$ and $(Sr_{0.526}La_{0.474})La_6I_{12}Os$, respectively). Also, as the fraction of A increased, the A – I1 distance usually increased (for A = Na, Sr) although the opposite seemed to be true for the A = Ca structures where the observed distances were 3.139 and 3.165 Å for $(Ca_{0.906}La_{0.094})La_6I_{12}Os$ and $(Ca_{0.621}La_{0.379})La_6I_{12}Os$, respectively. In contrast, the La – La, La – Os, and La – I distances remained almost constant from one crystal to another. The Pr – Pr, Pr – Ir, and Pr – I distances in $(Na_{0.887}Pr_{0.113})Pr_6I_{12}Ir$ were slightly shorter than the corresponding distances in the La compounds, as expected from the smaller size of Pr compared to La (crystal radii[48] = 1.13, 1.172 Å for Pr, La, respectively). Similarly, the observed La – Fe and La – Co distances were a little shorter than La – Os distances (~ 2.84 and 2.87 Å, respectively).

The occupancy refinements suggest that essentially all the loaded A substitutes for R2 in the structure, but there often remains a small balance of R2 for reactions loaded $A_1La_6I_{12}Os$. In reactions loaded with exactly one A per formula unit, the refined amount of A ranged between 80.1 and 96.7 % A. This rather large range may be due to errors in measuring alkali or alkaline earth metal reactants, evaporative losses during the welding process, and/or off-stoichiometries caused by formation of ROI during reaction (this impurity, though usually $\leq$10 % of the products, effectively sequesters a portion of the loaded R and I). Likewise, crystals from reactions loaded with half an equivalent of A per formula unit resulted in refined occupancies close to 50 % A, such as $(Ca_{0.621(2)}La_{0.379(2)})La_6I_{12}Os$ and $(Sr_{0.526(2)}La_{0.474(2)})La_6I_{12}Os$. These compositions suffer from the same sources of error as those loaded with one equivalent of A, possibly to even greater extent because of the extremely small quantity of A (or AI or AI_2) needed to provide half an equivalent (for a total reaction mass of 0.25 g, about 14 mg CaI_2 or 4 mg Sr is required). On the other hand, reactions loaded with excess alkali or alkaline earth metal usually could not be refined (the refinement diverged) with a second type of atom sharing the A position; instead, these refinements led to realistic results only when the A occupancies were reset to 100 %, as in the examples loaded $Na_4La_9I_{22}Os_3$ and $Sr_2La_6I_{12}Os$. There was one exception, loaded $Ca_2La_9I_{22}Os_3$, which refined to $(Ca_{0.933(2)}La_{0.067(2)})La_6I_{12}Os$. Of the three, the strontium example was loaded closest to correct $AR_6X_{12}Z$ stoichiometry, and yet the only other phases observed in Guinier powder patterns of the reaction products were roughly 25 % LaI_3 and 10 % Os in both the Na and Ca cases; no other phases were found in the Sr reaction products. The thermal parameters for the A cations were often two to five times larger than thermal parameters of the other atoms in a structure, which is not unusual for alkali or

alkaline earth metal cations in voids. The sum of crystal radii for six-coordinate A cations and I^- was always within about 0.1 Å of the observed A–I distances from the single crystal structure refinement (crystal radii[48] (Å): $I^- = 2.06$, $Li^+ = 0.90$, $Na^+ = 1.16$, $Ca^{+2} = 1.14$, $Sr^{+2} = 1.32$, $La^{+3} = 1.172$). In crystals where the A position was occupied by mixed A/R2 cations, the experimental distance usually decreased with greater R2 content, suggesting that the R^{+3} cations more strongly polarize the negatively-charged surrounding iodines than do the +1 alkali or +2 alkaline earth metal cations.

Although rhombohedral $Zr_6I_{12}Z$ are known (see Chapter 1), the analogous lanthanide compounds "$R_6I_{12}Z$" have never been prepared. In no case was it possible to refine the isolated cation position as less than fully occupied, whether by a single type of atom or by a combination of two atoms. Attempts to refine the position fractionally occupied by either A or R2 alone (in other words, with the site partially "empty") invariably failed, leading to unreasonable Ueq as well as large residual electron density.

The structures with the largest final R1, *w*R2 values (5.7, 14.4 % for $Na_1La_6I_{12}Os$; 9.1, 20.3 % for $(Na_{0.887}Pr_{0.113})Pr_6I_{12}Ir$; 6.1, 12.3 % for $(Na_{0.954}La_{0.046})La_6I_{12}Fe$; 5.8, 11.8 % for $(Sr_{0.526}La_{0.474})La_6I_{12}Os$) also had larger residual electron densities and larger relative transmission factor ranges, which indicates that the problems with these refinements are probably due to poor corrections for absorption. Incomplete empirical absorption corrections by the ψ-scans may have been due to irregularly shaped crystals. None of the crystals examined presented evidence of twinning, such as was found in at least one earlier study of the $R_7X_{12}Z$-type structure.[7] Placement of whole atoms on sites of residual electron density resulted in vanishing Ueq for neighboring atoms and higher R1, *w*R2. Calculation of the

dimensions of void spaces in the structure (see below) agree with the conclusion that there are no other atom sites suitable for occupation in $AR_6I_{12}Z$ compounds.

Energy-Dispersive Spectroscopy

Two single crystals were chosen for EDS analysis. These were from reactions with loaded composition $Sr_{0.5}La_{6.5}I_{12}Os$ and $Ca_{0.5}La_{6.5}I_{12}Os$; diffraction data on these same crystals (see above) had previously been refined to stoichiometries of $(Sr_{0.526(2)}La_{0.474(2)})La_6I_{12}Os$ and $(Ca_{0.621(2)}La_{0.379(2)})La_6I_{12}Os$, respectively. Small samples of powdered, crystalline LaI_3, SrI_2 and CaI_2 were also examined and used as calibration standards. Four areas on each of the two crystals were analyzed and the elemental compositions calculated. The results and averaged compositions are given in Table 39. The Sr crystal showed little variation in composition among the four areas selected, but the Ca crystal was more diverse. Some of this variability could be due to sample irregularities, for example scattering of the electron beam by an uneven or canted crystal surface or absorption by carbon-based grease remaining from sample preparation. Also, the loaded composition suffers from possible errors associated with measuring and transferring the reactants, as discussed in the section on single crystal x-ray structures. Additionally, if the distribution of Sr or Ca is random, as assumed, then some parts of the single crystal might have higher (or lower) local concentrations of these elements compared to the average concentration over the entire crystal, but the sampled areas were large enough to have encompassed several hundred unit cells. Generally, the EDS results agree respectably well with the compositions refined from x-ray data. In each case, where half of one equivalent of Sr or Ca was loaded, about the same amount was observed (0.4 Sr but 0.33–0.50 Ca per formula unit). All of these measurements gave less Sr or Ca than the corresponding x-ray crystal structure, and all but

one area of the Ca crystal showed six or more equivalents of La per formula unit. The one exception also yielded lower-than-expected amounts of Ca and I.

Void Space Calculation

The void spaces in the structure of $LiLa_6I_{12}Os$, using atomic coordinates from the single crystal x-ray refinement of $(Li_{0.967}La_{0.033})La_6I_{12}Os$, were calculated with the Li position at 0, 0, ½ empty to show that this site was the largest hole available. The position had six I1 neighbors at 3.10 Å and was reasonably sized for a six coordinate Li^+ (sum of crystal radii of Li^+ and $I^- = 2.96$ Å). The second largest void space at 0.77, 0.09, 0.50 had two I1 and two I2 nearest neighbors at 3.12 Å as well as one I1 and one I2 next-nearest neighbors at 3.22 Å. The third largest void had three iodine nearest neighbors at 2.69 Å, which was less than the sum of crystal radii for even four-coordinate Li^+ and I^- (2.79 Å). All of the other voids were smaller still; the eight largest voids are summarized in Table 40. If a second Li site exists

Table 39. EDS results for $Sr_{0.5}La_{6.5}I_{12}Os$ and $Ca_{0.5}La_{6.5}I_{12}Os$ crystals[a]

Area	$Sr_{0.5}La_{6.5}I_{12}Os$	$Ca_{0.5}La_{6.5}I_{12}Os$
1	$Sr_{0.4(3)}La_{7.4(9)}I_{14.2(9)}Os$	$Ca_{0.40(6)}La_{7.2(9)}I_{12(1)}Os$
2	$Sr_{0.4(3)}La_{6.9(7)}I_{12.7(9)}Os$	$Ca_{0.50(7)}La_{6(1)}I_{12(1)}Os$
3	$Sr_{0.4(2)}La_{6.0(9)}I_{11.4(9)}Os$	$Ca_{0.33(6)}La_{4.9(9)}I_{10(1)}Os$
4	$Sr_{0.4(2)}La_{6.8(9)}I_{13(1)}Os$	$Ca_{0.45(7)}La_{6(1)}I_{11(1)}Os$
Average	$Sr_{0.4(5)}La_{6.8(9)}I_{13(1)}Os$	$Ca_{0.4(1)}La_{6(1)}La_{11(1)}Os$
X-Ray	$(Sr_{0.526(2)}La_{0.474(2)})La_6I_{12}Os$	$(Ca_{0.621(2)}La_{0.379(2)})La_6I_{12}Os$

[a] EDS compositions normalized to 1.0 equivalent Os per formula unit

in the structure, it would most probably be the second-largest void at 0.77, 0.09, 0.50 but no suitable electron density has been observed at that position by x-ray diffraction. These calculations did not take into account possible effects of the Li cation on the other atoms in the structure of $(Li_{0.967}La_{0.033})La_6I_{12}Os$. For example, if the cation strongly attracts the surrounding iodines, the result may be contraction of the Li–I distances and consequences to other interatomic distances and therefore, underestimation of the "true" size of the void. There is no lanthanide example of rhombohedral "$R_6X_{12}Z$" (without an atom at 0, 0, ½) available for comparison.

Table 40. Largest void spaces in $LiLa_6I_{12}Os$

Void	x	y	z	Neighbors
1[a]	0	0	½	6 I at 3.10 Å[b]
2	0.77	0.09	0.50	4 I at 3.12, 2 I at 3.22 Å
3	0.55	0.59	0.42	3 I at 2.69 Å
4	0.10	0.74	0.43	2 I at 2.65, 2 I at 2.82 Å
5	0.15	0.62	0.27	2 I at 2.61, I at 2.69 Å
6	0	0	0.74	3 La1 at 2.60, I at 2.74 Å
7	0.13	0.18	0.08	3 La1 at 2.59 Å
8	0.02	0.12	0.52	I at 1.85 Å

[a] this is the position of La2 in $La_7I_{12}Os$
[b] error levels of the distances were not included in the calculation output but are probably ±0.01 or less, reflecting the uncertainty of the single crystal x-ray diffraction data

Solid State Nuclear Magnetic Resonance

Room temperature ^{7}Li MAS–NMR on a sample of solid $LiLa_6I_{12}Os$ showed a sharp peak centered at -10.22 ppm (vs. solid LiCl) accompanied by a pair of spinning sidebands (Figure 4). The sample was produced from a reaction with loaded composition $Li_3La_6I_{12}Os$, using Li metal, but a x-ray powder pattern of the products did not show evidence of any phases other than $LiLa_6I_{12}Os$. Excess Li may have been lost during loading or welding processes, or it may have formed a very small quantity of LiI that was not detectable by Guinier x-ray powder diffraction or by NMR. For comparison, the ^{7}Li NMR spectrum of LiI showed a sharp resonance at about -5 ppm vs. LiCl while the spectrum of $LiI{\cdot}xH_2O$ showed at least two overlapping peaks between -2 and -5 ppm vs. LiCl. The single NMR peak confirmed a single Li position of high symmetry in the $LiLa_6I_{12}Os$ compound and fit with the single crystal picture where Li was at the center of a (nearly octahedral) trigonal antiprismatic arrangement of six I atoms. None of the expected two pairs of satellites were observed, probably because they were weak and lost in the background. The absence of any other peaks in the spectrum is further indication that there are no other significant Li sites in the structure.

In one previous static ^{7}Li NMR study of cubic $Li_2Zr_6Cl_{15}Mn$,[49] a similar compound made up of Mn-centered Zr_6 clusters which are surrounded by edge-bridging Cl^{i} atoms and interconnected by Cl^{a-a} bridges, the spectrum showed a triplet centered at -0.4 ppm (vs. solid LiCl). The Li in the Zr compound had six Cl neighbors arranged nearly octahedrally (D_{2d} site symmetry) but the site was only one-third occupied by Li. The greater chemical shift in the Zr compound, as compared to the $LiLa_6I_{12}Os$ sample, is probably due to decreased shielding corresponding to the more electronegative Cl neighbors.

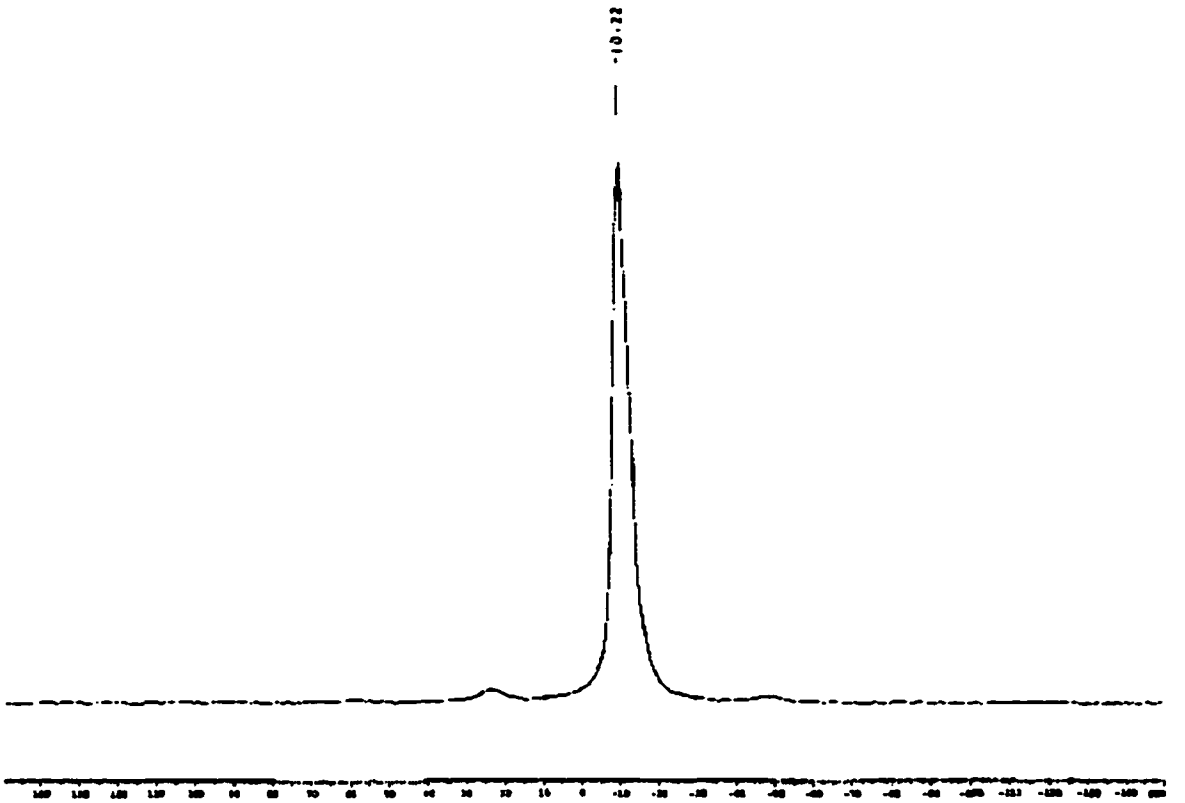

Figure 4. ^{7}Li NMR of solid $LiLa_6I_{12}Os$, with LiCl (s) as reference. The single peak is centered at -10.22 ppm, and there are spinning sidebands on either side.

Lattice Dimensions

Unit cell constants of various $ALa_6I_{12}Z$ compounds refined from Guinier powder patterns are shown in Table 41. This list includes refinements from powder patterns composed of at least 90 % $ALa_6I_{12}Z$-type products. In addition, refinements on less than ten diffraction lines were discarded. Up to 37 diffraction lines were matched on individual experimental powder patterns to the corresponding $ALa_6I_{12}Z$ calculated pattern, although the average number of lines was 19, and over half of the powder patterns examined fell within the range of 19 ± 4 lines. In cases where powder patterns from two or more reactions with identical loaded compositions were used in lattice constant refinements (this occurred only nine times), the refinement of each composition with the greatest number of matched lines was reported.

The dimensions of the compound do not change much as Z varies within a period, keeping A constant, which agrees with previous studies on other reduced halide cluster compounds.[7,13] The five compounds represented in Figure 5 had loaded stoichiometry $NaLa_6I_{12}Z$. It was expected that the unit cell volume would increase when the interstitial element was changed from a 3d to a 4d to a 5d transition metal. Fifth period transition metal atoms are generally larger than third or fourth period transition metal atoms, which explains the difference in unit cell dimensions as Z varies between periods. Two of these compositions, $NaLa_6I_{12}Os$ and $NaLa_6I_{12}Ir$ have been confirmed by single crystal x-ray diffraction. The anomalous Z = Ru volume was much smaller than expected. More examples of $NaLa_6I_{12}Z$ compounds with 3d and 4d transition metal interstitials are needed before reliable conclusions can be drawn, but the isolated cation site in Z = Co, Ru compounds may have had a more variable Na/La2 composition, with respect to the

compounds with fifth period transition metal interstitials, which would affect the unit cell volume (see below).

When A, the isolated cation, was changed while holding constant the rest of the composition, it was observed that the lattice constant *a* increased as A went from Li to Na, but decreased for alkaline earth metals in the order Mg > Ca > Sr. The other cell constant, *c*, likewise increased from A = Li to A = Na, but the alkaline earth metals reversed the order, increasing down the group as A went from Mg to Sr. The net effect of this was that the unit cell volume of $ALa_6I_{12}Os$ increased with larger A (Figure 6); and changed to the *c* dimension dominated the overall result. This agreed with data from single crystal x-ray studies, which showed that the only bond distances that changed significantly among examples of $ALa_6I_{12}Os$ were the A–I1 contacts along the *c* direction. These increased noticeably as the size of the cation A increased (from 3.11 Å when A = Li to 3.25 Å when A = Sr) and accounted for nearly all of the changes to the unit cell volume. Compounds with A = Li, Mg were indistinguishable from unsubstituted $La_7I_{12}Os$ (with La2 in the isolated cation position) on the basis of unit cell dimensions alone, even though the radii of Li^+ and Mg^{+2} are rather smaller than that of La^{+3} (0.9, 0.86 and 1.172 Å, respectively, for six-coordinate ions[48]). The greater coulombic attraction between La^{+3} and the six surrounding I^- may explain why the volume of $La_7I_{12}Os$ appears smaller than expected from radii alone.

The dimensions of $Na_xLa_6I_{12}Os$, summarized in Table 42, also increased as greater amounts of the alkali metal were loaded into the reaction. The unit cell volume smoothly increased with *x* up to $x = 1$, then became constant (Figure 7). The dimensions of a compound loaded with $x = 0.25$ were nearly the same as those of $La_7I_{12}Os$. No further significant increase in volume was observed for loaded compositions of $x > 1$. In addition,

Table 41. Refined unit cell constants for some $ALa_6I_{12}Z$[a,b] compounds

Compound[c]	No. of Lines	a (σ), Å	c (σ), Å	Volume (σ), Å^3
$La_7I_{12}Os$	33	16.146(2)	10.971(3)	2476.9(9)
$LiLa_6I_{12}Ru$	20	16.131(2)	10.960(1)	2469.8(6)
$LiLa_6I_{12}Os$	33	16.146(5)	10.968(4)	2476(2)
$LiLa_6I_{12}Ir$	16	16.172(7)	10.957(9)	2482(3)
$LiLa_6I_{12}Pt$	22	16.187(4)	10.995(4)	2495(2)
$NaLa_6I_{12}Co$	6[d]	16.120(5)	11.041(8)	2485(2)
$NaLa_6I_{12}Ru$	25	16.188(3)	11.108(4)	2421(1)
$NaLa_6I_{12}Os$	27	16.172(2)	11.134(2)	2521.8(8)
$NaLa_6I_{12}Ir$	19	16.206(4)	11.076(4)	2519(2)
$NaLa_6I_{12}Pt$	17	16.058(4)	11.195(7)	2500(2)
$MgLa_6I_{12}Os$	37	16.148(2)	10.971(2)	2477.5(8)
$CaLa_6I_{12}Co$	11	16.06(2)	11.10(2)	2479(8)
$CaLa_6I_{12}Ni$	23	16.026(1)	11.088(1)	2466.2(4)
$CaLa_6I_{12}Os$	23	16.1089(6)	11.1556(7)	2507.0(2)
$SrLa_6I_{12}Os$	31	16.094(1)	11.345(2)	2544.8(5)

[a] space group $R\bar{3}$ (#148), $Z = 3$
[b] dimensions from least-squares refinement of Guinier powder diffraction patterns with Si as an internal standard; $\lambda = 1.540598$ Å, 23 °C
[c] loaded compositions were $ALa_6I_{12}Z$
[d] the only example of 3d transition metal Z was included despite refinement on < 10 lines

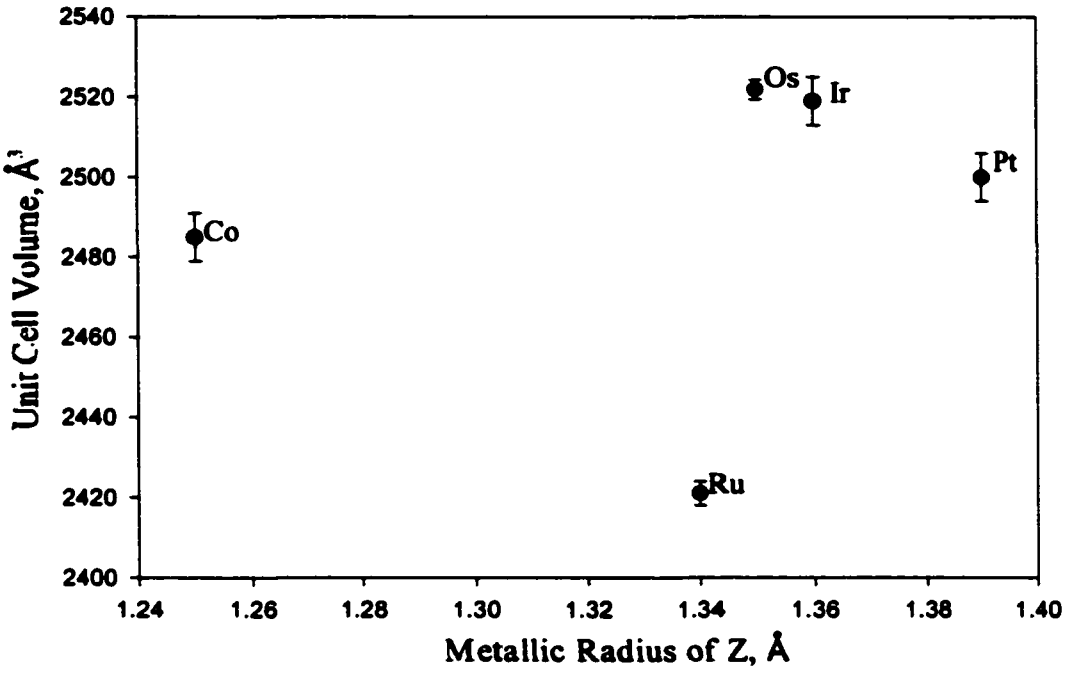

Figure 5. For the series of compounds loaded $NaLa_6I_{12}Z$, the variation of the unit cell volume with different Z elements. Points represent individual measurements. Bars indicate the 3σ error level. Although both dimensions, *a* and *c*, tend to increase with larger Z, there is much less variation within periods than between periods.

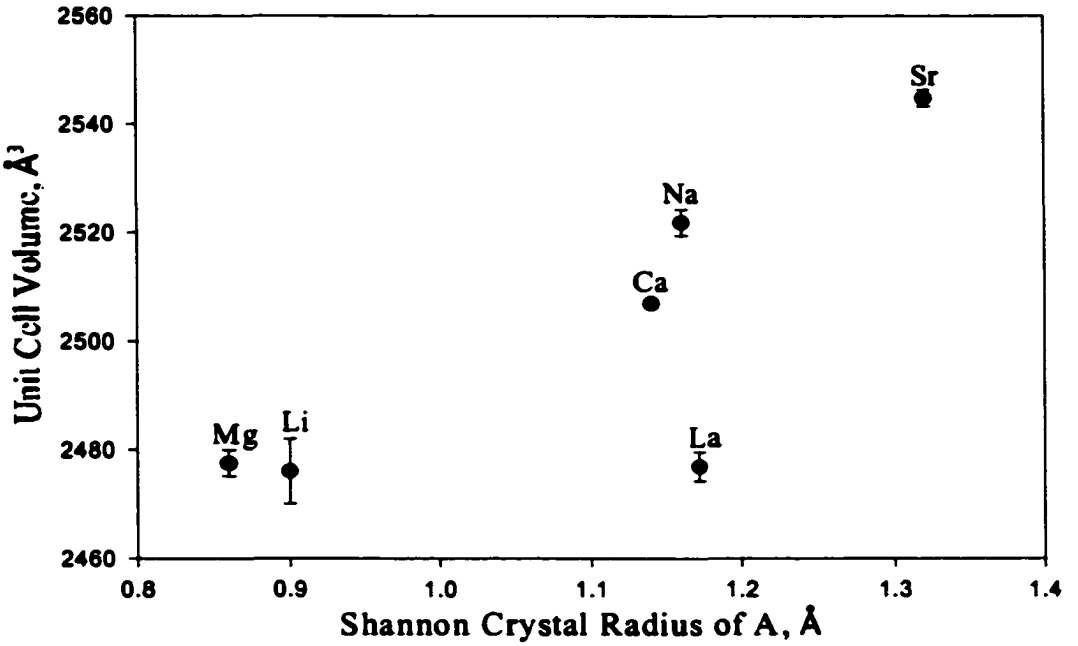

Figure 6. For the series of compounds loaded $ALa_6I_{12}Os$, the unit cell volume generally increases for larger A. Points represent individual measurements. Bars indicate the 3σ error level.

when $x > 2$ was loaded, NaI was observed in Guinier powder patterns of the reaction products–an indication that the cation site was saturated by Na. The only other phase identified in powder patterns of these reactions was LaOI (5–10 %). This can be explained by considering that La^{+3} occupies all of the R2 sites in the structure until some sodium is added to the composition. When $x < 1$, the sodium atoms replace an equivalent number of randomly distributed La^{+3}. Sites that do not become occupied by Na^{+} retain La^{+3}, producing a mixed Na^{+}/La^{+3} overall site occupancy with lattice constants intermediate between $LaLa_6I_{12}Os$ and $NaLa_6I_{12}Os$. When $x \geq 1$ is loaded, Na^{+} atoms replace nearly all of the La^{+3}, but the excess Na^{+} must form the next-most-favorable phase, which appears to be NaI under these conditions. This explanation also agrees with the analysis of the single crystal x-ray data which showed (for A = Ca, Sr) that the cation site was occupied by approximately 100 % A (~ 0 % La) when loaded with $x \geq 1$, and nearly 50 % A (~ 50 % La) when $x = 0.5$ was loaded.

A similar analysis of $Li_xLa_6I_{12}Os$ ($0.5 \leq x \leq 6.0$) compounds was complicated by the discovery that the reactant LiI, despite previous vacuum sublimation, was contaminated by $LiI{\cdot}yH_2O$ ($y \leq 3$). The parameter x was back-calculated from the amount of contaminated "LiI" loaded in each reaction, assuming the maximum $y = 3$, although y may not have been constant throughout. Also, some reactions that were loaded with metallic Li ($3.0 \leq x \leq 7.0$), therefore avoiding the stoichiometry problem, were compared to those loaded with $LiI{\cdot}yH_2O$ (corrected x). The numerical results are presented in Table 42. No clear trend of unit cell dimensions with the variation in x could be found. Only three examples gave unit cell volumes different ($>3\sigma$) from that of $La_7I_{12}Os$, but all three were slightly larger than the parent compound (Figure 8). None of the $Li_xLa_6I_{12}Os$ examples had observed volumes less

Table 42. Refined Guinier cell constants for $A_xLa_6I_{12}Os$ compounds

Loaded Composition	No. lines	*a* (Å)	*c* (Å)	Volume (Å^3)
$Na_{0.25}La_6I_{12}Os$	19	16.152(4)	10.973(4)	2479(2)
$Na_{0.5}La_6I_{12}Os$	23	16.128(3)	11.108(3)	2502(1)
$Na_{1.0}La_6I_{12}Os$	27	16.172(2)	11.134(2)	2521.8(8)
$Na_{2.0}La_6I_{12}Os$	20	16.165(2)	11.162(3)	2525.9(9)
$Li_{0.36}La_6I_{12}Os$[a]	28	16.156(4)	10.992(5)	2485(2)
$Li_{0.71}La_6I_{12}Os$[a]	33	16.146(5)	10.968(4)	2476(2)
$Li_{1.43}La_6I_{12}Os$[a]	14	16.147(5)	10.972(4)	2477(2)
$Li_{2.85}La_6I_{12}Os$[a]	17	16.182(5)	10.996(4)	2494(2)
$Li_3La_6I_{12}Os$[b]	19	16.04(1)	11.132(8)	2480(4)
$Li_{4.28}La_6I_{12}Os$[a]	13	16.15(3)	11.03(4)	2491(13)
$Li_7La_6I_{12}Os$[b]	12	16.153(4)	10.971(4)	2479(2)

[a] loaded stoichiometry corrected for $LiI{\cdot}3H_2O$
[b] loaded with metallic Li

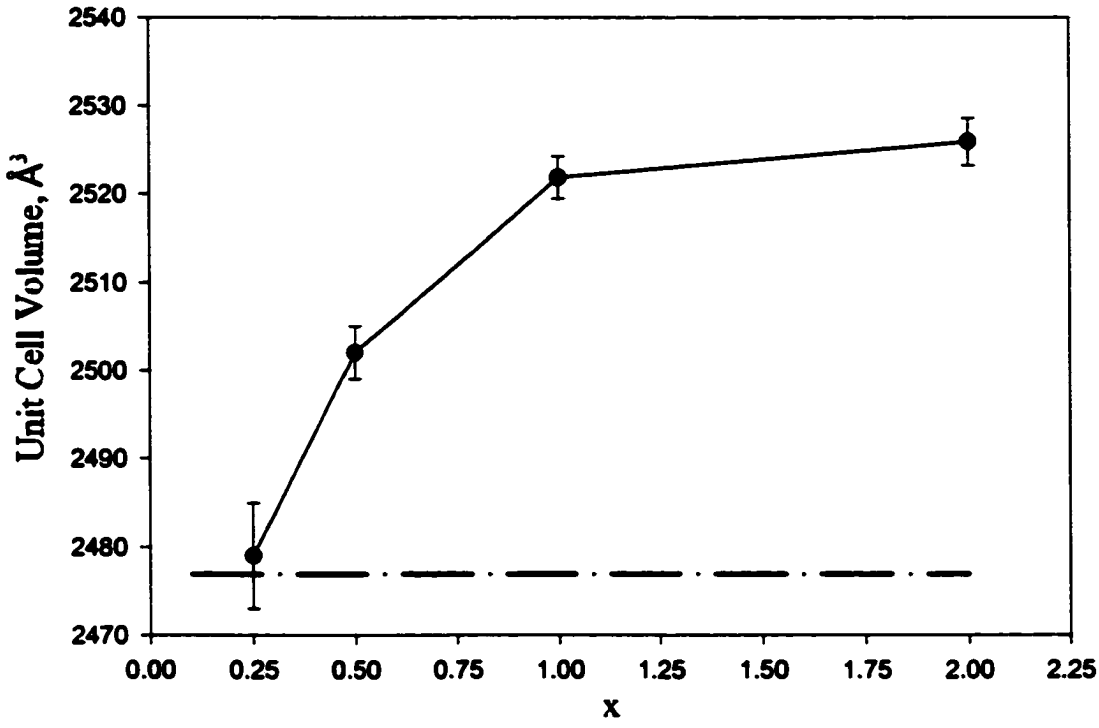

Figure 7. In the series of loaded compositions $Na_xLa_6I_{12}Os$ (solid line), the unit cell volume increased with greater x. For comparison, the volume of $La_7I_{12}Os$ (broken line) was 2476.9(9) Å^3. The volumes of the sodium compounds were similar to that of $La_7I_{12}Os$ at small x but increased with x and reached a maximum value around $x = 1$. Bars indicate 3σ error level.

than the parent. Reactions loaded with ≥4 equivalents of Li per formula unit showed 15–25 % LiI·yH$_2$O in the powder patterns of the products, while reactions with < 4 Li per formula unit did not have any. Unexpectedly, a small amount of LiI·yH$_2$O was observed in the products of reactions loaded with metallic Li as well as those loaded with the iodide, probably due to formation of LiI by excess Li followed by contact with moisture left in the reaction tube after cleaning, on the surface of the other reactants, or from the atmosphere. The only other phase observed in these reactions was LaOI (5–10 %, if any).

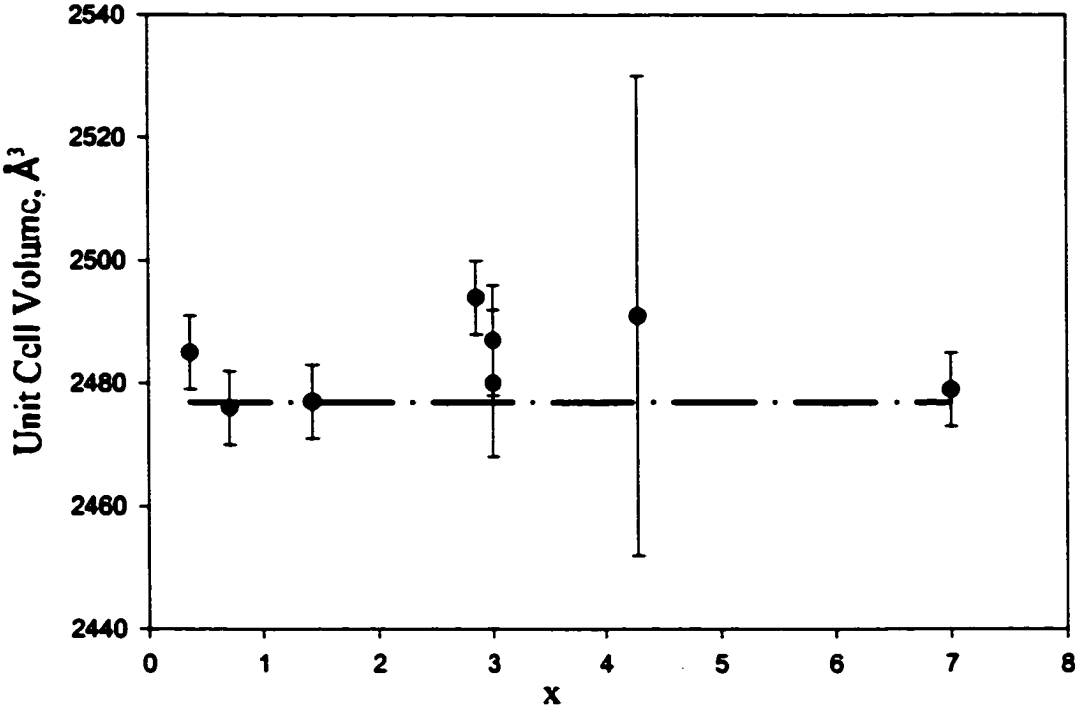

Figure 8. Unit cell volume of loaded compositions $Li_xLa_6I_{12}Os$ (circles) and $La_7I_{12}Os$ (broken line; 2476.9(9) $Å^3$). Bars indicate 3σ error level.

Comparison of Guinier X-ray Powder Pattern Intensities

In the previous discussion of the variation of lattice constants/unit cell volumes with changing A cations, it was noted that the lattice constants of $LiLa_6I_{12}Z$ and $MgLa_6I_{12}Z$ were indistinguishable from those of $La_7I_{12}Z$ (for the same Z) and, therefore, the presence of Li or Mg in the isolated position could not be inferred. Other evidence for the incorporation of these cations resulted from comparison of the Guinier powder diffraction intensities of the 1 0 1 and 1 1 0 reflections, which produced the lowest-angle lines in the pattern (near $2\theta = 10$ °). For $La_7I_{12}Os$ the 1 1 0 line was calculated to be more intense than the 1 0 1 line; while for $ALa_6I_{12}Os$ (A = Li, Mg, Na), the opposite was true. As the cation became heavier, the 1 0 1 line decreased and the 1 1 0 line increased in intensity. The two lines had about equal intensity in $CaLa_6I_{12}Os$, but the pattern of $SrLa_6I_{12}Os$ was much like that of $La_7I_{12}Os$. Thus, measuring these two lines and comparing the ratio of intensities could indicate the successful substitution of (especially the light) A for La2 in the isolated position, assuming that other factors, such as preferred orientations within the sample, did not skew the observed intensities. The examined single crystals were irregularly shaped and did not suggest any preferred orientation. Table 43 summarizes the results of an assortment of such comparisons.

The calculated pattern of $La_6I_{12}Os$ (with no atom at 0, 0, ½), which has not been found in the rhombohedral $R_7X_{12}Z$ structure type, showed line intensities that were very similar to those of $LiLa_6I_{12}Os$ (the intensity ratios were 1.61 for the Li compound and 1.69 for the hypothetical compound). Although the precision of the intensity measurement probably does not allow powder patterns of $LiLa_6I_{12}Os$ to be distinguished from that of "empty" $La_6I_{12}Os$, confusion is unlikely to occur because the latter is unknown.

In the experiments where one or more equivalent of A was loaded, the intensity ratios

were often larger than expected. For example, the lines for the sample loaded $Na_2La_6I_{12}Os$ had an intensity ratio of 1.48, compared to 1.31 for the calculated pattern. On the other hand, a sample with loaded composition $Na_{0.5}La_6I_{12}Os$ had an observed intensity ratio close to the average of the calculated ratios for $La_7I_{12}Os$ and $NaLa_6I_{12}Os$ which suggests that the sample also had intermediate composition. Unfortunately, the observed intensity ratio of the sample loaded $Ca_{0.5}La_6I_{12}Os$ was nearly identical to the ratio calculated for $CaLa_6I_{12}Os$, instead of between the calculated $La_7I_{12}Os$ and $CaLa_6I_{12}Os$ ratios.

Table 43. Guinier x-ray powder pattern line intensities[a]

Compound[b]		1 0 1	1 1 0	1 0 1/ 1 1 0
$La_7I_{12}Os$	calculated	10.20	28.60	0.36
$La_7I_{12}Os$	observed	10.01	17.30	0.58
$La_6I_{12}Os$[c]	calculated	26.90	15.90	1.69
$LiLa_6I_{12}Os$	calculated	26.40	16.40	1.61
$LiLa_6I_{12}Os$	observed	15.97	9.98	1.60
$Li_3La_6I_{12}Os$	observed	33.29	20.00	1.66
$NaLa_6I_{12}Os$	calculated	23.60	18.00	1.31
$NaLa_6I_{12}Os$	observed	25.09	17.23	1.46
$Na_{0.5}La_6I_{12}Os$	observed	6.56	7.35	0.89
$Na_2La_6I_{12}Os$	observed	18.21	12.26	1.48
$MgLa_6I_{12}Os$	calculated	22.80	18.60	1.22
$MgLa_6I_{12}Os$	observed	7.21	5.05	1.43
$CaLa_6I_{12}Os$	calculated	20.40	20.00	1.02
$CaLa_6I_{12}Os$	observed	4.92	4.92	1.00
$Ca_{0.5}La_6I_{12}Os$	observed	20.57	20.38	1.01
$Ca_2La_6I_{12}Os$	observed	16.97	13.44	1.26
$SrLa_6I_{12}Os$	calculated	15.20	23.80	0.64
$SrLa_6I_{12}Os$	observed	10.17	12.39	0.82
$Sr_2La_6I_{12}Os$	observed	17.58	18.66	0.94

[a] errors levels were not included in the intensity output; these are probably not better than ± 0.01 because of uncertainties associated with the reading of powder patterns on film by the line scanner

[b] loaded compositions of experimental powder patterns are given for observed data

[c] same structure as $La_7I_{12}Os$ but with the La2 position unoccupied

Neutron Powder Diffraction

Neutron powder diffraction was used to examine the structure of $LiLa_6I_{12}Os$. A sample (~3 cm^3) with loaded composition $Li_3La_6I_{12}Os$ (using LiI) was prepared in an extra-large Ta reaction tube. After reaction at 900 °C for seven days and cooling to room temperature, the products were examined visually and by Guinier x-ray powder diffraction. The black polycrystalline product was sealed into a vanadium canister and shipped to Argonne National Laboratory where the diffraction experiment took place at 300 K on the Intense Pulsed Neutron Source (IPNS) with the General Purpose Powder Diffractometer (GPPD) The resultant data were returned by electronic message.

The refinement using the GSAS program began with the symmetry and atomic positions (100 % Li at 0, 0, ½) previously established by x-ray diffraction in the space group $R\bar{3}$. The observed and calculated patterns fit fairly well after refining the lattice parameters and atomic positions, but the isotropic thermal parameter for Li was unacceptably large (U_{iso} = 0.40(15) $Å^2$). This value was about 20 times larger than the average U_{iso} for the other atoms. A second La was placed on the Li site and the fractional occupancy was refined isotropically to 57(3) % Li, 43(3) % La2, with U_{iso} = 0.062(16) $Å^2$ for both. Summaries of data collection and refinement parameters are given in Tables 44 and 45.

Some diffraction peaks were not accounted for by the calculated $(Li_xLa_{1-x})La_6I_{12}Os$ pattern and contamination by impurity phases was suspected. The Guinier x-ray powder pattern taken of a portion of the sample before neutron diffraction showed a small amount (10 %) of LaOI (*P4/nmm*) and LaI_3 (*P*6_3/*m*, 5 – 10 %). These two phases were added to the refinement and accounted for some of the less intense diffraction peaks. Although not seen in the x-ray powder pattern, $LiI{\cdot}yH_2O$ (*Pm*3*m*) was also observed in the neutron

Table 44. Neutron crystallographic data for $(Li_xLa_{1-x})La_6I_{12}Os$

Space group, Z	$R\bar{3}$, 3
a, c (Å)	16.1709(5), 10.9981(7)
V (Å^3)	2490.7(2)
d_{calc} (g/cm^3)	5.220
Absorption coefficient	0.032752(5)
Sample volume	3 cm^3
Diffractometer	IPNS-GPPD[a]
Detector bank 2θ (°)	145.9
Histogram scale factor	3.62(2)
R_{wp}, R_p	0.0817, 0.0533
Number of data points	4596
Reduced χ^2	3.053
Diffractometer zero point	-9.09(5)

[a] Argonne National Laboratory, Argonne, IL, U. S. Department of Energy

Table 45. Refined background and profile coefficients for $(Li_xLa_{1-x})La_6I_{12}Os$ (Å)

Background Coefficients	Profile Coefficients
1 = 0.199(4)	α = 3(3)
2 = 0.0052(5)	β_0 = 0.0403(9)
3 = -0.00026(5)	β_1 = 0.006(1)
4 = 0.000012(2)	γ_1 = 3.1(6)
5 = -0.00000027(5)	σ_1 = 109(8)
	σ_2 = -0.2(10)

refinement (5 % or less). This phase may be observed in the neutron experiment due to the more efficient scattering of neutrons by relatively light atoms. Other possible contaminant phases that were not observed in the neutron pattern were Si ($Fd\bar{3}m$), V ($Im\bar{3}m$), Ta ($Im\bar{3}m$), La ($Im\bar{3}m$), La ($P6_3/mmc$), LaI_2 ($I4/mmm$), and $La_6I_{10}Os$ ($P\bar{1}$). About five peaks, the most intense ~ 100 counts/msec (located at ~ 14 msec), remained unexplained.

The final R_{wp} and R_p were 8.2, 5.3 %, respectively, which are quite good, while the large reduced χ^2 value was probably a result of the failure to fully account for all the peaks in the spectrum. The calculated density of 5.220 g/cm^3 was slightly higher than that calculated from single crystal x-ray diffraction data, but the difference was likely due to the greater percentage of Li and ~ 14 Å^3 smaller unit cell volume in the x-ray case.

Shown in Figure 9 is the neutron diffraction pattern of $(Li_xLa_{1-x})La_6I_{12}Os$ collected at room temperature, where red crosses mark the observed data and the calculated curve of the refinement model is represented by the solid green line. Vertical marks below the pattern

mark the expected Bragg positions of the phases present in the model. The difference between the observed and calculated patterns is also plotted at the bottom of the figure. The sample was predominantly $(Li_xLa_{1-x})La_6I_{12}Os$, with small amounts of the other phases previously discussed. A summary of the refined positional parameters is given in Table 46.

Most of the results from the neutron refinement were consistent with results of x-ray diffraction. The lattice constants refined from a Guinier x-ray powder pattern (14 lines) of reaction products with loaded composition $Li_2La_6I_{12}Os$ were a = 16.147(5), c = 10.972(4) Å (unit cell volume = 2477(2) Å^3) while x-ray diffractometer-refined lattice constants (25 random reflections) for a single crystal from the same reaction were a = 16.185(3), c = 10.952(2) Å (volume = 2484(1) Å^3). Lattice constants refined from neutron data for a sample with loaded composition $Li_3La_6I_{12}Os$ were a = 16.1709(5), c = 10.9981(7) Å (volume = 2490.7(2) Å^3) while an x-ray powder pattern of a reaction with the same composition (14 lines) gave a = 16.083(4), c = 11.101(9) Å (volume = 2487(3) Å^3). These data show that both the neutron and x-ray diffractometer slightly overestimated a but underestimated c when compared to Guinier powder pattern refinements on the same loaded composition, with a net increase in unit cell volume in both cases. Despite these discrepancies, none of the values for the same parameter differed by more than ± 0.1 Å. The unit cell volume range was 7 Å^3 between the measurements on $Li_2La_6I_{12}Os$ and less than 4 Å^3 for $Li_3La_6I_{12}Os$. Much of the variation was probably due to the different refinement algorithms and the relatively few reflections used by each of the x-ray calculations.

Table 46. Positional parameters for $(Li_xLa_{1-x})La_6I_{12}Os$ by neutron powder diffraction[a]

Atom	fraction	x	y	z	U_{iso}, Å^2
La1	1	0.8821(5)	0.8376(4)	0.1519(7)	0.0230(9)
Os	1	0	0	0	0.0304(3)
I1	1	0.6155(10)	0.4644(8)	-0.008(1)	0.0241(2)
I2	1	0.6863(8)	0.7630(10)	-0.005(1)	0.0355(2)
Li	0.57(3)	1/3	2/3	1/6	0.062(2)
La2	0.43(3)	1/3	2/3	1/6	0.062(2)

[a] space group $R\bar{3}$ (#148), with lattice parameters a = 16.1709(5), c = 10.9981(7) Å, from neutron refinement

The neutron U_{iso} values ranged from 0.0230(9) for La1 to 0.0355(2) for I2 while U_{iso} for Li/La2 was slightly higher at 0.062(2). These values were comparable to the x-ray Ueq values that ranged from 0.0129(3) for Os to 0.0375(3) for I2 and 0.05(2) for Li/La2 (see Table 4). Although the definitions of U_{iso} and Ueq are equivalent, variations may have resulted from the different neutron and x-ray scattering factors for each atom. In addition, the Li/La2 site contained a much lower percentage of Li in the neutron refinement (57 %, compared to ~ 97 % from single crystal x-ray refinement) which could have resulted from absorption of neutrons by Li causing an underestimate of the Li occupancy. Important interatomic distances are presented in Table 47.

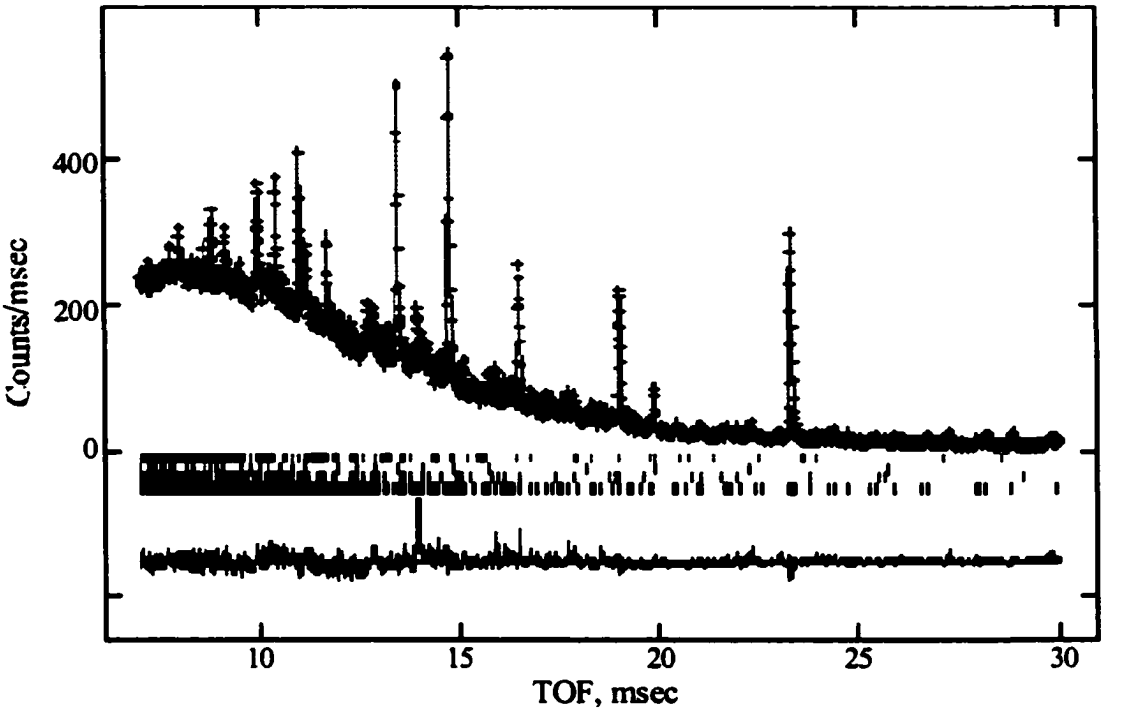

Figure 9. Neutron powder diffraction pattern for $(Li_xLa_{1-x})La_6I_{12}Os$, detector bank 2θ = 145.9 °. In the top figure, red crosses indicate observed data, the solid green line represents the calculated pattern.. Vertical ticks beneath mark the calculated positions of diffraction peaks: $(Li_xLa_{1-x})La_6I_{12}Os$ (black); LaOI (red); $LiI{\cdot}H_2O$ (blue); LaI_3 (green). At the bottom, the difference curve is plotted in purple.

Table 47. Important interatomic distances in $(Li_xLa_{1-x})La_6I_{12}Os$ (Å)

Atoms		Neutron	X-ray[a]	Atoms	Neutron	X-ray
Os–La1	(x6)	2.884(2)	2.8743(9)	La1–I1	3.245(5)	3.224(1)
Li/La2–I1	(x6)	3.158(5)	3.108(1)	La1–I1	3.269(5)	3.228(1)
La1–I2[b]		3.262(3)	3.246(1)	La1–La1	4.071(2)	4.050(2)
La1–I2[b]		3.266(3)	3.250(1)	La1–La1	4.085(2)	4.079(2)
La1–I2[c]		3.374(3)	3.414(1)	I1–I2[d]	4.370(2)	4.316(1)

[a] x-ray distances are repeated from Table 5 for comparison
[b] waist bridging I2
[c] exo bonded I2
[d] shortest I–I contact

Electrical Resistivity

Bulk resistivities of several compounds with various compositions were measured by the "Q"-method. All of the samples showed decreasing resistivity with increasing temperature, indicative of semiconducting behavior (Figure 10). The room temperature resistivity values of all samples were calculated to be between 126 and 204 $\mu\Omega\cdot$cm (Table 48). Although the electrical resistivities of most noncondensed ternary and quaternary lanthanide halide compounds have not been reported, those known have nearly always been insulators or poor semiconductors. One example, $La_{12}I_{17}Fe_2$, consists of pairs of iodine-sheathed La_6Fe octahedra in which some of the iodine atoms bridge one edge in each of two adjacent clusters ($I^{i\text{-}i}$) and others have unusual $I^{i\text{-}a\text{-}a}$ functionality, bridging the edge of one cluster and forming terminal exo-bonds to two other clusters.[50] The measured resistivity of

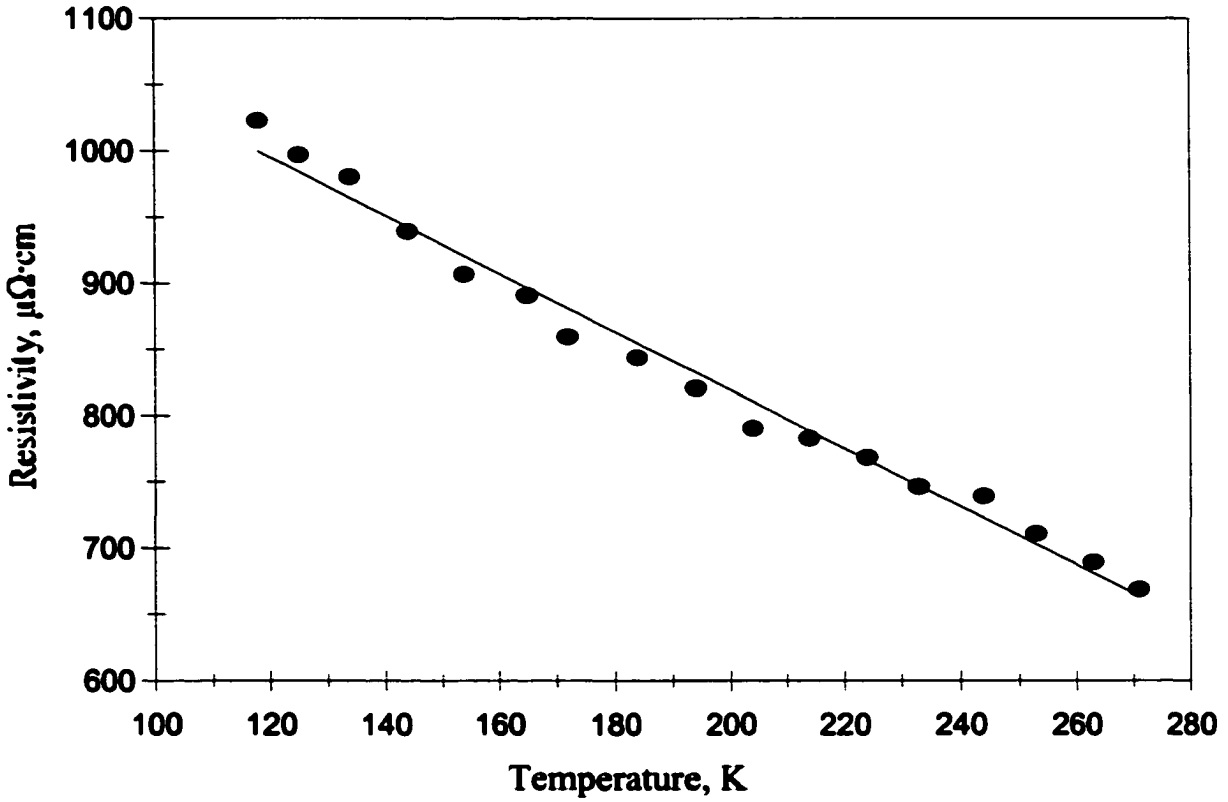

Figure 10. The electrical resistivity measured for a sample of $NaLa_6I_{12}Os$ by the "Q" method. The solid line (slope = -0.52(2)) represents the best linear fit to the data. The calculated resistivity at 298 K is 144 $\mu\Omega\cdot$cm.

Table 48. Electrical resistivities of $ALa_6I_{12}Z$ compounds by the "Q" method

Loaded Composition	ρ_{298K} ($\mu\Omega$·cm)[a]
$La_7I_{12}Os$	167, 169, 184
$Li_{0.5}La_6I_{12}Os$	172, 173
$Li_2La_6I_{12}Os$	133, 204
$NaLa_6I_{12}Os$	144, 126
$NaLa_6I_{12}Ir$	167
$Na_2La_6I_{12}Os$	173
$CaLa_6I_{12}Os$	174
$SrLa_6I_{12}Os$	149

[a] multiple values correspond to repeat experiments on the same sample

this semiconducting compound was ~ 350 $\mu\Omega$·cm at room temperature, though this may be an underestimate due to a LaI_2 impurity. In the anomalous α-$K_4R_6I_{14}Os$ (R = La, Pr) system, the octahedral clusters are connected by I^{i-a} to form planar two dimensional networks perpendicular to the *c* direction. These planar networks give rise to exceptionally low and substantially temperature-independent resistivities ~ 120 – 240 $\mu\Omega$·cm, in the range of a poor metal.[26]

Given the structure of the present compounds, there seems to be no reason to expect other than semiconducting properties. The metal clusters are linked to adjacent clusters three-dimensionally by nonplanar iodine bridges and the metal cations are isolated from the clusters as well as from each other also by iodines.

Magnetic Susceptibility

Magnetic susceptibilities were measured for nine different compositions at field strengths of either 1 or 3 Tesla and between ~5 and 300 K. Magnetization data showed no evidence of ferromagnetic impurities in any of the samples. The susceptibility data for each sample were fitted to a Curie-Weiss equation modified by an additional temperature-independent paramagnetic (van Vleck) term. The effective magnetic moment (μ_{eff}) of each sample was then calculated from the slope of $1/\chi$ vs. T and the results were collected in Table 49.

Although the sample of $NaLa_6I_{12}Os$ appeared to agree well with the modified Curie-Weiss description (Figure 11), most samples showed significant deviations, especially at higher temperatures (100–200 K and above). These – quite sharp – deviations appear in the plots of $1/\chi$ vs. T as regions of different slope and do not seem to depend either on the particular elements or the formal cluster electron count. The samples loaded $Li_2La_6I_{12}Os$ (Figure 12), $CaLa_6I_{12}Os$ (Figure 13), and $SrLa_6I_{12}Os$ (Figure 14) had the most extreme deviations from Curie-Weiss behavior while the data from samples loaded $NaLa_6I_{12}Os$ (above) and $NaLa_6I_{12}Ir$ (Figure 15) fit the equation well. Since all of the samples were made from reactions with high yields (95–100 %, estimated by powder x-ray diffraction patterns) of $ALa_6I_{12}Z$ products, and none of the samples showed evidence of ferromagnetic impurities, the possibility of deviations arising from sample contamination is low. Instead, the observed complicated susceptibilities may be due to a correspondingly more complex magnetic structure.

In one explanation, the ground state of the cluster is truly Curie-Weiss paramagnetic, producing the observed paramagnetic character at low temperatures. At higher temperatures,

Table 49. Calculated effective magnetic moments for $ALa_6I_{12}Z$ compounds

Loaded Composition	Field, T	Temperature, K	χ_0, 10^{-4} emu/mol	C, emu·K/mol	θ, K	μ_{eff}, μ_B	χ_{300}, 10^{-4} emu/mol
$Li_{0.5}La_6I_{12}Os$	3	6–300	5.95(6)	0.0302(6)	-5.1(3)	0.492	7.38(6)
$LiLa_6I_{12}Os$	1	2–350	8.77(4)	0.0270(1)	-2.26(9)	0.465	9.79(4)
$Li_2La_6I_{12}Os$	3	6–300	6.27(2)	0.0146(2)	-4.8(2)	0.342	6.93(2)
$Li_3La_6I_{12}Os$	1	2–320	9.8(1)	0.0208(3)	-1.92(7)	0.408	9.7(1)
$NaLa_6I_{12}Os$	3	6–300	11.94(3)	0.0323(3)	-5.2(1)	0.508	13.00(3)
$NaLa_6I_{12}Ir$	3	6–300	6.7(1)	0.039(1)	-7.6(6)	0.556	8.0(1)
$Na_2La_6I_{12}Os$	1	2–350	9.19(4)	0.0284(3)	-2.86(6)	0.477	10.40(4)
$CaLa_6I_{12}Os$	1	2–350	9.60(9)	0.0218(7)	-2.8(1)	0.504	10.10(9)
$SrLa_6I_{12}Os$	1	2–350	5.8(1)	0.0176(3)	-2.14(9)	0.375	6.7(1)
$SrLa_6I_{12}Os$	1	2–350	6.93(8)	0.026(2)	-1.50(3)	0.455	7.58(8)
$Li_2La_6I_{12}Os$	1	2–350	9.16(5)	0.0128(3)	-2.4(1)	0.320	9.54(5)
$Li_2La_6I_{12}Os$	5.5	2–350	5.91(2)	0.0146(2)	-5.1(1)	0.341	6.34(2)

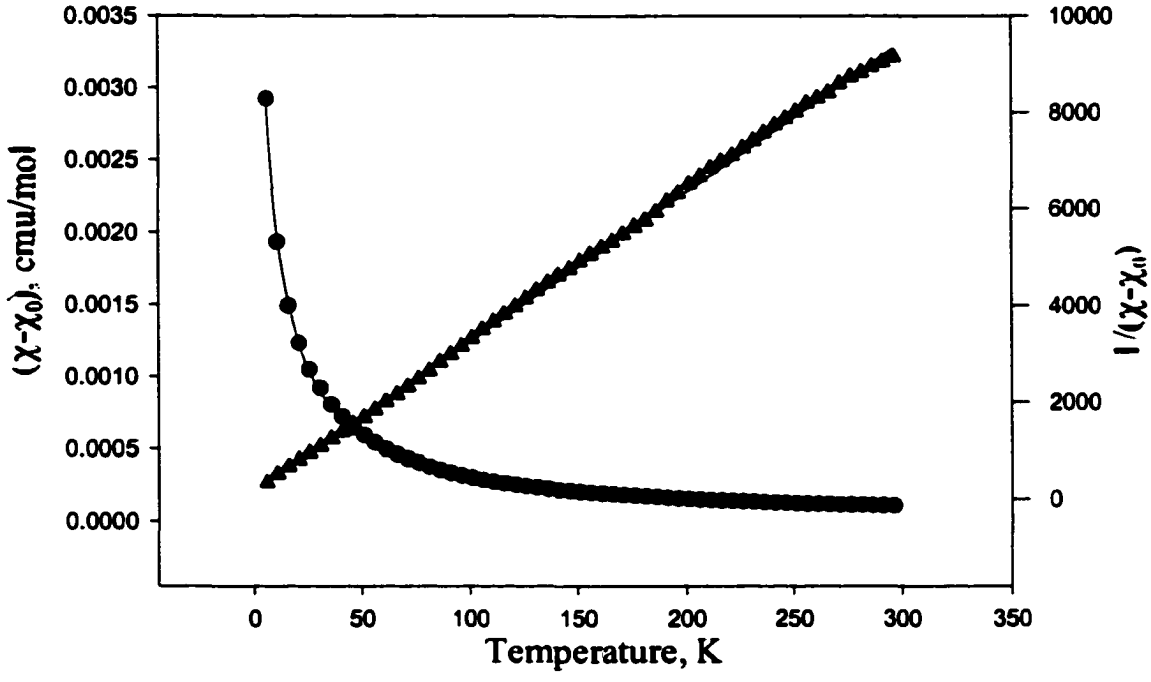

Figure 11. Magnetic susceptibility of $NaLa_6I_{12}Os$ (15 e^-/cluster) at 3 Tesla. Black circles and triangles represent χ and $1/\chi$, respectively, each corrected by a van Vleck term (χ_0), while the red lines show the Curie-Weiss fit to all data.

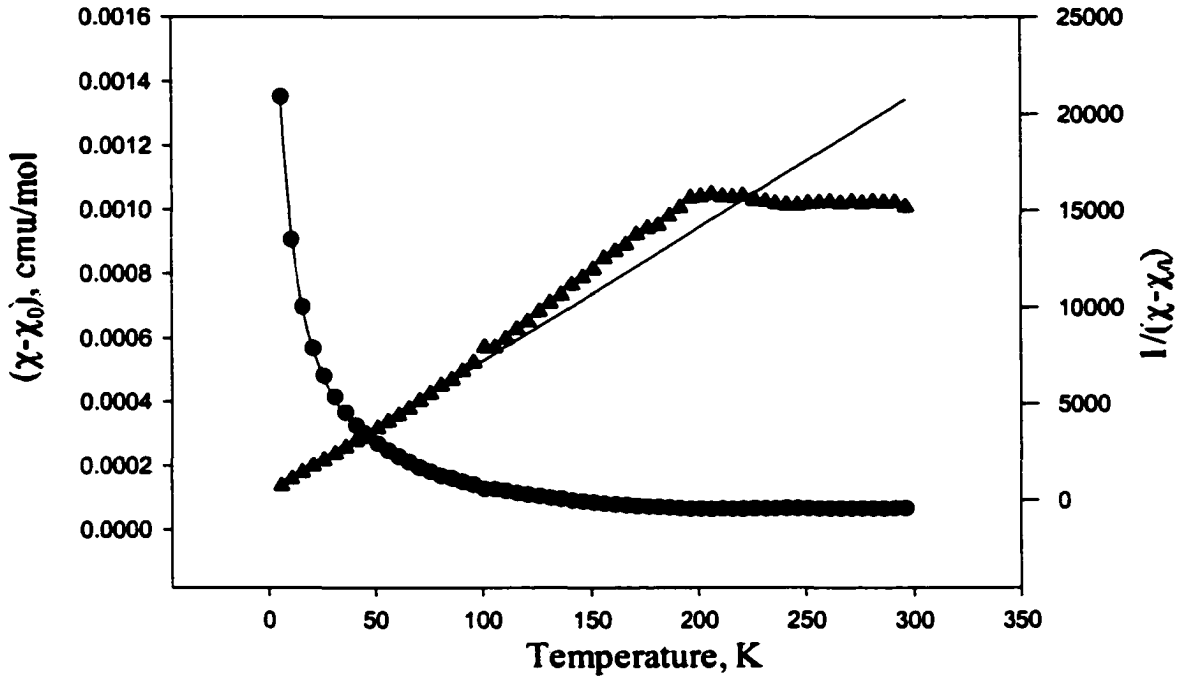

Figure 12. Magnetic susceptibility measured at 3 Tesla on a sample loaded as $Li_2La_6I_{12}Os$ (15 e^-/cluster, assuming actual composition is $LiLa_6I_{12}Os$). Black circles and triangles represent χ and $1/\chi$, respectively, each corrected by a van Vleck term (χ_0), while the red lines show the Curie-Weiss fit to all data.

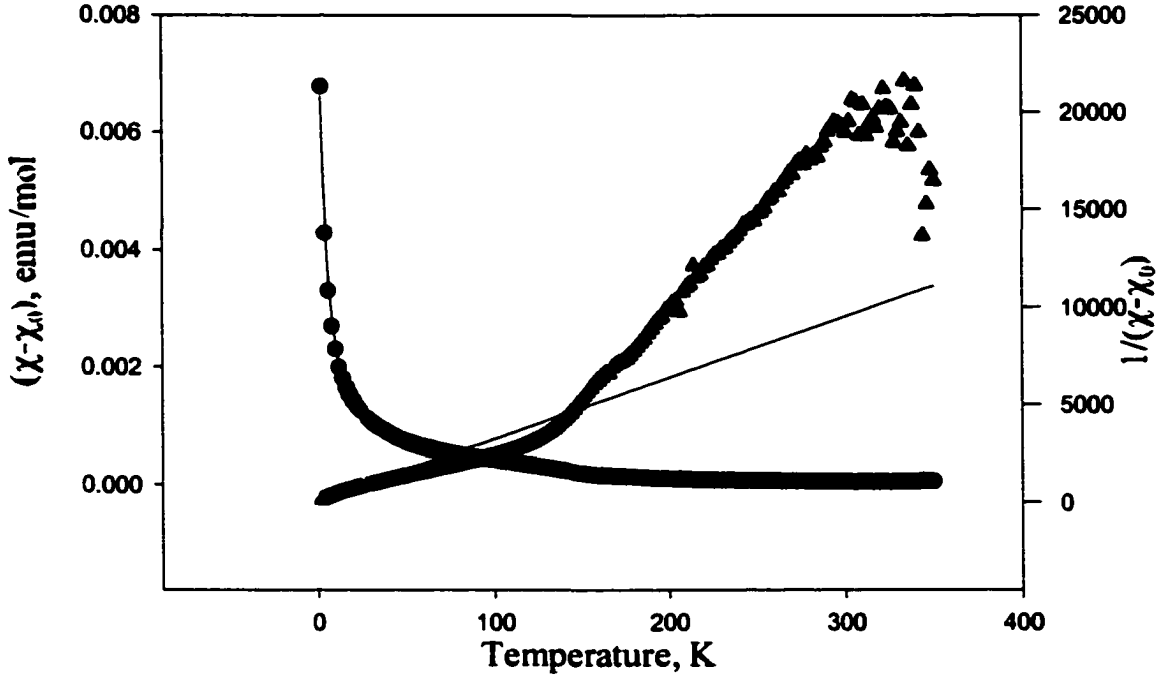

Figure 13. Magnetic susceptibility at 1 Tesla of a sample loaded as $CaLa_6I_{12}Os$ (16 e^-/cluster). Black circles and triangles represent χ and $1/\chi$, respectively, each corrected by a van Vleck term (χ_0), while the red lines show the Curie-Weiss fit to all data.

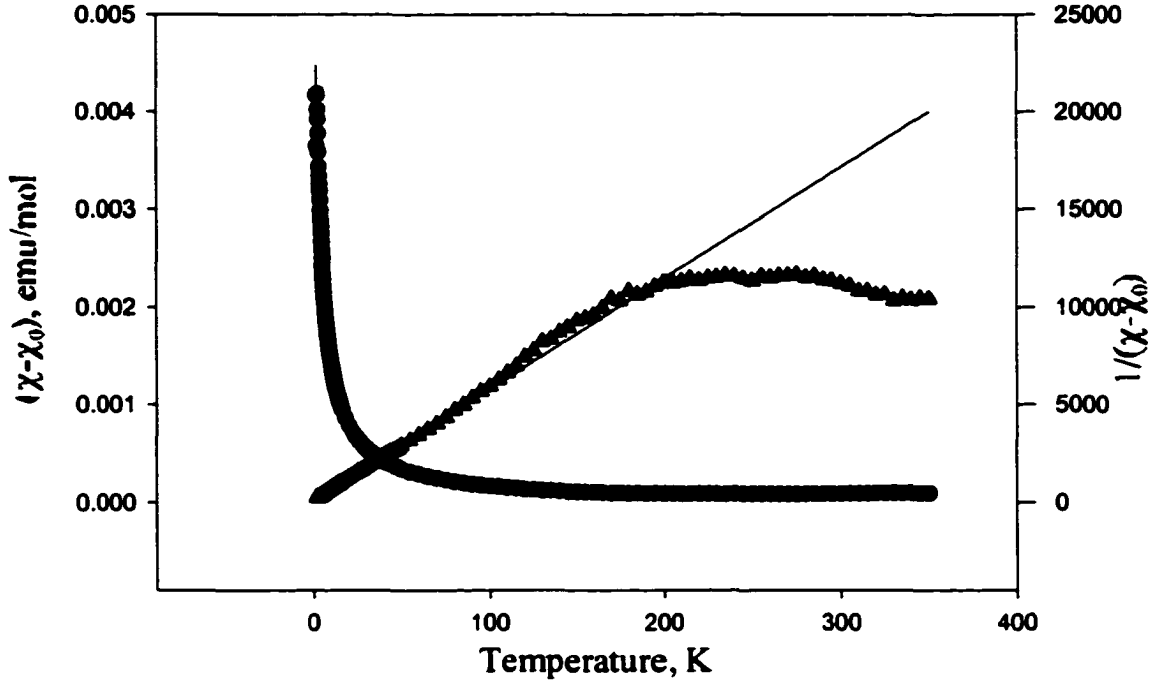

Figure 14. Magnetic susceptibility at 1 Tesla of a sample loaded as $SrLa_6I_{12}Os$ (16 e^-/cluster). Black circles and triangles represent χ and $1/\chi$, respectively, each corrected by a van Vleck term (χ_0), while the red lines show the Curie-Weiss fit to all data.

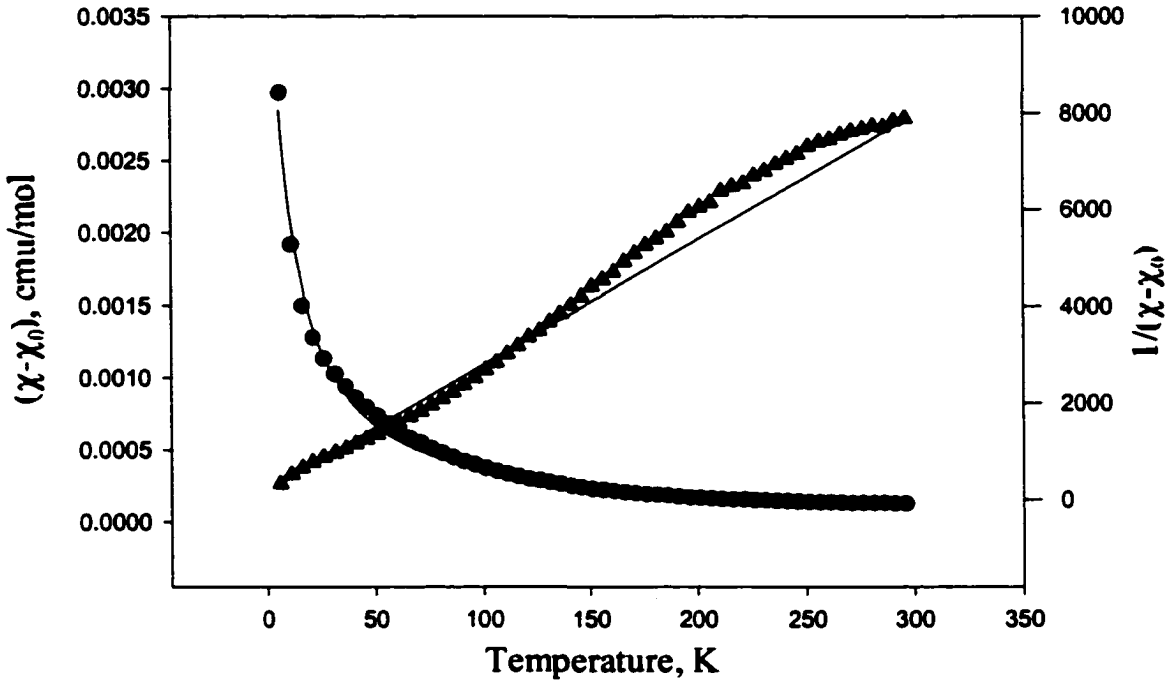

Figure 15. Magnetic susceptibility of $NaLa_6I_{12}Ir$ (16 e^-/cluster) at 3 Tesla. Black circles and triangles represent χ and $1/\chi$, respectively, each corrected by a van Vleck term (χ_0), while the red lines show the Curie-Weiss fit to all data.

or under the influence of an external magnetic field, one or more excited states could become populated by electrons, resulting in mixing of the Curie-Weiss paramagnetism with the magnetic character of the excited state(s) and causing the semblance of temperature independent paramagnetism (as in the $Li_2La_6I_{12}Os$ and $SrLa_6I_{12}Os$ examples) or drastically different $1/\chi$ vs. T slopes.

To explore this further, the susceptibility of a sample loaded $Li_2La_6I_{12}Os$ was measured at 1 Tesla and again at 5.5 Tesla. Both measurements showed similar Curie-Weiss behavior at low temperatures and nearly temperature-independent susceptibility at higher temperature, though neither displayed the abrupt transition that had been observed in the 3 Tesla data. The susceptibility (10^{-4} emu/mol) at 300 K was 9.54 at 1 Tesla and 6.34 at 5.5 Tesla. After fitting to the modified Curie-Weiss equation, plots of $1/\chi$ vs. T were made (Figure 16). Although the magnetic susceptibility was lower for the higher field measurement, the effective magnetic moment is not substantially changed by increased field: $\mu_{eff} = 0.32\mu_B$, $0.34\mu_B$ at 1, 5.5 Tesla, respectively. The behavior of the susceptibility above ~100 K was less clear for the 5.5 Tesla measurement and resulted in an array of widely scattered points, while the data for the 1 Tesla measurement continued to fall along a well-defined, although nonlinear, curve. The lower susceptibility and less linear plot of the 5.5 Tesla data could be interpreted as evidence that the higher magnetic field induces more mixing of two or more states than does the 1 Tesla field, but the similarity of the observed μ_{eff} values regardless of field strength is contradictory.

In addition, none of the effective magnetic moments calculated from the plots of $1/\chi$ vs. temperature were consistent with the spin-only theoretical values (~1.7 μ_B, ~2.9 μ_B for

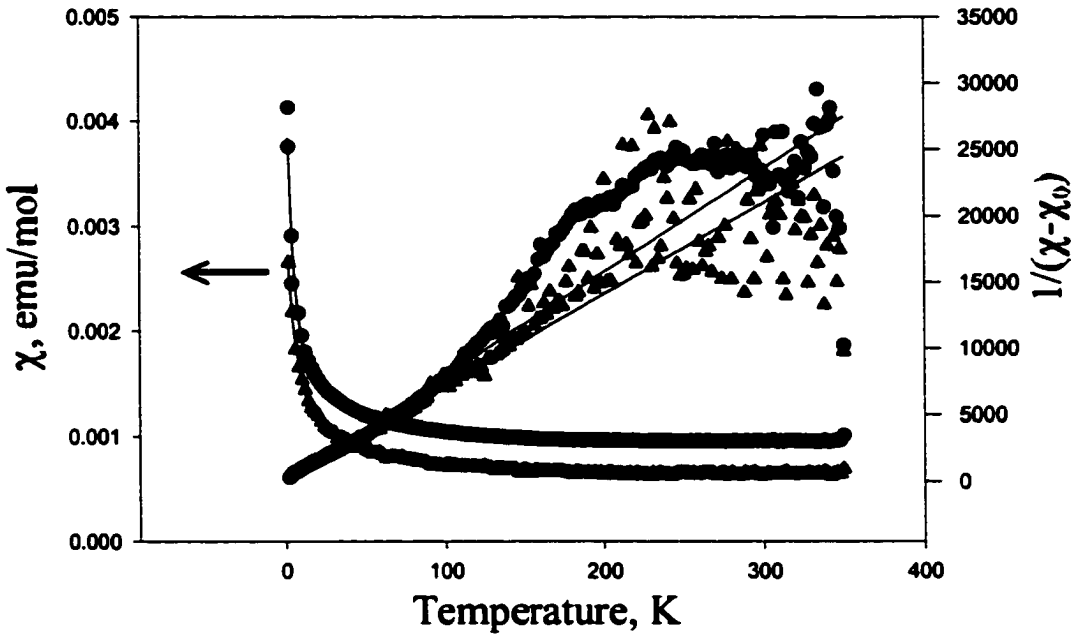

Figure 16. Magnetic susceptibility of a sample with loaded composition $Li_2La_6I_{12}Os$ at 1 Tesla (circles) and 5.5 Tesla (triangles). Fits of all data to the modified Curie-Weiss equation are shown in red and blue for 1 and 5.5 Tesla, respectively.

one and two unpaired electrons, respectively). All of the calculated μ_{eff} values were in the range 0.342–0.556 μ_B, which corresponds to about 1/5 to 1/3 unpaired electron per cluster in the spin-only model. These numbers suggest that the spin-only description is not appropriate for this system, although past work involving similar clusters with these elements has not resulted in such severe disagreement. Other Curie-Weiss paramagnetic compounds with isolated $(M,R)_6X_{12}$-type clusters gave μ_{eff} values much closer to the expected spin-only values, including $Zr_6I_{12}Mn$[5] (1.84(7) μ_B), $Sc_6I_{11}C_2$[12] (1.8(1) μ_B), $Sc_7I_{12}C$[10] (1.7 μ_B, isostructural with the $ALa_6I_{12}Z$ series), $CsZr_6I_{14}C$[3] (1.48 μ_B), $La_{12}I_{17}Fe_2$[50] (1.11(2) μ_B), and α-$K_4La_6I_{14}Os$[26] (0.77 μ_B). All of these examples were predicted to have a single unpaired electron per cluster, but $CsLa_6I_{10}Z$[21] (also made up of isolated R_6X_{12} clusters) has one unpaired electron for Z = Fe and two unpaired electrons for Z = Mn, which fits with the observed μ_{eff} values of 1.4 and 2.9 μ_B, respectively. None of the above was reported to have deviations in magnetic susceptibility comparable to those found for $ALa_6I_{12}Z$ compounds, except isostructural $Sc_7I_{12}C$, where a flattening at ~300 K was postulated to result from "thermal population of neighboring levels" and the metallic α-$K_4La_6I_{14}Os$ in which delocalized conduction electrons produced a spin-paired system with Pauli-like paramagnetism above ~270 K.

It is possible that the heavy elements in the present compounds, notably osmium and lanthanum, experience extensive spin-orbit coupling and contribute some of the deviations from ideal Curie-Weiss behavior. Octahedral Os^{IV} halide complexes are known to have lower than expected μ_{eff} values. This can be attributed to both the greater frequency of low spin configurations in these complexes and coupling between the S and L angular momentum vectors.[51] If similar spin-orbit coupling is occurring in these $R_6X_{12}(Z)$ clusters, due to either

the lanthanide or heavy transition metal atoms, that would generate the ridiculously low observed μ_{eff} values. Magnetic susceptibilities have not been reported for any unsubstituted $R_7X_{12}Z$ compounds; but it would be interesting to measure the magnetic susceptibilities of some $AR_6I_{12}Z$ compounds with lighter transition metal Z in order to compare their magnetic moments to the Z = Os, Ir compounds presented here.

Extended Hückel Molecular Orbital Calculations

The isolated $[La_6I_{18}Os]^{8-}$ cluster (including the six I^{a-i}) had S_6 symmetry but was not greatly distorted from ideal O_h symmetry. The La–La distances within the triangular "top" and "bottom" of each trigonal antiprism were generally about 0.01 Å shorter than the La–La distances between those triangular faces. In fact, among the new crystal structures discussed in this work, the ratios of the two R–R distances ranged only from 0.992 to 0.999. In previous studies on rhombohedral $R_7X_{12}Z$-type compounds, the clusters were treated as ideal octahedra.[7,13]

As in earlier work, the molecular orbital picture of the $[La_6I_{18}Os]^{8-}$ cluster using S_6 cluster symmetry resulted in a virtually nonbonding t_{1u} HOMO which was due to only weak R–R bonding. It can be seen in Figure 17 that the triply degenerate HOMO was split by the cluster distortion into doubly degenerate e_u and single a_u levels, but the separation was small, on the order of 0.022 eV. The character of the HOMO allows cluster electron counts to range from 15 to 18, although the 18 electron case has not been observed in the $ALa_6I_{12}Z$ series. The rest of the valence molecular orbitals followed the pattern of other $R_7X_{12}Z$ compounds with transition metal Z. The transition metal Z atom contributed an essentially nonbonding e_g set just below the HOMO and below that, strong R–Z π and σ overlaps

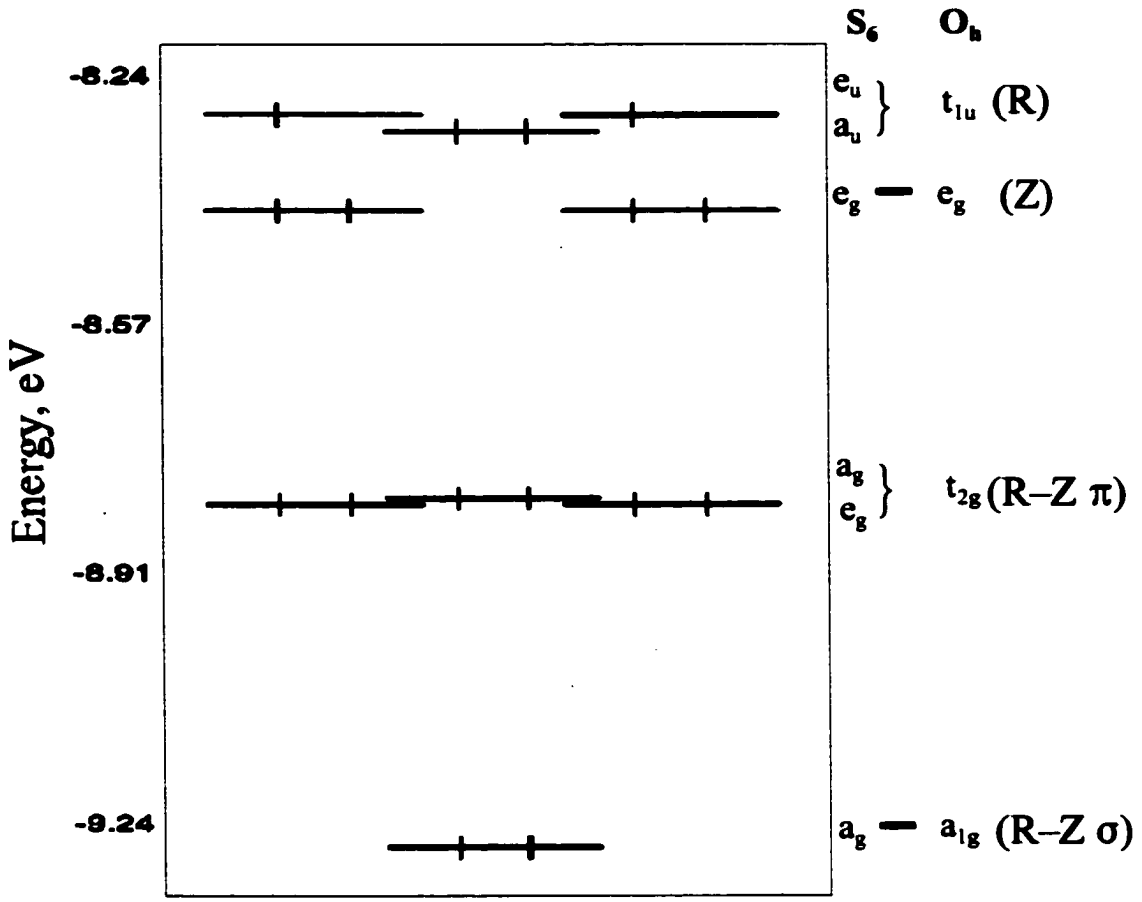

Figure 17. Molecular orbital diagram, including several valence orbital energy levels, from calculations on the isolated $[La_6I_{18}Os]^{8-}$ clusters in $SrLa_6I_{12}Os$. The O_h symmetry labels are also presented for reference. The $e_g + a_g$ LUMO (not shown) is ~ 0.9 eV above the e_u HOMO.

produced bonding $a_g + e_g$ (t_{2g} in O_h) and a_g levels. The LUMO, a t_{2g} split into e_g and a_g by symmetry, was separated from the HOMO by only about 0.9 eV.

It was hoped that molecular orbital calculations would help in interpreting the results of the magnetic susceptibility experiments. In order to better understand the effects of the cluster distortion on the energy levels, calculations on the same cluster were performed with the La positions changed to increase or decrease the distance between the "top" and "bottom" triangular faces (i. e. elongating or compressing the cluster along the three-fold crystallographic rotation axis parallel to *c*). The results in Table 50 show that elongating or compressing the cluster by about ±0.1 Å (keeping the other distances constant) decreased the HOMO-LUMO gap by about 0.6 eV. The most change for the frontier orbitals was seen in the separation between the e_u and a_u levels which increased from 0.022 eV in the original calculation using distances from single crystal x-ray diffraction experiments to 0.571 and 0.464 eV for calculations with elongated and compressed La–La distances, respectively. The a_u energy remained below the e_u energy in all cases. As the cluster was either stretched or compressed along the three-fold axis parallel to *c*, which distorted the cluster from O_h to S_6 symmetry, the molecular orbital energy levels were split further apart regardless of the sign of the change.

Even if the degeneracies of the energy levels were further broken by application of an external magnetic field, it is difficult to understand the susceptibility data. Several of the frontier orbitals will always be within 1 eV or less of each other, leading to many possible excited states.

Table 50. Frontier orbital energies of $[La_6I_{18}Os]^{8-}$ (eV)

	a_g	LUMO e_g	HOMO e_u	a_u
Crystallographic[a]	-7.2	-7.3	-8.3	-8.3
Long La–La[b]	-7.9	-7.9	-8.3	-8.8
Short La–La[c]	-7.9	-7.9	-8.3	-8.8

[a] La–La within triangular faces = 4.053 Å, La–La between triangular faces = 4.075 Å
[b] La–La within triangular faces = 4.053 Å, La–La between triangular faces = 3.950 Å
[c] La–La within triangular faces = 4.053 Å, La–La between triangular faces = 4.150 Å

Summary and Conclusion

A series of quaternary lanthanide halide cluster compounds $AR_6I_{12}Z$ (R = La, Pr) with transition metal interstitials (Z) and alkali or alkaline earth metal cations (A) has been synthesized by high temperature solid state techniques in the rhombohedral structure type known for $R_7X_{12}Z$. Results of examinations of powder x-ray diffraction patterns and refinement of lattice constants suggested that compounds with A = Li, Na, Mg, Ca, Sr could be prepared, while heavier alkali and alkaline earth metal A did not lead to the formation of analogous compounds. Single crystals in which A = Li, Na, Ca, Sr were structurally characterized by single crystal x-ray diffraction to show that the A element occupied the R2 position halfway between R_6Z trigonal antiprismatic clusters along *c*. This position was occupied by R and A atoms according to (A_xR_{1-x}), $x \leq 1$, with greater x as more A was loaded into the reaction composition. Energy dispersive spectroscopy on selected examples agreed with the x-ray diffraction results. The $LiLa_6I_{12}Os$ compound was further studied by neutron powder diffraction and ^7Li nuclear magnetic resonance in order to locate the lithium cations

more confidently. Calculation of the void spaces within the crystal lattice indicated that there were no other sites of adequate size available for the cation.

The electrical and magnetic properties of these compounds were also examined. The results of bulk resistivity measurements on various compositions showed that all of the compounds are semiconductors. The magnetic susceptibilities of these compositions fit well with the equation for Curie-Weiss paramagnetism (modified by a van Vleck term) at lower temperatures. At higher temperatures (above ~ 100–150 K), a more complicated magnetic character was evident, possibly due to spin-orbit coupling of the heavy transition metal Z and/or mixing of the ground magnetic state with one or more excited states.

CHAPTER 4. UNRESOLVED PROBLEMS AND FURTHER WORK

Solid state inorganic chemists, unlike organic chemists, often cannot direct the synthesis of desired compounds; this is both a curse and a blessing. On one hand, a researcher can expend great time and energy without achieving the proposed results, regardless of his or her diligence, intelligence or technique level. On the other hand, sometimes the planned synthetic experiment produces a totally new and unexpected creation instead of the intended outcome. Lanthanide halide compounds offer virtually infinite opportunities for discovery because of the number of competing variables involved in syntheses: stoichiometry, reaction temperature, reaction time, cooling rate and stability of alternate phases (related to packing efficiency and electronic effects). The addition of cations or substitution of known structures by different elements can result in more or less obvious structural modifications (e.g. expansion of a network to accommodate cations or condensation of clusters in response to changed electron concentrations) or in radical digressions.

In the $AR_6X_{12}Z$ family, although much has been revealed in this work, there still exist avenues for exploration. For example, almost nothing is known about the structures or properties of the corresponding bromides $ALa_6Br_{12}Z$. As suggested above, it would be interesting to test the magnetic susceptibilities of examples of $ALa_6I_{12}Z$ where Z is a first or second row transition metal, to ascertain whether the magnetic moments are better behaved (i. e. described by the classical, spin-only model). Single crystal x-ray diffraction on one of the problematic compositions (e. g. $CaLa_6I_{12}Os$ or $SrLa_6I_{12}Os$) at low temperature (~ 100 K)

could show whether the magnetic transition is associated with a structural modification. In the absence of a structural change, it would be helpful to fit the data to an equation that includes terms for spin-orbit coupling and for the non-Curie-Weiss states that were proposed to cause the strange behavior at higher temperatures. If these states contribute temperature-independent paramagnetic or even diamagnetic character to the compound, they will cancel out some of the Curie-Weiss character in the total susceptibility and produce the observed result. A more detailed multi-electron molecular orbital calculation may also be useful for examining the available excited states, with and without an external magnetic field.

There are also other systems that might be worthwhile to examine. Preliminary reactions loaded as $A_2La_{10}I_{19}Z_2$ (A = K, Rb; Z = Si, Ni, Rh, Os) and held for two days at 1000 °C, followed by one week at 800 °C, and cooled 10 °C/h resulted in similar, completely unidentifiable powder patterns; but no suitable single crystals were found. This was also the case with reactions loaded $NaSm_6Br_{12}Z$ (Z = B, Si, P), heated to 1075 °C for several hours and slowly cooled to room temperature over a period of two weeks. Other reactions loaded $A_5La_6I_{14}Os$ (A = Rb, Cs) and held at 900 °C for one week before cooling 10 °C/h produced several single crystals with symmetry and lattice constants similar to those of an unfinished refinement of tetragonal "$Rb_{4.37}La_6I_{14}Os$".[52] The original x-ray diffraction study suffered from problems associated with an uncertain space group assignment and fractional occupation of one of the cation sites. Subsequent single crystals appeared to be twinned or defective, and refinement of x-ray data was not satisfactorily completed.

REFERENCES CITED

(1) Simon, A.; Schnering, H. G.; Wöhrle, H.; Schäfer, H. *Z. Anorg. Allg. Chem.* **1965**, *339*, 155.

(2) Bauer, D.; von Schnering, H.-G. *Z. Anorg. Allg. Chem.* **1968**, *361*, 259.

(3) Smith, J. D.; Corbett, J. D. *J. Am. Chem. Soc.* **1985**, *107*, 5704.

(4) Hwu, S. J.; Corbett, J. D. *J. Solid State Chem.* **1986**, *64*, 331.

(5) Hughbanks, T.; Rosenthal, G.; Corbett, J. D. *J. Am. Chem. Soc.* **1988**, *110*, 1511.

(6) Smith, J. D.; Corbett, J. D. *J. Am. Chem. Soc.* **1984**, *106*, 4618.

(7) Hughbanks, T.; Corbett, J. D. *Inorg. Chem.* **1988**, *27*, 2022.

(8) Hughbanks, T.; Rosenthal, G.; Corbett, J. D. *J. Am. Chem. Soc.* **1986**, *108*, 8289.

(9) Ziebarth, R. P.; Corbett, J. D. *J. Solid State Chem.* **1989**, *80*, 56.

(10) Dudis, D. S.; Corbett, J. D.; Hwu, S. J. *Inorg. Chem.* **1986**, *25*, 3434.

(11) Warkentin, E.; Masse, R.; Simon, A. *Z. Anorg. Allg. Chem.* **1982**, *491*, 323.

(12) Dudis, D. S.; Corbett, J. D. *Inorg. Chem.* **1987**, *26*, 1933.

(13) Payne, M. W.; Corbett, J. D. *Inorg. Chem.* **1990**, *29*, 2246.

(14) Payne, M. W.; Dorhout, P. K.; Kim, S. J.; Hughbanks, T. R.; Corbett, J. D. *Inorg. Chem.* **1992**, *31*, 1389.

(15) Lulei, M.; Martin, J. D.; Hoistad, L. M.; Corbett, J. D. *J. Am. Chem. Soc.* **1997**, *119*, 513.

(16) Mattausch, H.; Warkentin, E.; Oeckler, O.; Simon, A. *Z. Anorg. Allg. Chem.* **2000**, *626*, 2117.

(17) Steinwand, S. J.; Corbett, J. D. *Inorg. Chem.* **1996**, *35*, 7056.

(18) Ebihara, M.; Martin, J. D.; Corbett, J. D. *Inorg. Chem.* 1994, 33, 2079.

(19) Berroth, K. Ph. D. Dissertation, University of Stuttgart, 1980.

(20) Corbett, J. D. *J. Alloys Compd.* **1995**, *229*, 10.

(21) Lulei, M.; Corbett, J. D. *Z. Anorg. Allg. Chem.* **1996**, *622*, 1677.

(22) Lulei, M.; Corbett, J. D. *Inorg. Chem.* **1996**, *35*, 4084.

(23) Lulei, M.; Maggard, P. A.; Corbett, J. D. *Angew. Chem. Int. Ed. Engl.* **1996**, *35*, 1704.

(24) Artelt, H. M.; Schleid, T.; Meyer, G. *Z. Anorg. Allg. Chem.*, **1992**, *618*, 18.

(25) Uma, S.; Corbett, J. D. *J. Solid State Chem.* **2001**, *161*, 161.

(26) Uma, S.; Martin, J. D.; Corbett, J. D. *Inorg. Chem.* **1999**, *38*, 3825.

(27) Corbett, J. D. *Inorg. Synth.* **1983**, *22*, 31.

(28) Meyer, G.; Dötsch, S.; Staffel, T. *J. Less-Common Met.* **1987**, *127*, 155.

(29) Corbett, J. D. In *Solid State Chemistry: Techniques*; Cheetham, A. K., Day, P. Eds.; Oxford University: Oxford, 1987; Chapter 1.

(30) Clark, C. M.; Smith, D. K.; Johnson, G. J. "A Fortran IV Program for Calculation of X-Ray Powder Diffraction Patterns-Version 6," Department of Geosciences, Pennsylvania State University: University Park, PA, 1973.

(31) Werner, P.-E. Arrhenius Laboratory, University of Stockholm, Stockholm, Sweden, 1990.

(32) Maggard, P. A., Ames Laboratory, Iowa State University, Ames, IA, unpublished results, 1995.

(33) Takusagawa, F., Ames Laboratory, Iowa State University, Ames, IA, unpublished results, 1981.

(34) *International Tables for X-Ray Crystallography*, 2nd ed.; Lonsdale, K., Macgillavry, C. H., Rieck, G. D., Eds.; Kynock Press: Birmingham, England, 1968, Vol. III.

(35) *International Tables for Crystallography*, 2nd rev. ed.; Hahn, T., Ed.; Kluwer Academic Publishers: Dordrecht, Germany, 1989, Volume A.

(36) Rietveld, H. M. *J. Appl. Cryst.* **1969**, *2*, 65.

(37) Young, R. A. *The Rietveld Method*; Oxford University: New York, 1993.

(38) Larson, A. C.; Von Dreele, R. B. *GSAS: General Structure Analysis System*, Los Alamos National Laboratory, Los Alamos, NM, 1986-1994.

(39) Lovesey, S. W. *Theory of Neutron Scattering From Condensed Matter*, Clarendon: Oxford, 1984, Vol. 1.

(40) Guloy, A. M.; Corbett, J. D. *Inorg. Chem.* **1996**, *35*, 4669.

(41) El-Hanany, U. *Rev. Sci. Instrum.* **1973**, *44*, 1067.

(42) Shinar, J.; Dehner, B.; Beaudry, B. J.; Peterson, D. T. *Physical Review B*, **1988**, *37*, 2066.

(43) Ren, J.; Liang, W.; Whangbo, M.-H. *CAESAR*; PrimeColor Software: Raleigh, NC, 1998.

(44) Alvarez, S. Tables of Parameters for Extended Hückel Calculations, Parts 1 and 2, Barcelona, Spain, 1987.

(45) Park, Y.; Martin, J. D.; Corbett, J. D. *J. Solid State Chem.* **1997**, *129*, 277.

(46) Dorhout, P. K.; Payne, M. W.; Corbett, J. D. *Inorg. Chem.* **1991**, *30*, 4960.

(47) Hughbanks, T.; Corbett, J. D. *Inorg. Chem.* **1989**, *28*, 631.

(48) Shannon, R. D. *Acta Crystallogr.* **1976**, *32A*, 751.

(49) Zhang, J.; Corbett, J. D. *Inorg. Chem.* **1991**, *30*, 431.

(50) Lulei, M.; Martin, J. D.; Corbett, J. D. *J. Solid State Chem.* **1996**, *125*, 249.

(51) Greenwood, N. N.; Earnshaw, A. *Chemistry of the Elements*, 2nd ed.; Butterworth-Heinemann: Oxford, 1984; p 1087.

(52) Uma, S., Ames Laboratory, Iowa State University, Ames, IA, unpublished results, 1999.

ACKNOWLEDGMENTS

My years as a student at Iowa State University have been challenging, fulfilling, and exciting but I would not have achieved my goal without the help of many people. To the person most responsible for the guidance and support of my research, Professor John D. Corbett, I extend special thanks. I remember with gratitude the many past and present members of the Corbett and Franzen groups, especially Michael Klem, for camaraderie and discussions of wide-ranging topics. Shirley Standley, K. G. Baikerikar, and James Anderegg have each influenced my success by offering friendly conversation and advice as well as performing their ordinary duties, without which the lab could not operate.

Also, I gratefully acknowledge Jerome Ostenson and Serguei Bud'ko for the measurements of magnetic properties and for discussions thereon, Warren Straszheim for the EDS measurements, Shu Xu for the NMR measurements, Chris Murphy at Argonne National Laboratory for measurement of the neutron powder diffraction data, and former Corbett group member Robert Henning for patient tutoring and help with the refinement of the neutron data. No less importantly, I acknowledge Professors Gordon J. Miller, H. F. Franzen, and David Johnston for engaging discussions on many subjects, including chemistry.

I am extremely grateful to my parents, Ralph and Susan Jensen, for encouraging my interest in science and supporting me with love. Finally, countless thanks to Bruce Miller for believing in me and sharing my life.

This research was supported by the National Science Foundation – Solid State Chemistry – Grants DMR - 9510278, - 9809850, - 0129785, and was carried out in the facilities of the Ames Laboratory, U. S. Department of Energy.